

Accuracy Improvements for Computational Methods and Color Rendering Index Calculations in Global Illumination Models

Dissertation

by

David Geisler-Moroder

submitted to the Faculty of Mathematics, Computer
Science, and Physics of the University of Innsbruck

in partial fulfillment of the requirements
for the degree of doctor of science

advisor: ao. Univ.-Prof. Mag. Dr. Arne Dür
Department of Mathematics, University of Innsbruck

Innsbruck, March 2010

Acknowledgments

I would like to thank

my supervisor Ao. Univ.-Prof. Mag. Dr. Arne Dür for both his excellent scientific mentoring and his patience throughout the development of the present thesis,

Mag. Christian Knoflach and Dipl.-Ing. Rico Thetmeyer at Bartenbach LichtLabor for valuable discussions and support with measurement data and test scenes,

the University of Innsbruck for financial support through a “Doktoratsstipendium” and a “Förderungsstipendium”,

the FFG for the financial support through the FIT-IT Visual Computing dissertation fellowship project “CRIGIM” under Grant No. 816009,

and my colleagues in the office and the Department of Mathematics for providing a delightful working atmosphere.

My very personal thanks belong

to my parents Maria and Klaus for their absolute and never-ending support,

and – unconditionally – to Raphaela.

Overview

The present thesis is basically arranged in four chapters that are preceded by a short introduction. All research work was done in collaboration with my supervisor Arne Dür.

In Chapter 1 the physically based renderer RADIANCE is validated against selected test scenes from the CIE 171:2006 publication *Test Cases to Assess the Accuracy of Lighting Computer Programs* [CIE06]. We use the six experimental test cases and three scenes with analytical references and show that RADIANCE yields highly accurate results if appropriate parameter settings are selected. The only weakness that was discovered occurred in test scenes containing circular luminaires where the simulated mean room illuminance was below the CIE lower limit. The results of this validation were presented at the *7th International RADIANCE Workshop* [GMD08].

Chapter 2 analyzes computational methods that are implemented in RADIANCE and proposes modifications that improve the accuracy of the calculations. Based on the findings from Chapter 1 the adaptive source subdivision algorithm implemented in RADIANCE is investigated in the first section. Here we present an improved subdivision algorithm for circular light sources that avoids ray aiming failures and thus increases the accuracy in the direct illumination calculation. Together with the validation of RADIANCE this method was presented at the *7th International RADIANCE Workshop* [GMD08]. In the second part we analyze the Ward-Dür BRDF and its sampling, and survey the problematic behaviour at grazing angles. Incorporating the criticism by Neumann et al. [NNSK99] we propose a modification that preserves Helmholtz reciprocity, is computationally cheap to evaluate, admits efficient importance sampling, and proved to be better suited for fitting measured BRDF data of a linoleum floor used in a real-world building. We plan to present this work at a computer graphics conference on rendering.

Chapter 3 discusses color rendering with local or global illumination. We propose an improved color rendering index (CRI) that brings the standard CIE CRI up to date and is better qualified to predict human color perception especially for LED light sources. In the second part we describe how RADIANCE is extended from RGB to a discrete spectrum using 81 wavelengths and how this spectral renderer can be used to predict the CRI and the correlated color temperature in globally illuminated scenes. These results were presented at the conference *Human Vision and Electronic Imaging XIV* [GMD09a] and have been published in the article *Color-rendering indices in global illumination methods* in the *Journal of Electronic Imaging* [GMD09b].

In Chapter 4 we use the spectral extension of RADIANCE for evaluations by two action spectra other than the luminous efficiency function – the circadian action function describing the melatonin suppression and the photosynthesis action spectrum. We display how the corresponding indices can be estimated in real-world scenes and show that inaccuracies introduced by RGB approximations are significant. This work will be presented at the *5th European Conference on Colour, Imaging, and Vision CGIV 2010* and appear in the article *Estimating Melatonin Suppression and Photosynthesis Activity in Real-World Scenes from Computer Generated Images* in the conference proceedings [GMD10].

Overview

Contents

Acknowledgments	iii
Overview	v
Introduction	1
1 Validation of RADIANCE Against CIE 171:2006 Test Cases	3
1.1 Proposed Experimental Test Cases	4
1.1.1 TC 4.1 – CFL, gray wall	5
1.1.2 TC 4.2 – Opal luminaire, gray wall	6
1.1.3 TC 4.3 – Semi-specular reflector (SSR) luminaire, gray wall	7
1.1.4 TC 4.4 – CFL, black wall	7
1.1.5 TC 4.5 – Opal luminaire, black wall	8
1.1.6 TC 4.6 – Semi-specular reflector luminaire, black wall	8
1.2 Proposed Test Cases with Analytical References	9
1.2.1 TC 5.6 – Light reflection over diffuse surfaces	9
1.2.2 TC 5.7 – Diffuse reflection with internal obstructions	14
1.2.3 TC 5.8 – Internal reflected component calculation for diffuse surfaces	16
1.3 Conclusion	17
2 Improvements in the Accuracy of Computational Methods in RADIANCE	19
2.1 Sampling of Circular Area Light Sources	19
2.1.1 Adaptive Source Subdivision in RADIANCE	19
2.1.2 Improved Adaptive Subdivision of Circular Light Sources	21
2.1.3 Alternative Solution in RADIANCE 3.9	26
2.1.4 Conclusion	28
2.2 A New BRDF Model Based on the Ward-Dür BRDF	29
2.2.1 The Ward-Dür BRDF and its Sampling	29
2.2.2 New BRDF	34
2.2.3 Fitting the New BRDF	38
2.2.4 Conclusion	41
3 Color Rendering Indices in Global Illumination Methods	43
3.1 Background	43
3.2 Related Work	44
3.3 CRI	46
3.3.1 Standard CIE Method for Calculating CRIs	46

Contents

3.3.2	The Recent Proposal of the CIE – $R96_a$	47
3.3.3	Alternative Method for Calculating CRIs	47
3.4	Global Illumination Methods	52
3.4.1	Cornell Box	54
3.4.2	Ward – Eydelberg-Vileshin Test Scene	56
3.4.3	CRI Test Scene	57
3.4.4	Real-World Seminar Room	59
3.5	Discussions and Future Work	61
3.6	Conclusion	62
4	Estimating Melatonin Suppression and Photosynthesis Activity	63
4.1	Background	63
4.2	Spectral Rendering	65
4.2.1	Test scene	65
4.2.2	Weighting functions	66
4.2.3	Circadian action function	67
4.2.4	Photosynthesis activity	69
4.3	RGB Approximation	69
4.4	Conclusion	74
A	CIE 171:2006 Test Cases 4.1 - 4.6: Results	75
B	Supplementary Material for the New BRDF Model	83
	Bibliography	87
	Curriculum Vitae	95

Introduction

Global illumination methods are commonly used tools in computer graphics to obtain photorealistic images. Moreover it is important to have realistic and physically correct simulations for many applications. For example prototyping as well as architectural design, industrial design and lighting engineering are fields where photorealistic rendering and radiometrically correct computations are needed.

Lighting simulation starts with a so called local illumination model taking into account only surface characteristics and direct lighting. In contrast it is not only direct but also indirect illumination that occurs in real-world scenes. Global illumination methods, however, consider all objects in the scene as potential sources of lighting in order to simulate the effects of interreflection. The aim of a global illumination algorithm is to solve the *rendering equation* that describes the steady-state distribution of light energy in a scene and was first formulated by Kajiya [Kaj86] as

$$L(x, y) = L_e(x, y) + \int_{\Omega_x} L_i(x, z) f_r(x, y, z) \cos \theta_z d\omega_z,$$

where

$x \in \mathbb{R}^3$ is a point on a surface in the scene,

$y, z \in \mathbb{R}^3$ are directions,

$L(x, y)$ is the total outgoing radiance from point x into direction y ,

$L_e(x, y)$ is the emitted radiance from point x into direction y ,

$L_i(x, z)$ is the incident radiance at point x from direction z ,

$f_r(x, y, z)$ is the bidirectional reflectance distribution function specifying the amount of radiance incident at point x from direction z that is reflected into direction y ,

θ_z is the angle between z and the surface normal in x ,

$\omega_z = \sin \theta_z d\theta_z d\phi_z$ is the differential solid angle at direction z , and

Ω_x is the hemisphere around the surface normal in x .

The rendering equation is a Fredholm integral equation of the second kind and can thus be solved by a Neumann series. Background information on the Neumann series can be found in most books on functional analysis (e.g. [Heu92, Wer95]).

In computer graphics basically two approaches are used to approximate the Neumann series solution of the rendering equation. The *radiosity method* [SP94] is based on the assumption that all surfaces in the scene are perfectly diffuse. This method calculates the distribution of light energy by evaluating the form factors between the single surfaces. To enable simulations of scenes containing not only diffuse surfaces or with participating media, extensions to the radiosity method such as a bidirectional solution are needed.

Introduction

On the other hand, *ray tracing methods* [Gla89, DBB03] send virtual light rays from the light sources into the scene, where they are reflected and eventually hit the image plane (forward ray tracing, see Figure 0.1(a)). Because this procedure is only effective if most rays really hit the receiver and do not leave the scene somewhere else, forward ray tracing is mainly used for simulations of optical systems and lenses. However, in simulations of real-world scenes such as the interior lighting of buildings, most rays would miss the image plane resulting in a computationally demanding procedure. For these cases pixel-driven or backward ray tracing is better qualified, because here the sample rays are sent from the view point through the pixel in the image plane into the scene (see Figure 0.1(b)).

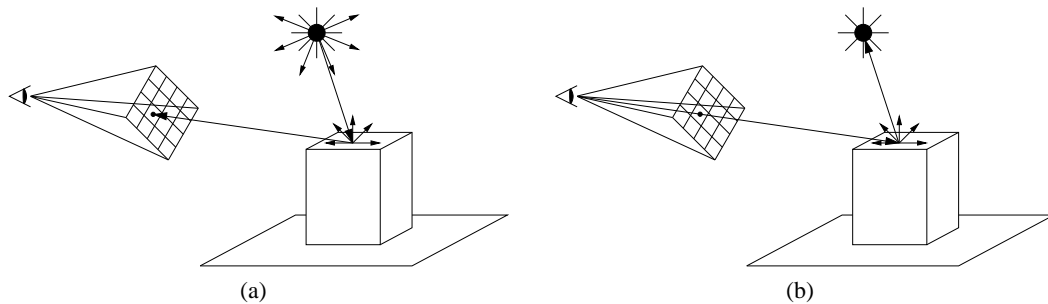


Figure 0.1: Basic idea of (a) forward ray tracing and (b) backward ray tracing.

In the physically-based rendering software RADIANCE [WS98] that has been developed by Greg Ward since 1985, backward ray tracing is implemented. RADIANCE is widely used in lighting design and architectural illumination planning for simulations of luminance and illuminance distributions. Especially for daylight simulations and daylight factor calculations this rendering tool is frequently used and was validated in [Gry89, Mar99, UWP05, RB06, GMD08].

The aim of the present thesis is to investigate the mathematical methods and algorithms that are implemented in RADIANCE and to propose modifications and extensions that make this powerful software toolkit more accurate and even more powerful. We propose an improved algorithm for the adaptive subdivision of circular light sources that is used as sampling scheme for the Monte Carlo integration of flat area light sources. Based on investigations on the energy balance of the Ward-Dür BRDF [Dür06] a modified BRDF is presented that meets energy balance and is suitable for importance sampling. Finally, we propose to extend RADIANCE from RGB to a discrete spectrum for reasons of accuracy and applicability of spectrally selective calculations. We exemplify this by calculating the color-rendering index, the correlated color temperature, the circadian action factor, and the photosynthesis activity from computer generated images of real-world scenes rendered with RADIANCE.

1 Validation of RADIANCE Against CIE 171:2006 Test Cases

Drum prüfe, wer sich ewig
bindet . . .

(Friedrich von Schiller,
1759-1805)

In 2006 the technical committee 3-33 of the International Commission in Illumination (CIE) proposed “test cases to assess the accuracy of lighting computer programs” in their publication CIE 171:2006 [CIE06]. The goal of the committee was to find test cases that help users to compare different simulation programs in terms of various aspects of light propagation.

The set of proposed scenes consists of both experimental test cases and test cases with analytical references. The former are based on the experimental protocol of CIBSE TM 28/00 by Slater and Graves [SG02] and describe real-world test scenes. For these test cases the reference data presented in [CIE06] were measured following given recommendations to minimize the possible ambiguities. For the second part of the test cases the analytical references were calculated based on the underlying physical laws. Thereby single aspects of the light propagation can be isolated and uncertainties in the reference values eliminated. The acceptance of these CIE test cases can be seen by published validations of well-known lighting software such as AGI32 [Dau07] and the Velux Daylight Visualizer 2 [LJJ09].

To assess the accuracy of simulations with RADIANCE we use all six proposed experimental test cases and select three test cases with analytical references that deal with various aspects of diffuse reflections. We consider them important because for example in architectural lighting design most surfaces are modeled with diffuse materials.

Unless otherwise noted RADIANCE in its version 3.8 is used for the simulations described in this chapter. A bug was corrected in *source.c* where we changed a function call from *intens()* to *bright()* (for details on the difference between these two functions see Chapter 3). Following our recommendation this was also changed in the later versions of RADIANCE (see CVS on [Rad10]).

We perform the illuminance calculations for the test scenes using RADIANCE’s *rtrace* program that is designed to compute (ir)radiance at single points. With the *rtrace* call

```
echo  $p_x p_y p_z d_x d_y d_z$  | rtrace -I [optional parameters settings] octree |  
rcalc -e '$I=47.4*$I+120*$2+11.6*$3'
```

the illuminance (option *-I*) at a measurement point (p_x, p_y, p_z) with measurement surface normal direction (d_x, d_y, d_z) is calculated in the scene that is specified by the *octree*. The call to *rcalc* at the end is used to transform from the radiometric unit irradiance to the photometric unit illuminance. In the different test scenes we specify additional parameters to account for varying

requirements due to geometry or materials and explain them where they occur. Further information on the modeling of geometry and materials as well as parameter settings can be found in [WS98].

All given rendering times were measured using a 3GHz Intel Core2 Duo E8400 with 4GB RAM.

1.1 Proposed Experimental Test Cases

In Chapter 4 of [CIE06] the CIE proposes test cases with reference values that were obtained from experimental measurements. Figure 1.1 shows the set-up of the test room that is 6.78m long, 6.72m wide, and has a ceiling height of 3.24m. Inside the room four regularly spaced luminaires are mounted at a height of 3.14m in case of point light sources (test cases 4.1 and 4.4) or at 3.20m in case of area light sources (test cases 4.2, 4.3, 4.5, and 4.6). Illuminance measurements are performed at 49 regularly spaced points as indicated in Fig. 1.1 at a height of 0.8m above the floor.

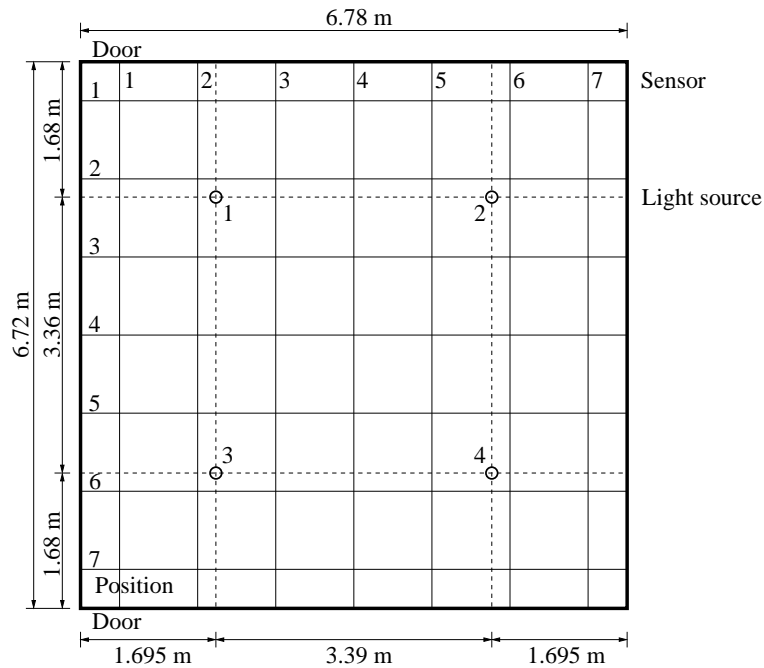


Figure 1.1: Set-up of CIE experimental test cases 4.1 to 4.6, with four light sources and 49 regularly spaced sensor positions.

The surface materials of the ceiling and the walls are spectrally neutral and “due to the low reflectance of the floor, the related error source is likely negligible with respect to the illuminance measurements” [CIE06]. Thus we also model the floor as being spectrally neutral. In our RADIANCE simulations we model the different surfaces perfectly diffuse, i.e. we set specularity and roughness both equal to zero because no BRDF measurements are available. For

1.1 Proposed Experimental Test Cases

the light sources measured luminous intensity distributions are given in CIBSE TM14 format in the appendix of [CIE06]. In RADIANCE such tabulated intensity distributions are attached to a *light* material by using a *brightdata* pattern. Because the CIE does not provide a spectrum for the luminaires, which are all fluorescent lamps, we use the spectrum of the standard fluorescent lamp FL11 as specified by the CIE in [CIE04]

For the RADIANCE simulations with *rtrace* the following parameters are changed from their default values:

-dt 0 -ab 6 -ad 3072.

Setting the direct threshold *-dt* to zero ensures that any direct contribution is accounted for, even for multiple reflected rays or small parts of a subdivided light source. The number of ambient bounces is set to *-ab 6* to allow sufficient diffuse reflections that contribute to the measured point illuminance. We also tested higher settings for *-ab*, but while the rendering times increased significantly, the simulated illuminance values did not change. The specified number of ambient divisions *-ad* determines how many child rays are spawned from a diffusely reflected ray. To increase the accuracy of the ambient calculation we tripled the default value from 1024 to 3072. Any additional parameter changes for single test scenes are given in the particular subsection.

The upper and lower mean room illuminance limits in Tables 1.1 to 1.6 as well as the total error band limits and the measurement band limits for the point illuminances that are presented in Appendix A in Tables A.1 to A.6 are taken from [CIE06]. The mean room illuminance limits are calculated as $m \pm 2 \cdot 0.063 \cdot m$, where m denotes the measured value. For the point illuminances the measurement band limits are defined as $m \pm 2 \cdot 0.067 \cdot m$, the total error band limits, which include both measurement and simulation errors, as $m \pm 2 \cdot 0.105 \cdot m$.

1.1.1 Test case 4.1 – Artificial lighting scenario - compact fluorescent lamp, gray wall

For test case 4.1 the surface reflectances are specified in [CIE06] with $R = 0.7 \pm 0.01$ for the white acoustic tiled ceiling, $R = 0.06 \pm 0.01$ for the dark brown floor, and $R = 0.41 \pm 0.02$ for the matte gray walls. In the RADIANCE simulations we model these surfaces as *plastic* with constant RGB values (R, R, R) where we do not consider the variations. For the four bare compact fluorescent lamps (CFLs) with measured total lumen outputs of 2182lm, 2196lm, 2203lm, and 2182lm no size is specified in [CIE06]. We chose to model them in RADIANCE as spheres with radii of 5cm using the *light* material with RGB values of $(143.4, 119.7, 71.4)$, $(144.3, 120.5, 71.8)$, $(144.7, 120.9, 72.1)$, and $(143.4, 119.7, 71.4)$, respectively, representing the FL11 spectrum with the particular lumen output.

The RADIANCE simulation result for the mean room illuminance in Table 1.1 is inside the limits given by the CIE. Considering the point illuminances, which can be found in Table A.1 in Appendix A, only 3 out of 49 values (6.1%) are slightly outside the measurement band, but all are inside the specified total error band. The calculation time for all 49 point illuminances was 144 seconds.

1 Validation of RADIANCE Against CIE 171:2006 Test Cases

Upper limit	112.0
Simulated mean room illuminance with RADIANCE	88.3
Lower limit	88.0

Table 1.1: RADIANCE result for the mean room illuminance of CIE test case 4.1, gray wall - CFL lamp, with upper and lower limits as given by the CIE.

1.1.2 Test case 4.2 – Artificial lighting scenario - opal luminaire, gray wall

In this test case the same surface materials as in test case 4.1 are used except for the reflectance of the wall which is $R = 0.52 \pm 0.02$ here. The four opal luminaires with measured total lumen outputs of 1850lm, 1830lm, 1870lm, and 2110lm are disks with a diameter of 0.45m. Thus we model them in RADIANCE as *ring* with inner radius of zero and outer radius of 0.225m and use the *light* material with RGB values of (10.51, 8.78, 5.23), (10.40, 8.68, 5.18), (10.62, 8.87, 5.29), and (11.99, 10.01, 5.97), respectively, representing the FL11 spectrum with the particular lumen output.

As this test scene contains large area light sources we modify an additional parameter in the *rtrace* call and set *-ds 0.02*. Thereby the number of subdivisions of a light source and thus the number of rays used for sampling increases. However, setting *-ds* to even smaller values leads to aiming failures in this test scene with circular luminaires. In Section 2.1 we investigate the sampling algorithm that is used in RADIANCE 3.8 and propose an improved subdivision algorithm for circular light sources.

Upper limit	67.5
Simulated mean room illuminance with RADIANCE	51.5
Simulated mean room illuminance with improved disk subdivision	54.1
Lower limit	53.1

Table 1.2: RADIANCE result for the mean room illuminance of CIE test case 4.2, gray wall - opal lamp, with upper and lower limits as given by the CIE.

The mean room illuminance calculated with RADIANCE is 4.8% below the lower limit given by the CIE. From the point illuminances, which can be found in Table A.2 in Appendix A, 32 out of 49 values (65.3%) are outside the measurement band, but all values are inside the specified total error band. However, using the improved subdivision algorithm (see Section 2.1) the simulated mean room illuminance is inside the error band and the ratio of point illuminances outside the measurement band is reduced to 24.5% (12 out of 49 values). With our proposed subdivision algorithm the rendering time increased from 188 to 258 seconds.

1.1.3 Test case 4.3 – Artificial lighting scenario - semi-specular reflector luminaire, gray wall

For this test scene the same materials as in test case 4.2 are used. The four square area light sources are semi-specular reflector (SSR) luminaires that have a side length of 60cm and measured total lumen outputs of 4087.7lm, 4174.7lm, 4135.0lm, and 4114.3lm. Again using the FL11 spectrum we derive RGB values of (19.16, 16.00, 9.53), (19.57, 16.35, 9.74), (19.33, 16.14, 9.62), and (19.30, 16.12, 9.61) for the four light sources. For the same reason as described in test case 4.2 the parameter $-ds$ is set to 0.02.

Upper limit	254.2
Simulated mean room illuminance with RADIANCE	234.7
Lower limit	199.8

Table 1.3: RADIANCE result for the mean room illuminance of CIE test case 4.3, gray wall - SSR luminaire, with upper and lower limits as given by the CIE.

The RADIANCE simulation results for the mean room illuminance as well as all 49 point illuminances (see Table A.3 in Appendix A) are within the error bands as specified by the CIE. The simulation time for this test scene 4.3 was 345 seconds for all 49 measurement points.

1.1.4 Test case 4.4 – Artificial lighting scenario - compact fluorescent lamp, black wall

For this test case 4.4 the surface reflectances are specified in [CIE06] with $R = 0.03 \pm 0.01$ for the black velvet ceiling, $R = 0.06 \pm 0.01$ for the dark brown floor, and $R = 0.04 \pm 0.01$ for the matte black walls. In the RADIANCE simulations we model these surfaces as *plastic* with constant RGB values (R, R, R) where we do not consider the variations. The same four luminaires as specified for test case 4.1 are used here.

Upper limit	37.5
Simulated mean room illuminance with RADIANCE	36.0
Lower limit	29.5

Table 1.4: RADIANCE result for the mean room illuminance of CIE test case 4.4, black wall - CFL lamp, with upper and lower limits as given by the CIE.

The RADIANCE simulation results for the mean room illuminance as well as all 49 point illuminances (see Table A.4 in Appendix A) are within the error bands as specified by the CIE. The simulation time for this test case 4.4 was 143 seconds for all 49 measurement points.

1.1.5 Test case 4.5 – Artificial lighting scenario - opal luminaire, black wall

The materials used in this test scene are equal to those specified for test case 4.4 and the circular opal luminaires’ specifications are the same as in test case 4.2. Again we additionally set the parameter *-ds* to 0.02 to increase the number of subdivisions of the large area light sources.

Upper limit	51.1
Simulated mean room illuminance with RADIANCE	40.5
Simulated mean room illuminance with improved disk subdivision	43.1
Lower limit	40.1

Table 1.5: RADIANCE result for the mean room illuminance of CIE test case 4.5, black wall - opal lamp, with upper and lower limits as given by the CIE.

The calculated mean room illuminances are inside the specified error limits for both the RADIANCE simulation and the simulation using the improved disk subdivision algorithm (see Section 2.1). However, with RADIANCE 14 out of 49 point illuminances (28.6%) are below the measurement band lower limit, whereas with the improved subdivision for circular light sources all values are within the given error band (see Table A.5 in Appendix A). The rendering times were 189 seconds with RADIANCE and 255 seconds using our proposed subdivision algorithm.

1.1.6 Test case 4.6 – Artificial lighting scenario - semi-specular reflector luminaire, black wall

The materials used in this test scene are equal to those specified for test case 4.4 and the semi-specular reflector luminaires’ specifications are the same as in test case 4.3. Again, we additionally set the parameter *-ds* to 0.02 to increase the number of subdivisions of the four large area light sources.

Upper limit	228.5
Simulated mean room illuminance with RADIANCE	212.9
Lower limit	179.5

Table 1.6: RADIANCE result for the mean room illuminance of CIE test case 4.6, black wall - SSR luminaire, with upper and lower limits as given by the CIE.

The RADIANCE simulation results for the mean room illuminance as well as all 49 point illuminances (see Table A.6 in Appendix A) are within the error bands specified by the CIE. The simulation time for all 49 measurement points was 308 seconds.

1.2 Proposed Test Cases with Analytical References

In Chapter 5 of [CIE06] the CIE proposes test cases with analytical references. These analytical reference values are calculated from theoretical, physical laws, which are usually the basis of lighting simulation software such as RADIANCE. The aim of these test scenes is to isolate certain aspects of the light propagation and to minimize or even eliminate uncertainties in the reference values. The CIE reference values that are used in Tables 1.7 to 1.11 are taken from [CIE06].

1.2.1 Test case 5.6 – Light reflection over diffuse surfaces

In architectural lighting design the simulation of diffuse reflection is an essential part. Inter-reflections inside a room or the reflection of daylight on the exterior ground are examples for reflections on surfaces that are usually modeled to be lambertian and that yield an important contribution to global illumination.

The basic set-up of the three scenarios contains a perfectly diffuse and spectrally neutral ground plane S_2 that receives uniform direct illuminance from a distant light source (e.g. the sun). Two measurement planes – one horizontal S_{1-hz} and one vertical S_{1-v} – are modeled as perfect absorbers with a reflectance of 0% that are not illuminated directly by the light source but only receive indirect illumination from the diffuse reflection on S_2 .

The distant light source is modeled in RADIANCE using the *source* “material” that actually specifies a solid angle. We specify its direction according to the particular given angle of the incident flux and set its opening angle to 1° . To provide emittance a *light* modifier defining (R,G,B) values of (100, 100, 100) is assigned. All surfaces are modeled in RADIANCE as *plastic* with specularity and roughness both equal to zero. The absorbing measurement planes are defined with (R,G,B) values of (0, 0, 0), the reflecting surface S_2 with (0.8, 0.8, 0.8) for scenario 1, and with (0.3, 0.3, 0.3) for scenarios 2 and 3.

The simulation results are compared to the analytical reference values using the fraction

$$E/(E_{hz} \cdot \rho), \quad (1.1)$$

which is independent of the illuminance E_{hz} that is received at the reflecting surface S_2 . This fraction, where E denotes the illuminance at the particular measurement point and ρ is the reflectance of S_2 , equals the configuration factor F_{12} between the measurement point and the reflecting surface S_2 .

The configuration factor F_{12} is defined by the equation $E_1 = M_2 \cdot F_{12}$, where E_1 is the direct illuminance at an elementary receiving surface dS_1 (representing the measurement point) received from a diffuse area light source S_2 , M_2 is the luminous emittance of S_2 , and F_{12} is the configuration factor between dS_1 and S_2 . With the following equations 1.2 and 1.3 the configuration factor F_{12} can be calculated.

To quote from [CIE06]:

“In the case of an area light source parallel to the receiving surface, the configuration factor F_{12} between the elementary receiving surface dS_1 and the area source S_2 is given by the following relation:

$$F_{12} = \frac{1}{2\pi} \cdot \left[\frac{X}{\sqrt{1+X^2}} \cdot \arctan\left(\frac{Y}{\sqrt{1+X^2}}\right) + \frac{Y}{\sqrt{1+Y^2}} \cdot \arctan\left(\frac{X}{\sqrt{1+Y^2}}\right) \right], \quad (1.2)$$

1 Validation of RADIANCE Against CIE 171:2006 Test Cases

where $X = a/h$, $Y = b/h$, and a, b and h are shown in Fig. 1.2(a).

In the case of an area light source perpendicular to the receiving point, the configuration factor F_{12} between the elementary receiving surface dS_1 and the area source S_2 is given by the following relation:

$$F_{12} = \frac{1}{2\pi} \cdot \left[\arctan(Y) - \frac{1}{\sqrt{1+X^2}} \cdot \arctan\left(\frac{Y}{\sqrt{1+X^2}}\right) \right], \quad (1.3)$$

where $X = a/h$, $Y = b/h$, and a, b and h are shown in Fig. 1.2(b)."

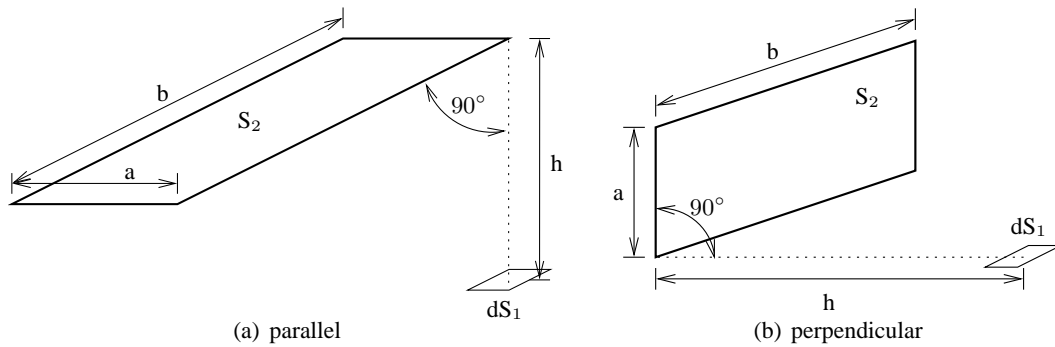


Figure 1.2: Configuration factor calculation in case of (a) parallel surfaces and (b) perpendicular surfaces.

General information about configuration factors can be found for example in [LH54] and [BS06].

Scenario 1

Figure 1.3(a) shows the set-up of the first scenario of test case 5.6. The square reflecting surface S_2 has a side length of 50cm and is centered under the ceiling, which is the horizontal measurement plane S_{1-hz} having a dimension of 4m \times 4m. S_2 is modeled as ideally diffuse surface having a reflectance of 80% and receives uniform direct illuminance at an incident angle of 45°. The measurement planes S_{1-v} (4m wide, 3m high) and S_{1-hz} are surrounded by an additional perfectly absorbing envelope that avoids direct illumination and light leakage artifacts. Figure 1.3(b) shows the locations of the equally spaced measurement points on S_{1-v} and S_{1-hz} .

For the RADIANCE calculations with *rtrace* some parameters need to be changed from their default values:

```
-ab 1 -aa 0 -ad 100000 -lw 0 -lr 1
```

With *-ab 1* the number of ambient (i.e. diffuse) reflections is limited to 1 and with *-aa 0* irradiance caching is switched off. This is useful here because the total number of rays in this scene with 14 measurement points and only one reflection is fairly small and thus the calculation is faster and more accurate. With *-ad 100000* every ray spawns approximately 100k rays to sample the hemisphere for the calculation of a diffuse reflection. A high number for *-ad* is important to

1.2 Proposed Test Cases with Analytical References

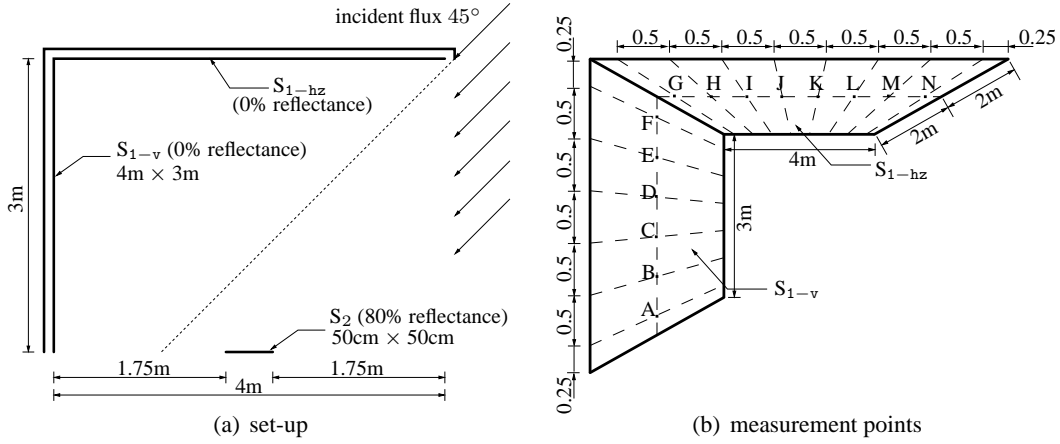


Figure 1.3: (a) Set-up of CIE test case 5.6, scenario 1, with reflecting surface S_2 , measurement planes S_{1-v} and S_{1-hz} , and indicated incident flux from a distant light source and (b) locations of measurement points A – N on surfaces S_{1-v} and S_{1-hz} .

ensure that a sufficient number of rays hit the reflecting surface. For *-ab 1* a large number of ambient divisions (*-ad*) is applicable, but due to exponential growth care should be taken for *-ab* settings higher than 1 to avoid enormous rendering times. Because the weight of a ray is split between all spawned rays the weight limit needs to be removed by *-lw 0* to avoid termination. Additionally, the maximum number of reflections *-lr* has to be set to a value greater than zero

		Points of measurement for S_{1-v}					
$E/(E_{hz} \cdot \rho)(\%)$	A	B	C	D	E	F	
CIE	0.246	0.580	0.644	0.556	0.433	0.325	
RADIANCE	0.250	0.583	0.650	0.565	0.441	0.321	
rel. error (%)	1.63	0.52	0.93	1.62	1.85	-1.23	

		Points of measurement for S_{1-hz}							
$E/(E_{hz} \cdot \rho)(\%)$	G	H	I	J	K	L	M	N	
CIE	0.491	0.639	0.778	0.864	0.864	0.778	0.639	0.491	
RADIANCE	0.488	0.640	0.774	0.861	0.863	0.780	0.641	0.488	
rel. error (%)	-0.61	0.16	-0.51	-0.35	-0.12	0.26	0.31	-0.61	

Table 1.7: Results for CIE test case 5.6, scenario 1: Variation of $E/(E_{hz} \cdot \rho)$ with $\rho = 0.8$ for S_2 of 50cm \times 50cm.

1 Validation of RADIANCE Against CIE 171:2006 Test Cases

to switch of Russian roulette that cannot be applied if the limit of a ray's weight is zero. As all surfaces are lambertian and $-ab$ is 1, $-lr$ is sufficient.

In Table 1.7 the results from the *rtrace* calculations with RADIANCE are opposed to the CIE reference values given in [CIE06]. Additionally, the relative errors between the reference and the calculated values are depicted. The mean rendering time was approximately 0.07 seconds per measurement point. For the first scenario RADIANCE with the specified settings for *rtrace* yields highly accurate results with relative deviations from the analytical references not higher than 1.85% for all 14 measurement points.

Scenario 2

Figure 1.4(a) shows the set-up of the second scenario of test case 5.6. The square reflecting surface S_2 with a size of $4\text{m} \times 4\text{m}$ is centered under the ceiling, which is the horizontal measurement plane S_{1-hz} having the same dimension. S_2 is modeled as ideally diffuse surface having a reflectance of 30% and receives uniform direct illuminance at an incident angle of 35° . The measurement planes S_{1-v} (4m wide, 2.5m high) and S_{1-hz} are surrounded by an additional perfectly absorbing envelope that avoids direct illumination and light leakage artifacts. Figure 1.4(b) shows the locations of the equally spaced measurement points on S_{1-v} and S_{1-hz} where the lowest point A is excluded to avoid direct illumination from the distant source.

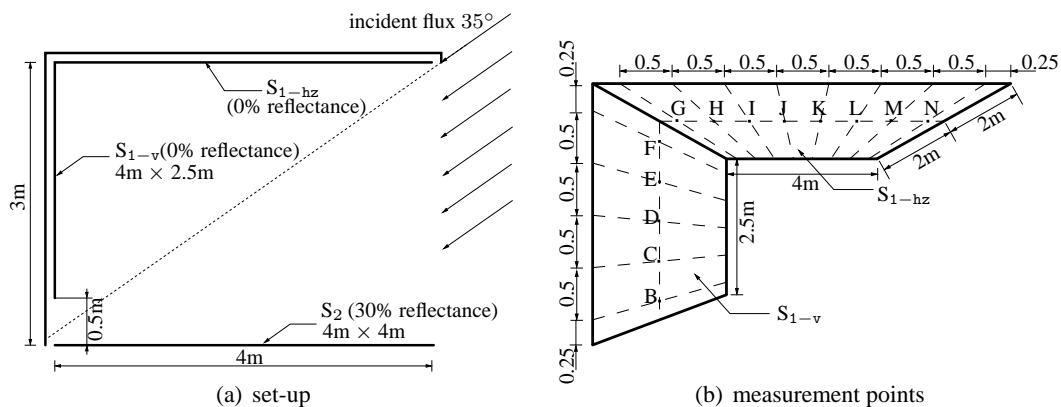


Figure 1.4: (a) Set-up of CIE test case 5.6, scenario 2, with reflecting surface S_2 , measurement planes S_{1-v} and S_{1-hz} , and indicated incident flux from a distant light source and (b) locations of measurement points B – N on surfaces S_{1-v} and S_{1-hz} .

To ensure high accuracy some parameters need to be changed from their default values for the RADIANCE calculations with *rtrace*. Thus we set them in the same way as described for scenario 1.

In Table 1.8 the results from the *rtrace* calculations with RADIANCE are opposed to the CIE reference values given in [CIE06]. Additionally, the relative errors between the reference and the calculated values are depicted. The mean rendering time was approximately 0.09 seconds per measurement point. For the second scenario RADIANCE with the specified settings

1.2 Proposed Test Cases with Analytical References

Points of measurement for S_{1-v}						
$E/(E_{\text{hz}} \cdot \rho)(\%)$	A	B	C	D	E	F
CIE	–	35.901	27.992	21.639	16.716	12.967
RADIANCE	–	35.911	27.937	21.592	16.744	12.979
rel. error (%)	–	0.03	-0.20	-0.22	0.17	0.09

Points of measurement for S_{1-hz}								
$E/(E_{\text{hz}} \cdot \rho)(\%)$	G	H	I	J	K	L	M	N
CIE	26.80	30.94	33.98	35.57	35.57	33.98	30.94	26.80
RADIANCE	26.80	30.95	33.96	35.56	35.57	33.96	30.92	26.80
rel. error (%)	0.00	0.03	-0.06	-0.03	0.00	-0.06	-0.06	0.00

Table 1.8: Results for CIE test case 5.6, scenario 2: Variation of $E/(E_{\text{hz}} \cdot \rho)$ with $\rho = 0.3$ for S_2 of $4\text{m} \times 4\text{m}$.

for *rtrace* yields highly accurate results with relative deviations from the analytical references smaller than 0.25% for all 13 measurement points.

Scenario 3

Figure 1.5 shows the set-up of the third scenario of test case 5.6. The square reflecting surface S_2 has a side length of 500m and is located outside of the “building” to represent the exterior ground. It is modeled as ideally diffuse surface having a reflectance of 30% and receives uniform direct illuminance at an incident angle of 45° .

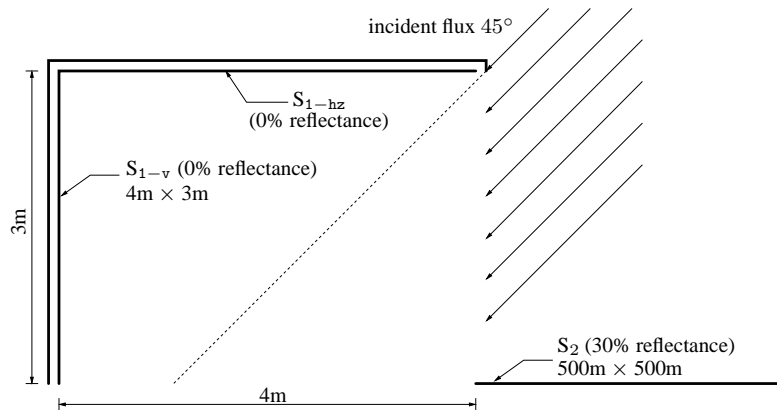


Figure 1.5: Set-up of CIE test case 5.6, scenario 3, with reflecting surface S_2 , measurement planes S_{1-v} and S_{1-hz} , and indicated incident flux from a distant light source.

1 Validation of RADIANCE Against CIE 171:2006 Test Cases

The horizontal measurement plane S_{1-hz} ($4m \times 4m$) and the vertical measurement plane S_{1-v} ($4m$ wide, $3m$ high) are surrounded by an additional perfectly absorbing envelope that avoids direct illumination and light leakage artifacts. The measurement points are equally spaced on S_{1-v} and S_{1-hz} and are located at the same positions as in scenario 1 (see Fig. 1.3(b)). For the same reasons as described for scenarios 1 and 2 we change some *rtrace* parameters from their default values to the settings as specified in scenario 1.

	Points of measurement for S_{1-v}					
$E/(E_{hz} \cdot \rho)(\%)$	A	B	C	D	E	F
CIE	3.080	9.097	14.718	19.767	24.161	27.896
RADIANCE	3.004	9.107	14.760	19.719	24.172	27.956
rel. error (%)	-2.47	0.11	0.29	-0.24	0.05	0.22

	Points of measurement for S_{1-hz}							
$E/(E_{hz} \cdot \rho)(\%)$	G	H	I	J	K	L	M	N
CIE	10.95	13.26	16.21	20.00	24.80	30.77	37.87	45.84
RADIANCE	10.94	13.26	16.20	20.00	24.80	30.78	37.86	45.83
rel. error (%)	-0.09	0.00	-0.06	0.00	0.00	0.03	-0.03	-0.02

Table 1.9: Results for CIE test case 5.6, scenario 3: Variation of $E/(E_{hz} \cdot \rho)$ with $\rho = 0.3$ for S_2 of $500m \times 500m$.

In Table 1.9 the results from the *rtrace* calculations with RADIANCE are opposed to the CIE reference values given in [CIE06]. Additionally, the relative errors between the reference and the calculated values are depicted. The mean rendering time was approximately 0.08 seconds per measurement point. For the third scenario RADIANCE with the specified settings for *rtrace* yields highly accurate results with relative deviations from the analytical references not greater than 2.5% for any of the 14 measurement points.

1.2.2 Test case 5.7 – Diffuse reflection with internal obstructions

With this test case the capability of a lighting simulation program to correctly account for obstructions in the calculation of diffusely reflected light is assessed. This is important because shading elements such as furniture or exterior objects that obstruct reflections from the ground appear in most simulated scenes.

The scene consists of a vertical plane S_2 ($4m \times 3m$) that is perfectly diffuse and spectrally neutral with a reflectance of 60%. S_2 receives uniform direct illuminance from a distant light source (e.g. the sun) at an incident angle of 60° . Two measurement planes – one horizontal S_{1-hz} ($2.5m \times 4m$) and one vertical S_{1-v} ($4m \times 3m$) – are modeled as perfect absorbers with a reflectance of 0%. Both are not directly illuminated by the light source but only receive indirect illumination from the diffuse reflection on S_2 . S_{1-hz} and S_{1-v} are surrounded by an absorbing

1.2 Proposed Test Cases with Analytical References

envelope that avoids direct illumination and light leakage artifacts. Between the reflecting surface S_2 and the measurement planes a vertical obstruction ($4\text{m} \times 1\text{m}$, 0.2m thick) is positioned that introduces some shading on $S_{1\text{-hz}}$ and $S_{1\text{-v}}$. Figure 1.6(a) shows the set-up of the scene and Figure 1.6(b) gives the positions of the measurement points that are equally spaced on the surfaces $S_{1\text{-hz}}$ and $S_{1\text{-v}}$. The RADIANCE modeling is done similarly as for test case 5.6 with the only difference that the color of S_2 is set to $(0.6, 0.6, 0.6)$.

Again the simulation results are compared to the analytical reference values using the configuration factor

$$E/(E_v \cdot \rho), \quad (1.4)$$

where E is the illuminance at the particular measurement point, E_v is the received illuminance at the reflecting surface S_2 , and ρ is the reflectance of S_2 , which is 0.6 in this test case.

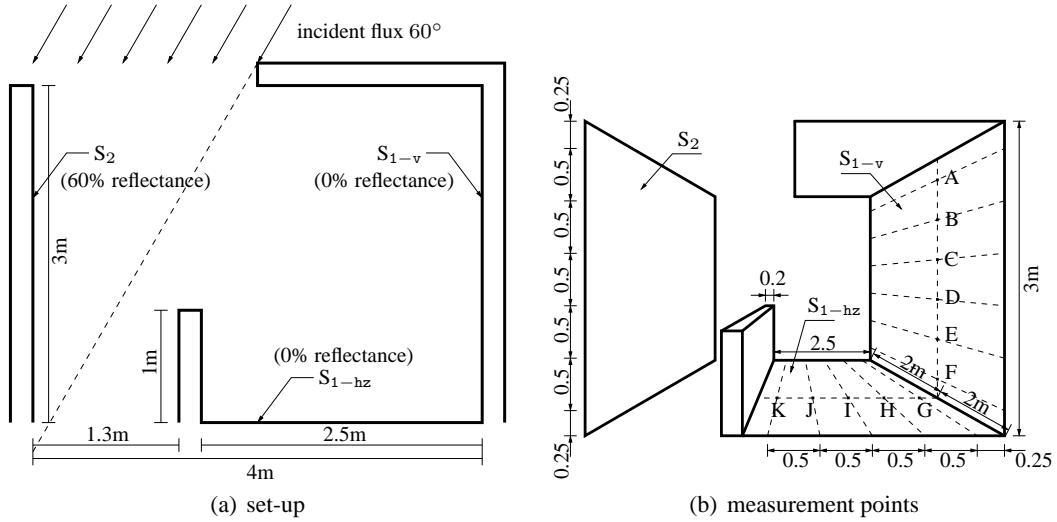


Figure 1.6: (a) Set-up of CIE test case 5.7 with reflecting surface S_2 , measurement planes $S_{1\text{-v}}$ and $S_{1\text{-hz}}$, and indicated incident flux from a distant light source and (b) locations of measurement points A – K on surfaces $S_{1\text{-v}}$ and $S_{1\text{-hz}}$.

For the same reasons as described in scenario 1 of test case 5.6 we change some *rtrace* parameters from their default values for the RADIANCE calculations:

```
-ab 1 -aa 0 -ad 100000 -lw 0 -lr 1.
```

The first results that we obtained from our RADIANCE calculations suggested to check the correctness of the CIE reference values. The authors of [Dau07] also mention that the values in Table 19 in [CIE06] are not correct. However, their presented values seem to be wrong as well. Therefore we recalculate the configuration factors $E/(E_v \cdot \rho)$ using equations 1.2 and 1.3 and obtain results that differ from the values published by the CIE in Table 19 in [CIE06].

In Table 1.10 the results from the RADIANCE simulations are opposed to the CIE data and our recalculated values (“analytical”). Additionally, the relative errors between the simulation

1 Validation of RADIANCE Against CIE 171:2006 Test Cases

	Points of measurement for S_{1-v}					
$E/(E_v \cdot \rho)(\%)$	A	B	C	D	E	F
CIE reference	20.941	21.187	19.946	17.284	14.053	9.751
analytical	16.071	16.330	15.399	13.322	10.317	7.079
RADIANCE	16.080	16.343	15.395	13.331	10.313	7.071
rel. error (%)	0.06	0.08	-0.03	-0.07	-0.04	-0.11

	Points of measurement for S_{1-hz}				
$E/(E_v \cdot \rho)(\%)$	G	H	I	J	K
CIE reference	4.761	5.261	4.535	0.000	0.000
analytical	3.382	3.629	3.013	0.000	0.000
RADIANCE	3.366	3.614	3.009	0.000	0.000
rel. error (%)	-0.47	-0.41	-0.13	0.00	0.00

Table 1.10: Results for CIE test case 5.7: Variation of $E/(E_v \cdot \rho)$ for the test case with internal obstruction. In addition to the CIE reference values the recalculated analytical values are shown.

results and the recalculated analytical values are depicted. The mean rendering time was approximately 0.12 seconds per measurement point. For this test scene 5.7 RADIANCE with the specified settings for *rtrace* yields highly accurate results with relative deviations from the analytical references smaller than 0.5% for all 11 measurement points.

1.2.3 Test case 5.8 – Internal reflected component calculation for diffuse surfaces

With this test case the capability to correctly simulate diffuse interreflections inside a room is assessed. This is important because internal surfaces such as walls or ceilings are usually modeled to be lambertian and yield an important contribution to global illumination.

The test scene set-up is a cubical-shaped room (4 m×4 m×4 m) where all surfaces are perfectly diffuse and spectrally neutral with a reflectance ρ varying from 0% to 95%. The illumination comes from an isotropic point light source that is positioned at the center of the room and has an output flux Φ of 10000lm. In RADIANCE the surfaces are modeled as *plastic* with RGB values (ρ, ρ, ρ) and specularity and roughness both equal to zero. Because RADIANCE does not provide point light sources, the lamp is simulated as sphere with a radius of 1cm, where the RADIANCE primitive *light* with the modifier *void* is assigned to provide diffuse emittance. For the light source we obtain an RGB value of (14151, 14151, 14151) using RADIANCE's *lampcolor* routine.

The simulation results are compared to the analytical references in terms of the average indirect illuminance E_{av} inside the room. Because the room is cubical the average indirect illu-

minance at each of the six surfaces is the same. To save computation time the RADIANCE simulation is limited to a regular 20×20 grid of measurement points on one of the surfaces and E_{av} is computed as mean of all 400 calculated illuminances. For the *rtrace* calculations some parameters need to be changed from their default values:

$$-dt 0 -aa 0.08 -ar 0 -ab n -lr n -lw 0.$$

For this test scene – especially for high values of ρ – setting the direct threshold *-dt* to zero is important. Otherwise multiple reflected rays with low weights ($w = \rho^r$ for r reflections) fail at the threshold check in the *direct()* function in RADIANCE’s *source.c* and do not contribute to the indirect illuminance. With setting *-dt* to zero any contribution is computed and added to the global illumination. The parameters *-aa* and *-ar* are set to the specified values to limit the error that might be introduced through the irradiance caching algorithm. Due to the high number of reflections that would result in enormous rendering times, irradiance caching cannot be switched off (*-aa 0*) for this test case as it is done in test cases 5.6 and 5.7. The number of ambient bounces *-ab* is set to the smallest integer n providing $\rho^n \leq 0.01$ to limit the termination of multiple reflected rays to those that contribute less than 1% of the direct lighting. To really allow n reflections for each ray, the limit *-lr* is set to n and the limit of a ray’s weight *-lw* is set to zero.

ρ	0.00	0.05	0.10	0.20	0.30	0.40	0.50	0.60	0.70	0.80	0.90	0.95
$E_{av}(lx)$ CIE	0.00	5.48	11.6	26.0	44.6	69.4	104	156	243	417	937	1979
RADIANCE	0.00	5.48	11.5	25.9	44.5	69.5	104	156	243	418	943	2006
rel.error (%)	0.0	0.0	-0.9	-0.4	-0.2	0.1	0.0	0.0	0.0	0.2	0.64	1.4
n	1	2	2	3	4	6	7	10	13	21	44	90
time (sec)	0.59	16.5	16.4	66.4	107	119	121	126	129	133	151	177

Table 1.11: Results for CIE test case 5.8: Indirect average illuminance variation with average reflectance.

In Table 1.11 the results from the RADIANCE simulations are opposed to the data presented by the CIE in Table 20 of [CIE06]. Additionally, the relative errors between the simulation results and the analytical values, the number of ambient bounces *-ab* n , and the rendering times are depicted. For reflectances up to 90% RADIANCE with the specified settings for *rtrace* yields highly accurate results with relative deviations from the analytical references smaller than 1% and even for $\rho = 0.95$ the accuracy of the simulation is high with an error of only 1.4%.

1.3 Conclusion

In this chapter we assessed the accuracy of RADIANCE using the six experimental test cases and three scenes with analytical references as proposed by the CIE [CIE06]. Generally, calculations with RADIANCE yield highly accurate results if appropriate parameter settings for *rtrace* are selected. Considering the test cases with analytical references the relative deviations of our

1 Validation of RADIANCE Against CIE 171:2006 Test Cases

RADIANCE results from the given reference data is smaller than 2.5% in all scenes. Test case 5.8 and especially the scenes with high reflectances show that RADIANCE delivers highly accurate results even for scenarios where the ray tracing approach that approximates the Neumann series solution of the rendering equation, is slowly convergent.

For the experimental test cases RADIANCE performs very well in the scenes with point and rectangular area light sources (test cases 4.1, 4.3, 4.4, and 4.6), whereas it shows weaknesses in the simulation of circular area light sources (test cases 4.2 and 4.5). Therefore we developed an improved subdivision algorithm for circular light sources that significantly increases the accuracy of the simulations. We present this subdivision approach in the following Section 2.1.

2 Improvements in the Accuracy of Computational Methods in RADIANCE

Divide et impera!

(Louis XI of France,
1423-1483)

2.1 Sampling of Circular Area Light Sources

In Chapter 1 the CIE experimental test case 4.2 discovers a shortcoming of RADIANCE in the modeling of circular light sources. Thus we investigate the adaptive source subdivision algorithm that is implemented in *srcsamp.c* of the source code and propose an improved subdivision method for disk shaped luminaires.

2.1.1 Adaptive Source Subdivision in RADIANCE

Usually, in RADIANCE one single sample ray is traced per light source to compute the direct lighting contribution at the current position. For large area light sources this may introduce severe inaccuracies due to partial occlusion or a poor estimation of the solid angle covered by the luminaire. One approach would be to sample the light source adequately by using many rays that are distributed according to the luminaire's shape. However, these sampling methods as described for example by Shirley, Wang, and Zimmerman [SWZ96] are computationally demanding.

In version 3.8 of RADIANCE a more robust approach called “adaptive source subdivision” is implemented (see [WS98]). Basically, a large area light source is repeatedly subdivided into two parts until the size of each single segment relative to the distance to the current position is small enough. In Algorithm 2.1 we briefly describe the main steps that are performed in RADIANCE when a flat area light source is subdivided. The threshold for the abort criterion (*size of longest axis of source* \div *distance from source to current position*) can be steered by the user via the parameter *-ds*. The lower this value is, the more subdivisions and thus sample rays for each light source are calculated, bounded by the macro `MAXSPART` that is defined as $64 = 2^6 = 2^d$ (for a maximum subdivision depth $d = 6$) in *source.h*. Setting *-ds* to zero switches this algorithm off and thus allows fast but maybe inaccurate renderings.

The method described in Algorithm 2.1 approximates all flat area light sources as rectangles having the same area as the luminaire. Thus, the partition of every flat light source comprises solely rectangular subsources. After the subdivision one sample ray is traced from the current position to each subsource. Additionally, the user is able to steer the degree of direct jittering around the center of the subsource with the parameter *-dj*. The sample position (s_1, s_2) at the

Algorithm 2.1 Adaptive source subdivision for disk area light sources implemented in *srcsamp.c* in version 3.8 of RADIANCE.

```

FLATPART (srcindex si, ray r)
    approximate disk by a square;
    if ([size of longest axis of square ÷ distance from source to current position] too large)
        then
            subdivide source into two parts along the longest axis;
        else
            write partition structure (i.e., non-divided source) to si;
            return ;

    for each part
        do
            while ([size of longest axis of part ÷ distance to current part] too large
                    and maximum number of parts not yet reached)
                recursively repeat subdivision for each part;

    write partition structure to si;
    return ;

```

light source is calculated as

$$(s_1, s_2) = \left(c_1 + dj \cdot (1 - 2 \cdot x) \cdot \frac{r_1}{2}, c_2 + dj \cdot (1 - 2 \cdot y) \cdot \frac{r_2}{2} \right), \quad (2.1)$$

where (c_1, c_2) is the center of the rectangular subsurface, r_1 and r_2 are the side lengths of the rectangle, and x and y are independent random numbers with uniform distribution in the real interval $[0, 1]$. Thus, if $-dj$ is set to 0 each sample ray is traced to the center of the particular subsurface, i.e., to the center of the rectangle. With setting $-dj$ to 1 the sample rays are distributed over the full rectangular source volume.

This subdivision approach fits well for roughly rectangular light sources, but is problematic for other shapes such as triangles or disks. Figure 2.1 exemplifies this issue for a disk light source that is overlaid by the sampling square and a possible partition. In the example of Figure 2.1 ten sample rays would be sent to the light source. Assuming that $-dj$ is set to 0, the ray that is traced to the upper right corner of the rectangle would miss the luminaire volume and lead to an “aiming failure for light source” warning.

Generally, if a circular light source is subdivided into 64 subsurfaces (current setting of MAXSPART) and $-dj$ is zero, 4 out of 64 or 6.25% of the sample rays miss the target volume of the luminaire. Because these rays’ contributions are not computed, the calculated direct illumination at the current position from the light source is too low. Actually, if the full rectangular volume is sampled ($-dj$ 1), the expected value for the number of rays that miss the disk light source and report an aiming failure is 9.06%.

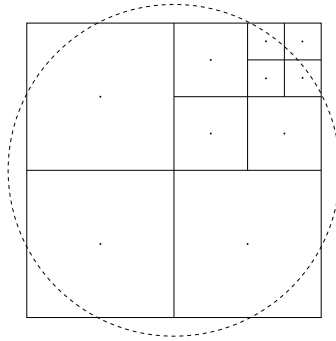


Figure 2.1: Adaptive source subdivision for circular light sources in standard RADIANCE. The circular area light source (stippled) is sampled by using the partition of the approximating square.

2.1.2 Improved Adaptive Subdivision of Circular Light Sources

Motivated by the imprecise RADIANCE results for the experimental CIE test cases 4.2 and 4.5 with disk luminaires (see Sections 1.1.2 and 1.1.5) we look for an improved subdivision algorithm for circular area light sources. To enable a fairly simple implementation in RADIANCE we try to keep the algorithm similar to the existing one and to still keep it adaptive. The basic idea is to triangulate the disk, what is a standard approach in computer graphics. However, using an equilateral triangle to approximate the disk would be even worse than using a square. Thus we approximate the circular light source by an equilateral hexagon that can be split up into six equilateral triangles in the first subdivision step (see left image in Figure 2.2). These triangles can then be subdivided adaptively into four equilateral triangles having the half side length. Algorithm 2.2 describes the procedure for our improved adaptive subdivision of circular light sources, which we call RINGPART because of the ring geometry that is used in RADIANCE to model disks.

A main issue for the implementation of our improved algorithm in RADIANCE is to find a clever way of traversing the – maybe differently sized – triangular elements of the source partition. Lee and Samet [LS98] present a triangle labeling method that we adopt for our subdivision algorithm. The basic idea is to use the fact that one sub-triangle is oriented in the same way as the initial triangle, whereas the other three sub-triangles are reversely oriented.

For our algorithm it is important to know the center points of the single triangles where – for now without jittering – the sample rays shall be sent. Because under an affine transformation the center of a triangle remains the transformed triangle’s center, we can perform all calculations based on a standard isosceles rectangular triangle where the length of the legs l is 1 (see Figure 2.2 center and right).

With the affine transformation a every point in the standard rectangular triangle can be mapped to the equilateral sampling triangle. Thus, the center c_0 can be computed from m using

$$a(x, y) = c + x \cdot u + y \cdot w, \quad (2.2)$$

i.e., for the center $c_0 = c + m_x \cdot u + m_y \cdot w,$

Algorithm 2.2 Improved adaptive subdivision for circular light sources.

```

RINGPART (srcindex si, ray r)
  approximate disk by an equilateral hexagon;
  if ([size of longest axis of hexagon ÷ distance from source to current position] too large)
    then
      subdivide hexagon into 6 equilateral triangles;
    else
      write partition structure (i.e., non-divided source) to si;
      return ;

  for each triangle
    do
      while ([size of triangle side length ÷ distance to current part] too large)
        and maximum number of parts not yet reached)
          recursively subdivide into 4 equilateral triangles;

  write partition structure to si;
  return ;

```

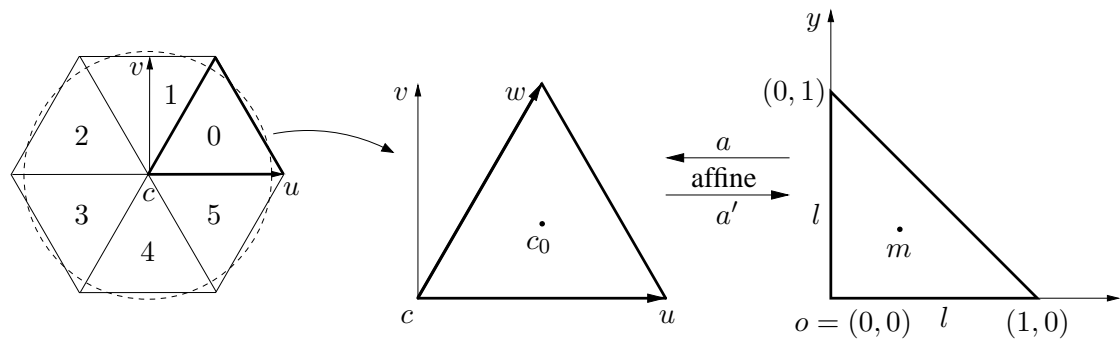


Figure 2.2: Hexagonal approximation of a disk light source (left) and affine transformation from an equilateral to a standard isosceles rectangular triangle and vice versa (center and right).

where $w = v + u/2$ and u and v are the local coordinates of the hexagon that approximates the disk light source (see Figure 2.2, left).

In the rectangular triangle in Figure 2.2 (right) we can calculate the center point m from its rectangular corner o and the length of the leg l as

$$m = o + \frac{l}{3}(1, 1). \quad (2.3)$$

If the relative size criterion is met in the algorithm, the equilateral triangle shall be subdivided

into four small equilateral triangles. Again we perform the calculations in the rectangular triangle and receive the four midpoints that can then be mapped to the center of the corresponding equilateral triangle by Equation 2.2. Figure 2.3(a) shows the standard rectangular triangle ($l = 1$) partitioned into four rectangular triangles together with their midpoints m_i , rectangular corners o_i , and legs l_i (for $i = 0, 1, 2, 3$). Numbering the rectangular corners counterclockwise leads to the labeling as proposed by Lee and Samet [LS98] that allows a structured traversal of the triangles.

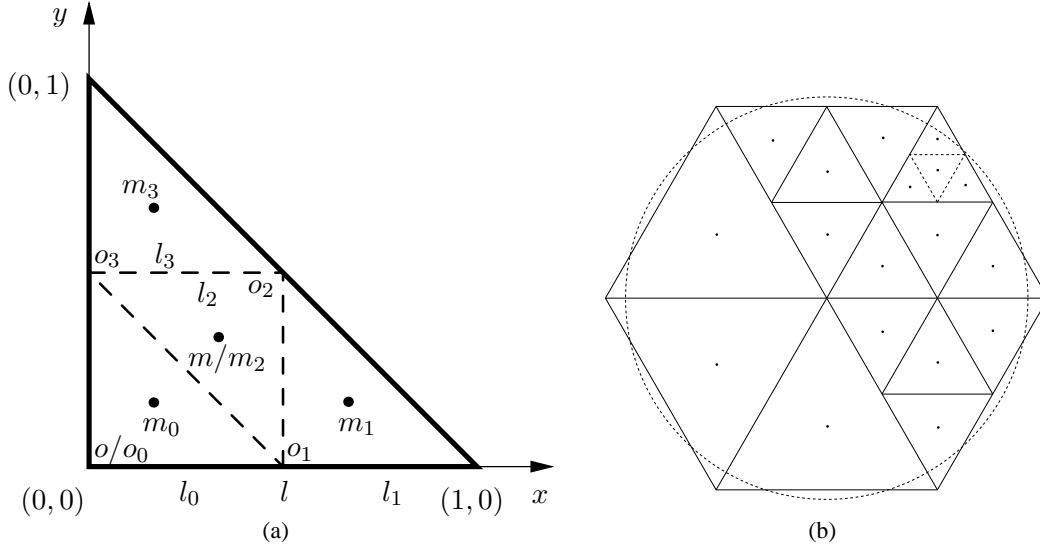


Figure 2.3: Improved adaptive subdivision for circular light sources: (a) subdivision of a standard isosceles right-angled triangle and (b) possible partition for sampling a disk-shaped luminaire.

For each single rectangular sub-triangle the position of the rectangular corner o_i and the length of the legs l_i can be calculated by Equations 2.4 to 2.7. Care has to be taken that the “length” of the center sub-triangle’s leg l_2 is set to a negative value due to the reverse orientation and the usage of l in Equation 2.3. Recursively applying Equations 2.4 to 2.7, further subdivisions of the rectangles can easily be computed.

$$o_0 = o, \quad l_0 = \frac{l}{2} \quad (2.4)$$

$$o_1 = o + \frac{l}{2}(1, 0), \quad l_1 = \frac{l}{2} \quad (2.5)$$

$$o_2 = o + \frac{l}{2}(1, 1), \quad l_2 = -\frac{l}{2} \quad (2.6)$$

$$o_3 = o + \frac{l}{2}(0, 1), \quad l_3 = \frac{l}{2} \quad (2.7)$$

Using Equations 2.3 and 2.2, the midpoint of each equilateral triangle can be computed and used

in the direct illumination calculation to sample the light source. Figure 2.4 exemplifies the three main steps of our improved adaptive subdivision algorithm and Figure 2.3(b) shows a possible partition for sampling a circular area light source.

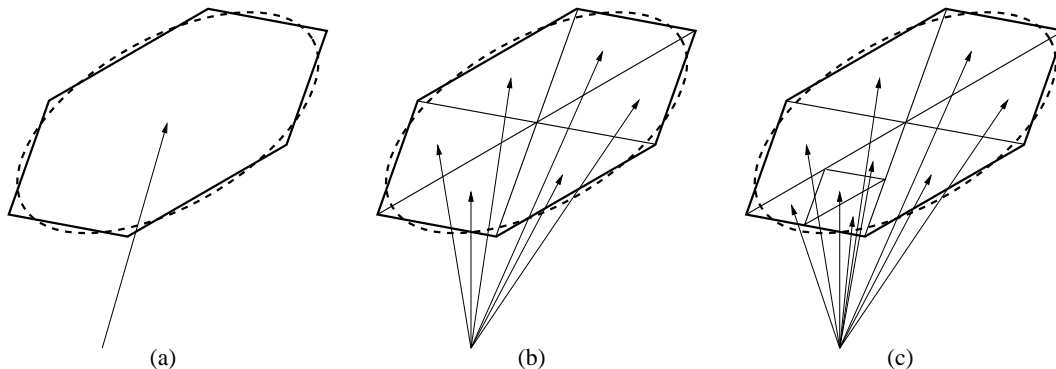


Figure 2.4: Main steps of the improved adaptive subdivision algorithm: (a) approximate circular light source by a hexagon, (b) subdivide hexagon into six equilateral triangles, and (c) recursively subdivide triangles into smaller equilateral triangles.

To enable the simulation of soft shadows, jittering, i.e., randomly distributing the sample rays over the source volume, is necessary. We adapt the sampling approach proposed by Shirley, Wang, and Zimmerman [SWZ96] for jittering the sample rays for both the non-subdivided disk and the triangles and gain a jittering method that is similar to the one implemented in RADIANCE 3.8 (see Equation 2.1).

In case of a not subdivided disk a random sample position (s_1, s_2) can be calculated as

$$(s_1, s_2) = (c_1 + dj \cdot r \cdot \sqrt{x} \cdot \cos(2\pi y), c_2 + dj \cdot r \cdot \sqrt{x} \cdot \sin(2\pi y)), \quad (2.8)$$

where (c_1, c_2) is the center and r is the radius of the disk light source, and x and y are independent random numbers with uniform distribution in the real interval $[0, 1]$. Compared to [SWZ96] we introduce the factor dj to keep up the possibility for the user to decide if the sample ray is sent to the center ($-dj \ 0$), if it is randomly distributed in a region around the center ($0 < -dj < 1$), or if it is randomly distributed over the full source volume ($-dj \ 1$).

If the disk light source is subdivided into equilateral triangles we use a jittering based on barycentric coordinates that is similar to the sampling approach for triangles in [SWZ96]. In this case a jittered position $s = (s_1, s_2)$ inside the triangle can be computed as

$$s = m + dj \cdot y \cdot \sqrt{1-x} \cdot u + dj \cdot (1 - \sqrt{1-x}) \cdot w, \quad (2.9)$$

where m is the midpoint of the triangle, u and w are vectors that represent two sides of the triangle (see Figure 2.2), and x and y are independent random numbers with uniform distribution in the real interval $[0, 1]$. Again, we introduce the factor dj to allow a user-defined degree of jittering.

2.1 Sampling of Circular Area Light Sources

To limit the number of subdivisions in our new algorithm we define a macro `MAXTRISPART` similar to `MAXSPART` in `source.h` (see above). For a maximum subdivision depth d we set `MAXTRISPART` = $6 \cdot 2^{\lfloor \frac{d-1}{2} \rfloor}$, i.e., to 96 for the default value of $d = 6$ in version 3.8 of `RADIANCE`. With this settings and switched off jittering (`-dj 0`), all 96 sample rays of a fully subdivided disk hit the circular volume of the luminaire. Conversely, if the full hexagonal area is sampled (`-dj 1`), the expected value for the number of rays that miss the target volume is 3.72%. This is a decrease of aiming failures by a factor of 2.43 compared to the 9.06% of the standard approach.

Analytical test scene

The illuminance under a perfectly diffuse emitting disk can be computed as

$$E = L_0 \cdot \pi \cdot \frac{r^2}{r^2 + h^2} = \frac{\Phi}{\pi(r^2 + h^2)}, \quad (2.10)$$

where E [lux] is the illuminance at the measurement point P located perpendicular below the center of the disk, h [m] is the distance between P and the light source, r [m] is the radius of the disk, L_0 [cd/m²] is the luminance, and Φ [lm] is the total luminous flux of the light source (see Figure 2.5).

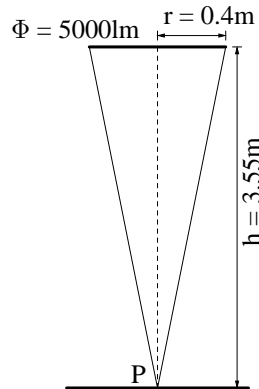


Figure 2.5: Analytical test scene.

Adopted from the real-world seminar room that we use as test scene in Chapter 3, we define the disk luminaire with a radius of 0.4 m and at a (room) height of 3.55 m. For the total luminous flux Φ of the circular light source we chose 5000 lm. The analytical solution for the illuminance at point P can then easily be computed from Equation 2.10 as

$$E = \frac{5000 \text{ lm}}{\pi(0.4^2 + 3.55^2) \text{ m}^2} = 124.705 \text{ lux.}$$

In Table 2.1 we compare the calculation results from both `RADIANCE 3.8` and our improved subdivision algorithm for the analytical test scene. In both cases we change some `rtrace` parameters from their default values:

2 Improvements in the Accuracy of Computational Methods in RADIANCE

$$-dt\ 0\ -ds\ 0.02\ -dj\ 0/1.$$

With setting $-dt$ to zero the “selective shadow testing algorithm” in RADIANCE (see [WS98]) is switched off. Thus every direct contribution is accounted for, even for the small parts of the – due to $-ds\ 0.02$ – finely subdivided light source. For the value of the parameter $-dj$ we choose the two extrema 0 and 1 to show the differences between tracing the sample rays to the centers of the subsources and distributing the samples over the full source volume.

Algorithm	$-dj$	E [lux]	rel. error (%)	exp. error (%)	partition	remarks
analytical	–	124.705	—	—	—	—
RADIANCE 3.8	0	117.007	-6.17	-6.25	64 □	aiming failure
	1	111.184	-10.84	-9.06	64 □	aiming failure
our subdivision	0	124.720	0.01	0.00	96 △	—
	1	120.856	-3.09	-3.72	96 △	aiming failure

Table 2.1: Analytical test scene results and relative errors obtained from calculations with standard RADIANCE 3.8 and with our improved subdivision algorithm opposed to the analytical value.

The results in Table 2.1 show that our proposed improved subdivision algorithm for circular light sources reduces the relative error in this analytical test scene by $\sim 6\%$ for both parameter settings for $-dj$. All relative errors match the expected errors well, where we have to keep in mind that for $-dj\ 1$ variations are introduced by randomly distributing the samples over the light source area. The results for the CIE experimental test cases 4.2 and 4.5 in Tables 1.2 and 1.5 (mean room illuminance) as well as A.2 and A.5 (point illuminances) that motivated us to investigate Ward’s “adaptive source subdivision” algorithm, show similar behaviours. For example the mean room illuminances increased from 51.5 lux with RADIANCE 3.8 to 54.1 lux (+5.05%) in test case 4.2 (Table 1.2) and from 40.5 lux to 43.1 lux (+6.42%) in test case 4.5 (Table 1.5), respectively, with our proposed subdivision algorithm.

2.1.3 Alternative Solution in RADIANCE 3.9

After some discussions about our proposal for an improved light source subdivision [War08], Greg Ward implemented an alternative approach in the current version 3.9 of RADIANCE (see CVS on [Rad10]). The basic idea is to map the calculated sample position (s_1, s_2) from the square to a position (s'_1, s'_2) at the disk (see Figure 2.6) using the transformation

$$(s'_1, s'_2) = \left(s_1 \sqrt{1 - \frac{s_2^2}{2}}, s_2 \sqrt{1 - \frac{s_1^2}{2}} \right). \quad (2.11)$$

The benefits of this method are that aiming failures are avoided at all, its implementation is straightforward, and it is computationally faster than our triangulation approach.

2.1 Sampling of Circular Area Light Sources

However, using this “mapping squares to disks” approach, various problems arise. First, the resulting samples are not uniformly distributed over the disk volume. Regions around 45° , 135° , 225° , and 315° as well as near the boundary of the disk are sampled most densely, whereas the region around the center is undersampled. However, all samples have the same weight in the calculation, which means that they represent the same area. Viewing the partitioned light source from a point along its surface normal through the center (i.e., standing just under the source) will result in larger viewing angles (and therefore smaller cosines) for all samples that yields an undervaluation of the received illuminance (see Figure 2.6).

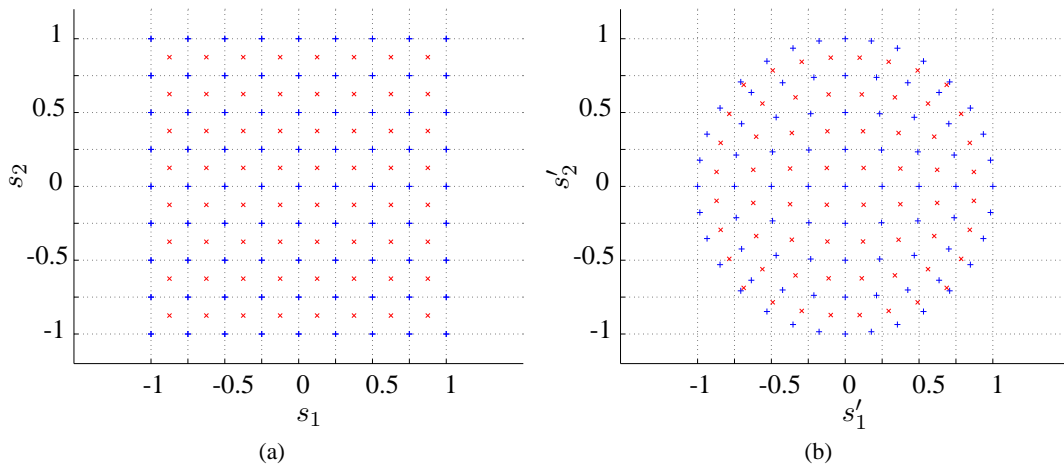


Figure 2.6: Adaptive subdivision of disk luminaires implemented in RADIANCE 3.9: the subdivided square (a) is mapped to the disk (b) using Equation 2.11.

Second, the resulting sample distribution is not rotationally symmetric. As pointed out above, samples accumulate around 45° , 135° , 225° , and 315° as well as close to the boundary of the disk. Thus, for light sources with non-symmetric luminous intensity distributions the non-uniform sampling may lead to even larger errors.

Third, the more subdivisions are allowed for a circular light source, the smaller a single partition region near the boundary gets. For the current setting of 64 for the macro `MAXSPART` it is not that bad, but allowing more subdivisions results in an even worse ratio between region areas near the center and those close to the boundary.

The image in Table 2.2 on the right shows an extreme example where the non-uniform sampling stated above introduces large errors. The results for this example are opposed to the analytical value in Table 2.2 (left). The *rtrace* parameters were set as stated above for the analytical test scene and *-dj* was kept at 0. For this example the drawback of the non-uniform sampling of the “mapping squares to disks” method (RADIANCE 3.9) is dominating and leads to errors that are nearly twice as high compared to the original approach (RADIANCE 3.8).

For Greg Ward the benefits that are mentioned above outweigh the discussed problems, especially because they hardly arise in real-world scenes [War08]. Thus he implemented the method of “mapping squares to disks” in the current version of RADIANCE (available at [Rad10]). We

2 Improvements in the Accuracy of Computational Methods in RADIANCE

Algorithm	E [lux]	error (%)	partition	remarks
analytical	795.77	—	—	—
RADIANCE 3.8	769.94	-3.25	64 \square	aiming failure
RADIANCE 3.9	744.81	-6.40	64 \square	—
our subdivision	796.87	0.14	96 \triangle	—

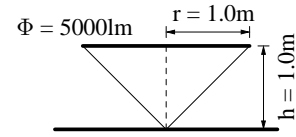


Table 2.2: Results for the test scene demonstrating the shortcomings of the “mapping squares to disks” approach implemented in RADIANCE 3.9.

tested his approach for the CIE experimental test case 4.2 (see Section 1.1.2) and received satisfying results that did not differ significantly from the values obtained with our proposed subdivision algorithm.

2.1.4 Conclusion

We presented an improved adaptive subdivision algorithm for circular light sources. The basic idea is to approximate a disk shaped luminaire by a hexagon that is adaptively subdivided into equilateral triangles instead of a square and its rectangular subdivisions. For a clever way of traversing the triangular elements we could use the labeling as proposed in [LS98].

With the proposed subdivision algorithm the relative error in the analytical test scene was reduced by $\sim 6\%$. Similarly, the mean room illuminances in the CIE test cases 4.2 and 4.5 were increased by 5.05% and 6.42%, respectively.

2.2 A New BRDF Model Based on the Ward-Dür BRDF

A bidirectional reflectance distribution function (BRDF) [NRH*77] $f(\theta_l, \phi_l; \theta_v, \phi_v)$ describes the reflectance properties of a surface by specifying the amount of radiance incident from direction (θ_l, ϕ_l) that is reflected into direction (θ_v, ϕ_v) , i.e.,

$$L_v(\theta_v, \phi_v) = \int_0^{2\pi} \int_0^{\pi/2} L_l(\theta_l, \phi_l) f(\theta_l, \phi_l; \theta_v, \phi_v) \cos \theta_l \sin \theta_l d\theta_l d\phi_l. \quad (2.12)$$

The main characteristics of a *physically plausible* BRDF are *Helmholtz reciprocity* and *energy conservation* [Lew94]. Helmholtz reciprocity stands for the symmetry between incident and reflected directions,

$$f(\theta_l, \phi_l; \theta_v, \phi_v) = f(\theta_v, \phi_v; \theta_l, \phi_l), \quad (2.13)$$

that allows global illumination calculations by backward ray tracing algorithms [Whi80]. Energy conservation – or *energy balance* – means that the *albedo*, i.e., the total reflected power for a given direction of incident radiation,

$$a(\theta_l, \phi_l) = \int_0^{2\pi} \int_0^{\pi/2} f(\theta_l, \phi_l; \theta_v, \phi_v) \cos \theta_v \sin \theta_v d\theta_v d\phi_v \quad (2.14)$$

is bounded by 1.

Over the last five decades numerous BRDF models were introduced. Beckmann [BS63] and Torrance and Sparrow [TS67] presented physically based microfacet BRDF models that use the Gaussian distribution to define the microfacets' surface normals. The model by Torrance and Sparrow was used in computer graphics by Cook and Torrance [CT81] and later improved by He et al. [HTSG91]. However, these models are neither suitable for Monte Carlo integration due to missing efficient importance sampling formulae, nor do they provide anisotropic reflection. The first empirical and probably most famous model that simulates specular reflections was introduced by Phong [Pho75] and later improved by Blinn [Bli77]. Other physically plausible BRDFs that model anisotropic reflection and are suitable for Monte Carlo integration were proposed by Schlick [Sch94], Lafortune et al. [LFTG97], Ashikmin and Shirley [AS00], and Kurt et al. [KSKK10].

As a simplification of the Cook-Torrance model, Ward [War92] presented an anisotropic BRDF that was later improved by Dür [Dür06]. The main benefits of this model are that it is computationally cheap to evaluate, it admits efficient importance sampling for Monte Carlo integration, and it is simple and intuitive to use with only two parameters for specularity and roughness. Neumann et al. [NNSK99] proposed modifications for the Phong, Blinn, and Ward models by adding correction terms to make them physically plausible.

2.2.1 The Ward-Dür BRDF and its Sampling

In [War92], Ward proposes a BRDF that models anisotropic specular reflection by

$$f_W(\theta_l, \phi_l; \theta_v, \phi_v) = \frac{\rho_s}{\pi\alpha\beta} \cdot \exp\left(-\tan^2 \delta \left(\frac{\cos^2 \phi}{\alpha^2} + \frac{\sin^2 \phi}{\beta^2}\right)\right) \cdot \frac{1}{4\sqrt{\cos \theta_l \cos \theta_v}}, \quad (2.15)$$

2 Improvements in the Accuracy of Computational Methods in RADIANCE

where $\theta_l, \phi_l; \theta_v, \phi_v$ and θ, ϕ denote the polar and azimuthal angles of the incident and reflected directions, and of the halfway vector, respectively (see Figure 2.7). The material properties are given by the *specular reflectance* ρ_s and the *roughness* values α and β that give the standard deviation of the surface slopes in the perpendicular directions \vec{x} and \vec{y} .

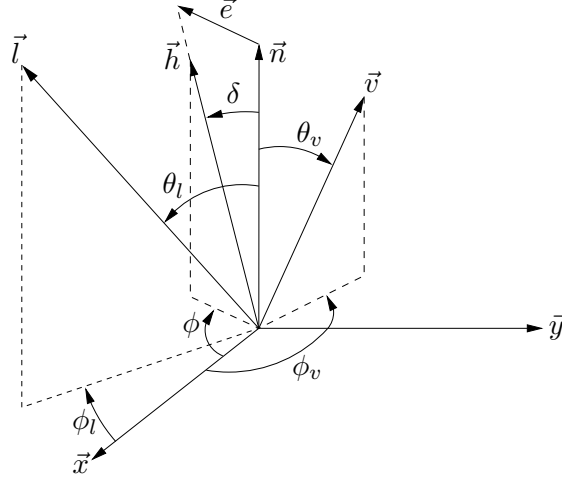


Figure 2.7: Notation used in this section: \vec{h} is the halfway vector, \vec{n} is the surface normal, \vec{v} is the view point direction, and \vec{l} is the light source or sampling direction. All vectors have unit length.

Based on investigations on the energy balance of Ward's reflection model, Dür [Dür06] presents an improved normalization for the Ward BRDF that we refer to as Ward-Dür BRDF:

$$f_{\text{WD}}(\theta_l, \phi_l; \theta_v, \phi_v) = \frac{\rho_s}{\pi\alpha\beta} \cdot \exp\left(-\tan^2 \delta \left(\frac{\cos^2 \phi}{\alpha^2} + \frac{\sin^2 \phi}{\beta^2}\right)\right) \cdot \frac{1}{4 \cos \theta_l \cos \theta_v}. \quad (2.16)$$

In RADIANCE the approach to calculate the specular reflected radiance is

$$\int_S L_l(\vec{l}) f_{\text{WD}}(\vec{l}, \vec{v}) d\Omega_l + \int_R L_l(\vec{l}) f_{\text{WD}}(\vec{l}, \vec{v}) d\Omega_l, \quad (2.17)$$

where $\vec{v} = (\theta_v, \phi_v)$ is the view direction, $\vec{l} = (\theta_l, \phi_l)$ is the direction to a light source or a sampling direction, S is the area of the hemisphere H subtended by the light sources, R is the remaining area, and $d\Omega_l = \cos \theta_l \sin \theta_l d\theta_l d\phi_l$ is the projected surface element (compare [Dür06]). In the current version of RADIANCE the direct specular component is approximated by

$$\int_S L_l(\vec{l}) f_{\text{WD}}(\vec{l}, \vec{v}) d\Omega_l \approx \sum_{m=1}^M L_l(\vec{l}_{(m)}) f_{\text{WD}}(\vec{l}_{(m)}, \vec{v}) \Delta\Omega_{l_{(m)}}, \quad (2.18)$$

where $\vec{l}_{(m)}$ are the directions to the light sources in the scene. The corresponding functions are *diraniso()* in *aniso.c* for anisotropic reflection and *dirnorm()* in *normal.c* for isotropic reflection, respectively (see [Rad10]).

2.2 A New BRDF Model Based on the Ward-Dür BRDF

The second term in Equation (2.17) describes the indirect specular component and is approximated in RADIANCE by

$$\int_R L_l(\vec{l}) f_{\text{WD}}(\vec{l}, \vec{v}) d\Omega_l \approx \rho_s \cdot L_l(\vec{l}^*), \quad (2.19)$$

where the direction \vec{l}^* is chosen randomly by *Ward's sampling method* [War92, WS98] described below in Equation (2.21). Because $\theta_l^* > \pi/2$ is possible, samples $\vec{l}^* \notin R$ are rejected until a valid direction is generated. The corresponding functions are *agaussamp()* in *aniso.c* for anisotropic reflection and *gaussamp()* in *normal.c* for isotropic reflection, respectively (see [Rad10]). Within the *iBRDF* extension to RADIANCE, Westlund et al. [WMW99, Wes00] improved the approximation of the indirect specular component to

$$\int_R L_l(\vec{l}) f(\vec{l}, \vec{v}) d\Omega_l \approx \frac{\rho_s}{N} \sum_{n=1}^N L_l(\vec{l}_{(n)}^x), \quad (2.20)$$

where the directions $\vec{l}_{(n)}^x$ are chosen according to a tabulated BRDF f .

In the backward ray tracing process, for a given reflected direction $\vec{v} = (\theta_v, \phi_v)$ the incident direction $\vec{l} = (\theta_l, \phi_l)$ is determined via the halfway vector \vec{h} that is given by its angles

$$\delta = \arctan \left(\sqrt{\frac{-\log(1-s)}{\cos^2 \phi / \alpha^2 + \sin^2 \phi / \beta^2}} \right) \quad \text{and} \quad \phi = \arctan \left(\frac{\beta}{\alpha} \tan(2\pi t) \right), \quad (2.21)$$

where s and t are independent random numbers uniformly distributed in $[0, 1)$. Note that the calculation of ϕ should be implemented as $\phi = \text{atan2}(\beta \sin(2\pi t), \alpha \cos(2\pi t))$ to allow $\phi \in (-\pi, \pi]$. In [War92] the arctan in the formula for δ is missing what was noted by Dür [Dür06] and Walter [Wal05], but the calculation of the halfway vector is correctly implemented in the source code of RADIANCE. Dür shows that the distribution of the random direction \vec{l} has the probability density function (PDF)

$$d_{\alpha, \beta}(\theta_l, \phi_l; \theta_v, \phi_v) = \frac{f_{\text{WD}}(\theta_l, \phi_l; \theta_v, \phi_v)}{\rho_s \cdot w(\theta_l, \phi_l; \theta_v, \phi_v)}, \quad (2.22)$$

with

$$w(\theta_l, \phi_l; \theta_v, \phi_v) = \frac{(\cos \theta_l + \cos \theta_v)^3}{4 \cos \theta_v (1 + \cos \theta_l \cos \theta_v + \sin \theta_l \sin \theta_v \cos(\phi_v - \phi_l))}. \quad (2.23)$$

Because at non-grazing angles and for small values of α and β

$$d_{\alpha, \beta}(\theta_l, \phi_l; \theta_v, \phi_v) \approx f_{\text{WD}}(\theta_l, \phi_l; \theta_v, \phi_v) / \rho_s, \quad (2.24)$$

no weighting factors are used in the Monte Carlo integration (Equation (2.19)) in RADIANCE (see *normal.c* and *aniso.c* in the source code [Rad10]). However, at grazing angles the difference between the BRDF f_{WD} and the sampling PDF $d_{\alpha, \beta}$ is significant and can clearly be observed (see Figure 2.8).

2 Improvements in the Accuracy of Computational Methods in RADIANCE

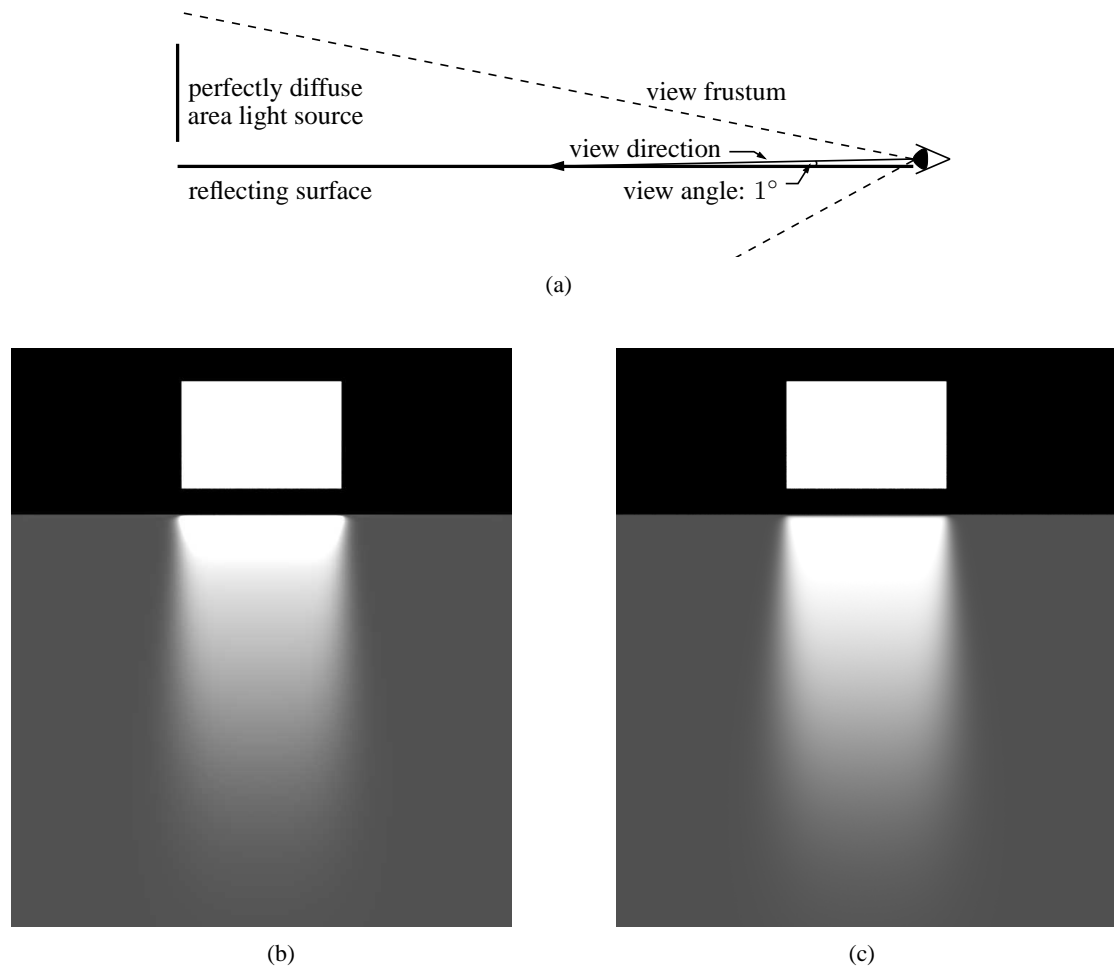


Figure 2.8: Grazing angle test scene: (a) set-up and renderings with specular reflection calculated by (b) Ward-Dür BRDF and (c) Ward's sampling method.

Figure 2.8(a) shows the set-up of a test scene where a gray isotropic surface with 80% specular reflection ($\rho_d = 0.12$, $\rho_s = 0.48$) and roughness of $\alpha = 0.1$ is viewed at a grazing angle of 1° . Using RADIANCE's *light* material for the luminaire the direct illumination is computed by evaluating the Ward-Dür BRDF. The resulting image is shown in Figure 2.8(b). To avoid inaccuracies within the subdivision algorithm for flat area light sources (compare Section 2.1.1), the maximum number of source subdivisions was set to 512 in *source.h*. Figure 2.8(c) shows the result if the direct illumination is calculated using Ward's sampling method, i.e. following the sampling PDF. Therefore the light source needs to be included in the calculation of the indirect specular component in RADIANCE which can be done by modeling the luminaire with the *glow* material. By default a single sample ray that is determined by rejection sampling is sent in RADIANCE in the indirect specular component calculation (see Equation (2.19)). To receive a

smooth image that is comparable to the BRDF result we changed Equation (2.19) similar to the approach by Westlund (see Equation (2.20)) to

$$\int_R L_l(\vec{l}) f_{\text{WD}}(\vec{l}, \vec{v}) d\Omega_l \approx \frac{\rho_s}{N} \sum_{n=1}^N L_l(\vec{l}_{(n)}^*), \quad (2.25)$$

where the direction \vec{l}^* is chosen randomly by Ward's sampling method and N is set to 10000. In the RADIANCE source code we added a loop around the call to *gaussamp()* in the function *m_normal()* in *normal.c* and thus traced 10000 indirect specular sample rays. The differences in the reflections at the gray surface can already be observed in Figures 2.8(b) and 2.8(c), but are more clearly visualized in the falsecolor images shown in Figure 2.9 where the luminance distributions that result from the two methods are juxtaposed.

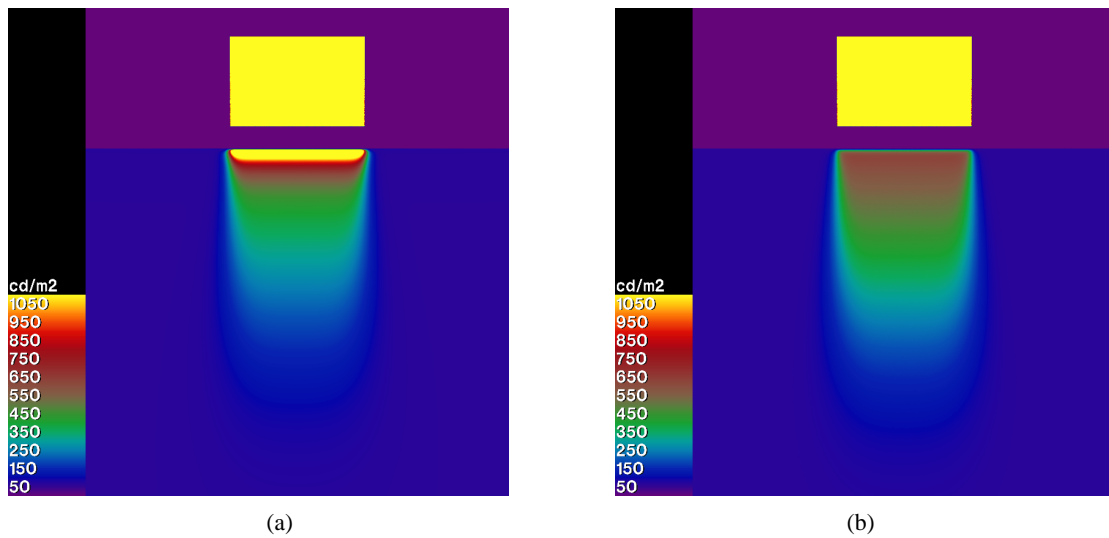


Figure 2.9: Falsecolor images showing the luminance distributions resulting from (a) Figure 2.8(b) (Ward-Dür BRDF) and (b) Figure 2.8(c) (Ward's sampling method).

In [NNSK99] Neumann et al. criticize that the Ward BRDF is not physically plausible because at grazing angles the BRDF diverges to infinity and its albedo violates energy balance, i.e. it is greater than 1. Using $\max(\cos \theta_l, \cos \theta_v)$ instead of $\sqrt{\cos \theta_l \cos \theta_v}$ in Equation (2.15), Neumann et al. propose a modification that meets energy balance but still has the shortcoming that specular highlights are too dark, especially for low-lying light sources. We refer to this modification as Ward-Neumann BRDF.

Because the Ward-Dür BRDF can be written as $f_{\text{WD}}(\vec{l}, \vec{v}) = f_{\text{W}}(\vec{l}, \vec{v}) / \sqrt{\cos \theta_l \cos \theta_v}$ the argumentation concerning energy balance as given in [NNSK99] also holds for the Ward-Dür BRDF. In Figure 2.12 the albedos of the Ward-Dür BRDF, the Ward BRDF, the Ward-Neumann BRDF, our new BRDF, and the PDF of Ward's sampling method are compared.

2.2.2 New BRDF

To remove the discrepancy between the calculation of the direct and the indirect illumination in RADIANCE, i.e. between evaluating the Ward-Dür BRDF and the sampling by Ward's method, and to account for the criticism by Neumann et al. [NNSK99], we propose the following modification of the Ward-Dür BRDF that preserves Helmholtz reciprocity:

$$f_{new}(\theta_l, \phi_l; \theta_v, \phi_v) = \frac{\rho_s}{\pi\alpha\beta} \cdot \exp\left(-\tan^2 \delta \left(\frac{\cos^2 \phi}{\alpha^2} + \frac{\sin^2 \phi}{\beta^2}\right)\right) \cdot \frac{2(1 + \cos \theta_l \cos \theta_v + \sin \theta_l \sin \theta_v \cos(\phi_v - \phi_l))}{(\cos \theta_l + \cos \theta_v)^4}. \quad (2.26)$$

In particular

$$f_{new}(\theta_l, \phi_l + \pi; \theta_l, \phi_l) = \frac{\rho_s}{4\pi\alpha\beta \cos^2 \theta_l} = f_{WD}(\theta_l, \phi_l + \pi; \theta_l, \phi_l). \quad (2.27)$$

Staying in line with the Ward BRDF we do not introduce Fresnel factors in our proposed model. In [War92], Ward states that geometric attenuation coefficients and the Fresnel factor usually counteract anyway. However, if Fresnel effects are explicitly desired, either Schlick's approximation [Sch94]

$$\rho' = \rho + (1 - \rho)(1 - \cos \theta_l)^5 \quad (2.28)$$

or Ward's approximation that is used in RADIANCE [Rad10] for purely specular surfaces, i.e. materials with zero roughness,

$$\rho' = \rho + (1 - \rho)(\exp(-5.85 \cdot \cos \theta_l) - 0.00287989916) \quad (2.29)$$

can be used.

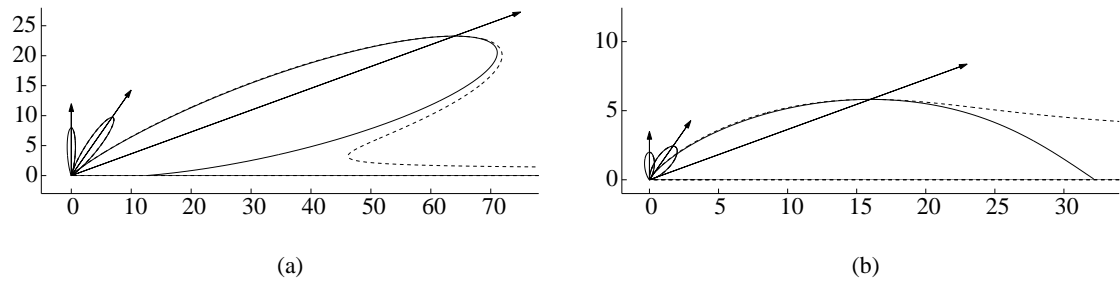


Figure 2.10: New BRDF (solid lines) and Ward-Dür BRDF (dashed lines) at $\theta_l = 0^\circ, 35^\circ,$ and 70° for $\rho_s = 1$ and (a) $\alpha = \beta = 0.1$ and (b) $\alpha = \beta = 0.2$.

The polar plots in Figures 2.10 and 2.11 compare the isotropic BRDFs of our new model and the Ward-Dür model for $\rho_s = 1$ and $\alpha = \beta = 0.1$ or $\alpha = \beta = 0.2$ in the plane of incidence.

2.2 A New BRDF Model Based on the Ward-Dür BRDF

The images in Figure 2.10 present the absolute values of the BRDFs for $\theta_l = 0^\circ, 35^\circ,$ and 70° , whereas the images in Figure 2.11 show the particular reflected radiances for $\theta_l = 0^\circ, 45^\circ,$ and 85° , multiplied by $\cos \theta_v$. From Figures 2.10 and 2.11 one can see that the new BRDF mainly coincides with the Ward-Dür BRDF but is physically valid at grazing angles.

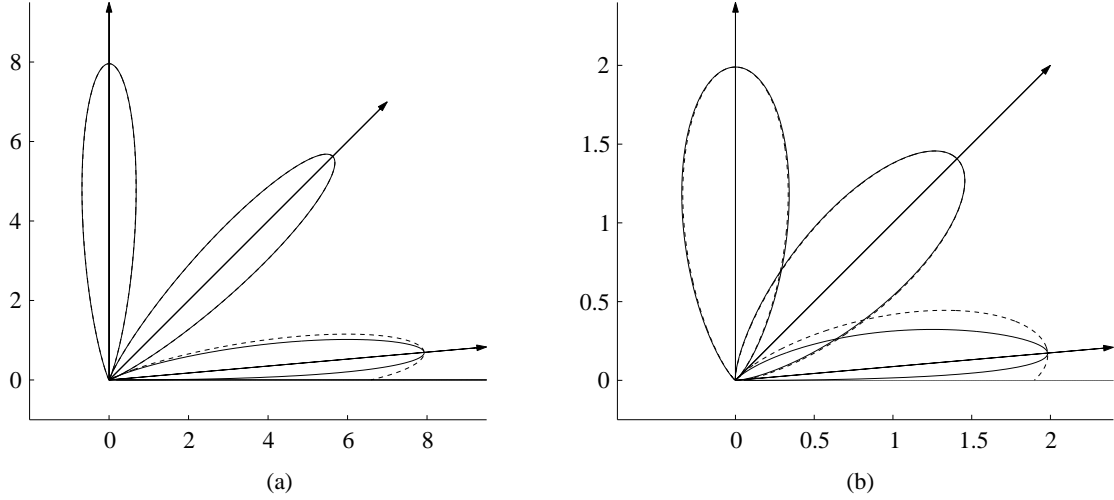


Figure 2.11: Reflected radiance multiplied by $\cos \theta_v$ for new BRDF (solid lines) and Ward-Dür BRDF (dashed lines) at $\theta_l = 0^\circ, 45^\circ,$ and 85° for $\rho_s = 1$ and (a) $\alpha = \beta = 0.1$ and (b) $\alpha = \beta = 0.2$.

Figures 2.10 and 2.11 predict that, in the plane of incidence, the maximum of the new BRDF $f_{new}(\vec{l}, \vec{v})$ occurs below the mirror direction, whereas the maximum of the new BRDF times the cosine of the polar angle of the reflected direction $f_{new}(\vec{l}, \vec{v}) \cdot \cos \theta_v$ is found in the mirror direction (the corresponding proofs are given in Appendix B). Thus, the new BRDF shows the same behaviour as the Ward-Dür BRDF concerning off-specular peaks that were first described by Torrance and Sparrow [TS67].

Contrary to the Ward-Dür BRDF our new BRDF model is physically plausible as it meets energy balance, i.e. the albedo is bounded by 1 (in Appendix B the proof is given for the critical case where $\theta_l \rightarrow \pi/2$):

$$\forall \theta_l \in [0, \pi/2] : a(\theta_l, \phi_l) = \int_0^{2\pi} \int_0^{\pi/2} f_{new}(\vec{l}, \vec{v}) \cos \theta_v \sin \theta_v d\theta_v d\phi_v \leq 1. \quad (2.30)$$

In Figure 2.12(a) the albedo functions of the Ward BRDF, the Ward-Dür BRDF, the PDF of Ward's sampling method, the Ward-Neumann BRDF, and our new BRDF are compared in the isotropic case for $\alpha = \beta = 0.1$ and $\rho_s = 1$. Note that the albedo of the sampling method is calculated as $a(\vec{v})$ because in backward ray tracing \vec{v} is the incident direction and \vec{l} is the sampled direction. Figure 2.12(b) shows the behaviour of the albedo functions of the Ward BRDF, the Ward-Dür BRDF, and our new BRDF at grazing angles. In Figure 2.13 the albedo functions of

2 Improvements in the Accuracy of Computational Methods in RADIANCE

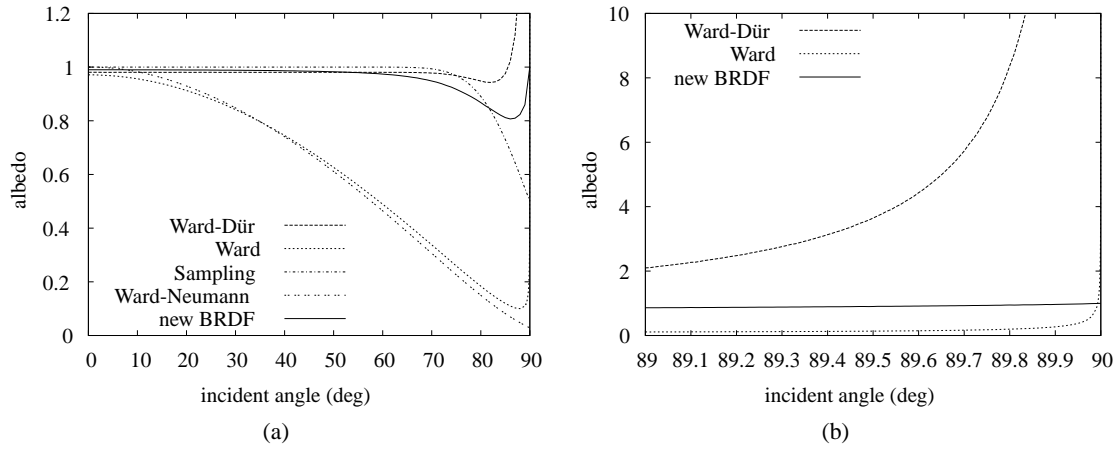


Figure 2.12: Albedo functions (a) for various BRDF models and (b) at grazing angles for the Ward BRDF, the Ward-Dür BRDF, and our new BRDF.

our new BRDF in the isotropic cases for $\alpha = \beta = 0.01$, $\alpha = \beta = 0.05$, $\alpha = \beta = 0.1$, and $\alpha = \beta = 0.2$ are presented. Again we examine the purely specular case $\rho_s = 1$.

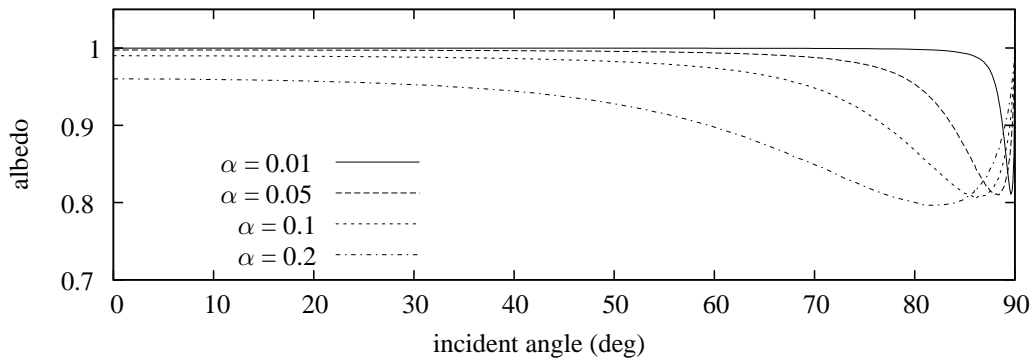


Figure 2.13: Albedo functions of our new BRDF for varying values of $\alpha = \beta$.

Writing the PDF $d_{\alpha,\beta}$ of Ward's sampling method (see Equation (2.22)) with respect to our new BRDF yields

$$d_{\alpha,\beta}(\theta_l, \phi_l; \theta_v, \phi_v) = \frac{f_{new}(\theta_l, \phi_l; \theta_v, \phi_v)}{\rho_s \cdot w_{new}(\theta_l, \phi_l; \theta_v, \phi_v)}, \quad (2.31)$$

where

$$w_{new}(\theta_l, \phi_l; \theta_v, \phi_v) = \frac{2}{1 + \cos \theta_v / \cos \theta_l} = \frac{2}{1 + \langle \vec{v}, \vec{n} \rangle / \langle \vec{l}, \vec{n} \rangle}. \quad (2.32)$$

With our new BRDF, the indirect specular component can be approximated by

$$\int_R L_l(\vec{l}) f_{new}(\vec{l}, \vec{v}) d\Omega_l \approx \frac{\rho_s}{N} \sum_{n=1}^N L_l(\vec{l}_{(n)}^*) w_{new}(\vec{l}_{(n)}^*, \vec{v}), \quad (2.33)$$

where the weighting factors w_{new} are cheap to compute by Equation (2.32). Finally, rewriting the new BRDF as

$$f_{new}(\theta_l, \phi_l; \theta_v, \phi_v) = \frac{\rho_s}{\pi\alpha\beta} \cdot \exp\left(-\frac{1}{\langle \vec{l} + \vec{v}, \vec{n} \rangle^2} \cdot \left(\frac{\langle \vec{l} + \vec{v}, \vec{x} \rangle^2}{\alpha^2} + \frac{\langle \vec{l} + \vec{v}, \vec{y} \rangle^2}{\beta^2}\right)\right) \cdot \frac{\langle \vec{l} + \vec{v}, \vec{l} + \vec{v} \rangle}{\langle \vec{l} + \vec{v}, \vec{n} \rangle^4} \quad (2.34)$$

shows that the BRDF for the direct specular component

$$\int_S L_l(\vec{l}) f_{new}(\vec{l}, \vec{v}) d\Omega_l \approx \sum_{m=1}^M L_l(\vec{l}_{(m)}) f_{new}(\vec{l}_{(m)}, \vec{v}) \Delta\Omega_{l_{(m)}}, \quad (2.35)$$

is computationally cheap and thus sustains one of the main benefits of the Ward model.

Grazing Angle Test Scene

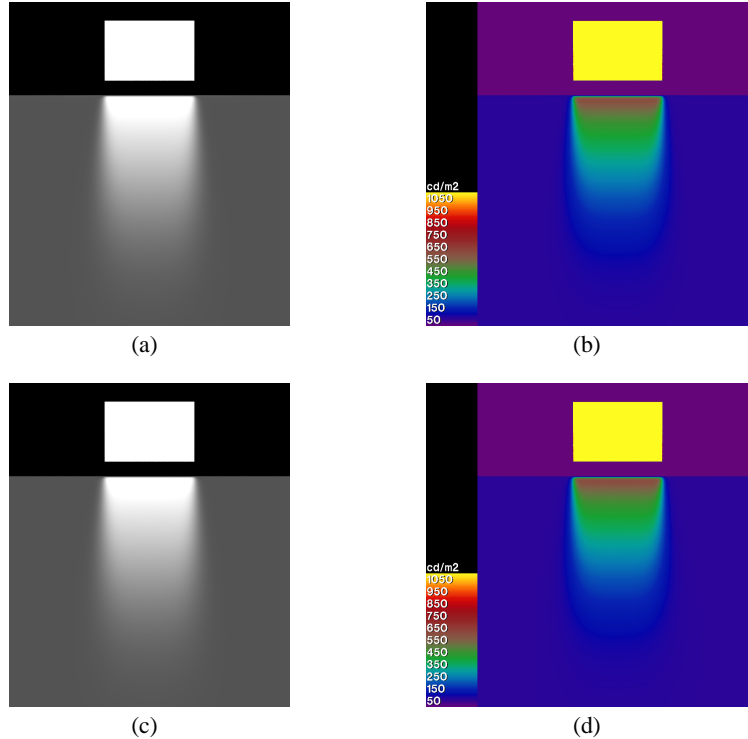


Figure 2.14: Grazing Angle Test Scene: (a) rendering with specular reflection calculated by new BRDF, (b) resulting luminance distribution, (c) rendering with specular reflection calculated by Ward's sampling method using new weighting factors, and (d) resulting luminance distribution.

2 Improvements in the Accuracy of Computational Methods in RADIANCE

We re-rendered the test scene of Section 2.2.1 (see Figure 2.8(a) for the set-up) using Equation (2.35) for calculating the direct specular component from the luminaire modeled as *light* (Figure 2.14(a)) and using Equation (2.33) for computing the indirect specular component from the luminaire modeled as a *glow* material (Figure 2.14(c)). In the falsecolor images (Figures 2.14(b) and 2.14(d)) no differences can be observed. By using luminance contour lines laid over the images (Figure 2.15) it is clearly visualized that the resulting distributions are the same for the new BRDF and the sampling using the new weighting factors. Including the new BRDF and weighting factors in the current version of RADIANCE [Rad10] does not change the rendering times significantly.

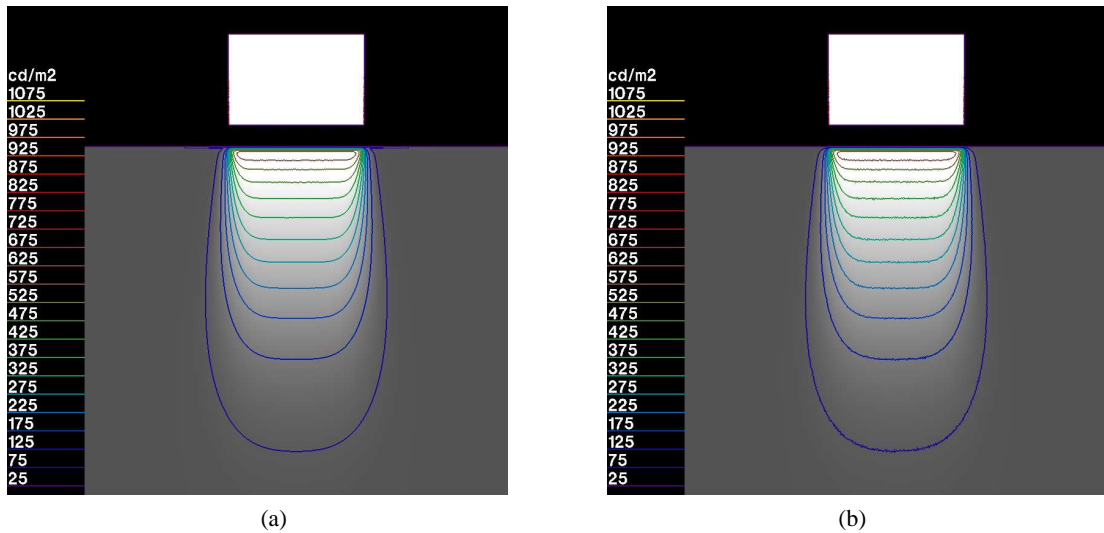


Figure 2.15: Luminance distributions laid over renderings for the Grazing Angle Test Scene: specular reflection calculated (a) by new BRDF and (b) by Ward's sampling method using new weighting factors.

2.2.3 Fitting the New BRDF

The BRDF of an isotropic red linoleum floor was measured with a gonioreflectometer for 222 pairs of incident/outgoing directions by our cooperation partner Bartenbach LichtLabor, Austria [Bar]. In Appendix B the corresponding data are given. The total reflectance ρ of the isotropic linoleum floor illuminated by the CIE standard illuminant A [CIE04] is 17.5% and was measured by Bartenbach LichtLabor using an integrating sphere.

For the curve fitting we use the same approach as Ngan et al. [NDM05], i.e. we define the objective function for fitting as

$$g(\theta_l, \phi_l; \theta_v, \phi_v) = \left(d(\theta_l, \phi_l; \theta_v, \phi_v) - \left(\frac{\rho_d}{\pi} + f(\theta_l, \phi_l; \theta_v, \phi_v) \right) \right) \cdot \cos \theta_l, \quad (2.36)$$

where $\rho_d = \rho - \rho_s$ is the diffuse reflectance, $f = f_W$ for the Ward BRDF, f_{WD} for the Ward-Dür BRDF, or f_{new} for our new BRDF, respectively. The parameter estimation is then performed

2.2 A New BRDF Model Based on the Ward-Dür BRDF

using the MATLAB routine *lsqnonlin()* that computes ρ_s and α such that

$$\|g(\theta_l, \phi_l; \theta_v, \phi_v)\|_2^2 = \sum_{k=1}^{222} g(\theta_l^{(k)}, \phi_l^{(k)}; \theta_v^{(k)}, \phi_v^{(k)})^2 \rightarrow \min. \quad (2.37)$$

	Parameter		Error
	ρ_s	α	r
Ward BRDF f_W	0.08508	0.02935	6.8269
Ward-Dür BRDF f_{WD}	0.02605	0.02122	2.8846
new BRDF f_{new}	0.04982	0.03172	0.9241

Table 2.3: Fitting results for the isotropic red linoleum floor (see Appendix B).

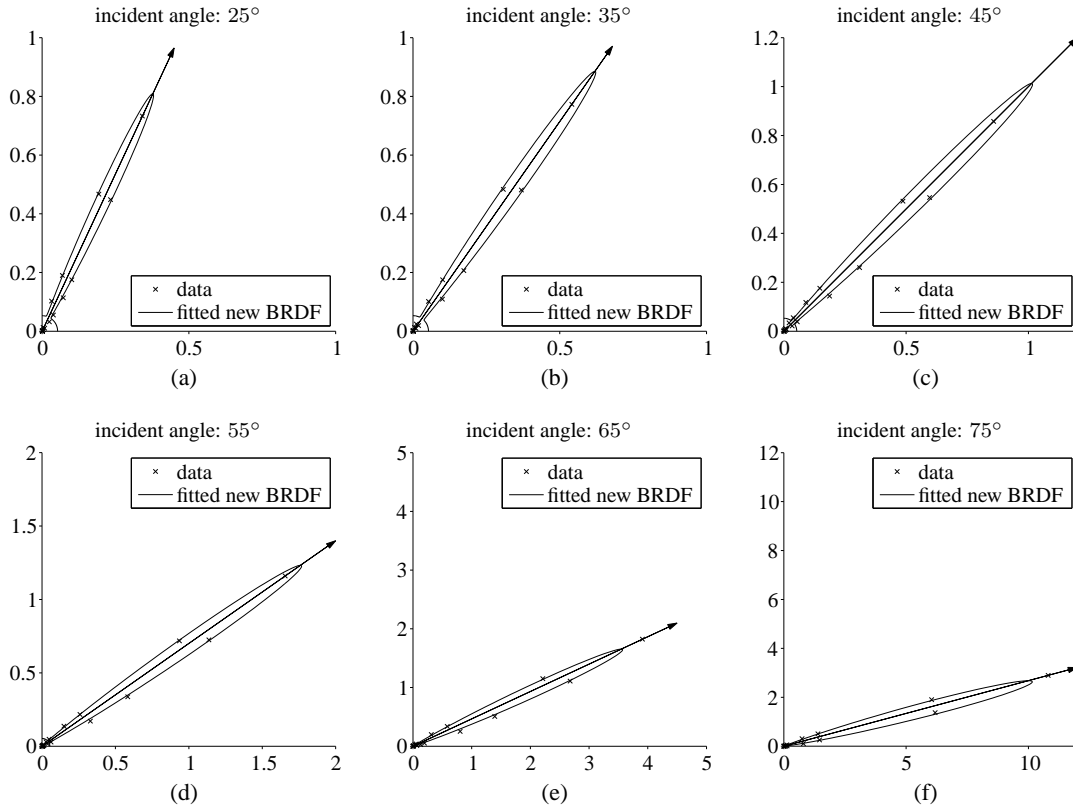


Figure 2.16: Measured BRDF data for the isotropic red linoleum floor and fits from the new BRDF model for incident angles from 25° to 75°. Note the varying scales.

In Table 2.3 the results for ρ_s and α of the three BRDF models are presented together with the residual error r that specifies the computed minimum value in Equation (2.37). Expectedly,

2 Improvements in the Accuracy of Computational Methods in RADIANCE

compared to the Ward-Dür BRDF we receive a higher value for the roughness α that accounts for the tighter lobes of the new BRDF at grazing angles (see Figure 2.11). In turn also the specular ρ_s increases and thus corrects the length of the lobe that is shortened by the greater α . The decrease of the residual error by a factor of 3 demonstrates that – given the measured BRDF of the isotropic red linoleum floor – the new BRDF is better suited to approximate the measured data. Figures 2.16(a) to 2.16(f) show the measured BRDF data together with the fits obtained from the new BRDF for incidence angles from 25° to 75° every 10° .

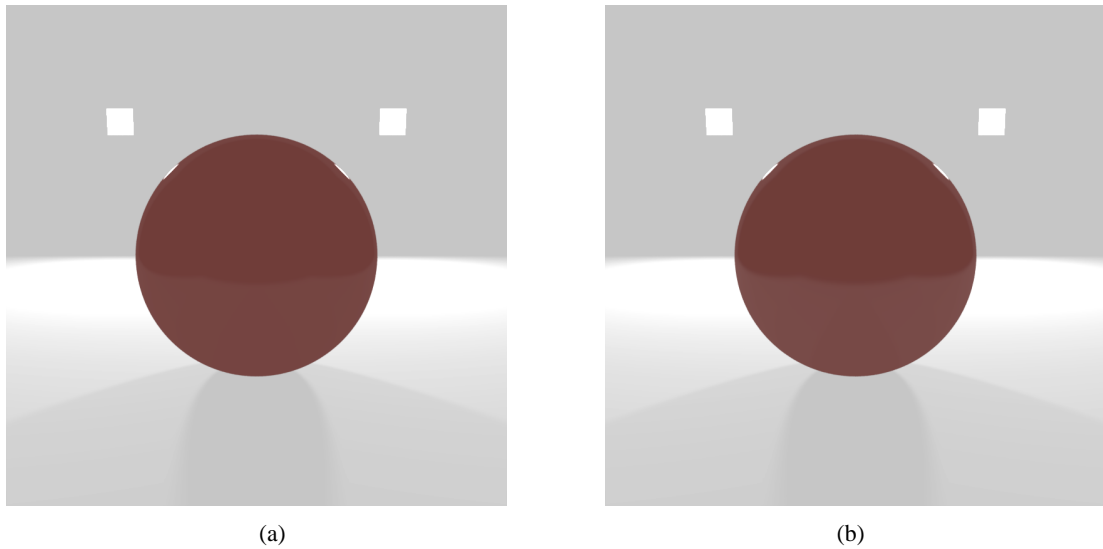


Figure 2.17: Test scene containing an isotropic red linoleum sphere. The specular highlights are calculated (a) by the Ward-Dür BRDF and (b) by the proposed new BRDF.

Figure 2.17 shows a test scene for comparing the Ward-Dür BRDF f_{WD} to the new BRDF f_{new} . The scene contains an isotropic red linoleum sphere that is modeled in RADIANCE using the *plastic* material with the particular parameters from Table 2.3. Because the differences between the highlights in Figures 2.17(a) and 2.17(b) are hardly visible, a close-up of the right highlight was rendered. Figure 2.18 shows the results obtained from using the Ward-Dür BRDF (2.18(a)) and the new BRDF (2.18(b)). The falsecolor image below (Figure 2.18(c)) gives the relative brightness differences between the two images with Figure 2.18(a) (Ward-Dür BRDF) being the reference. Here the maximal differences are located on a circular ring around the center of the highlight.

Compared to the Ward-Dür BRDF our new BRDF yields significantly more expanded specular highlights and thus up to five times brighter reflections in off-center regions. Regarding the criticism by Ngan et al. [NDM05] that at grazing angles the Ward-Dür BRDF produces much less pronounced highlights than the measured data, the behaviour of the new BRDF seems to be desirable.

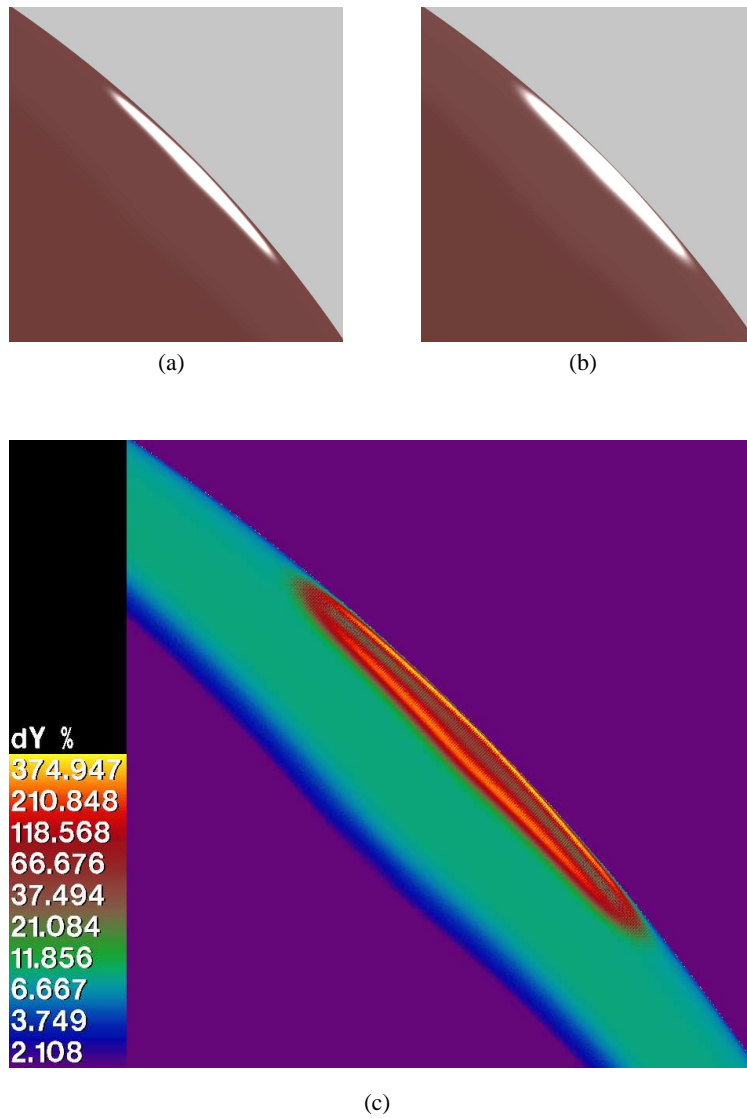


Figure 2.18: Close-up of the right highlights in Figure 2.17: renderings with specular highlights calculated (a) by the Ward-Dür BRDF and (b) by the new BRDF, and (c) relative brightness differences with Ward-Dür BRDF being the reference.

2.2.4 Conclusion

We presented an improved BRDF model based on the Ward-Dür BRDF [Dür06]. The new model is physically plausible, i.e., it satisfies Helmholtz reciprocity and meets energy balance. For non-flat angles the new BRDF is very close to the Ward-Dür BRDF due to the identical exponential functions. Ward’s sampling method gives an efficient importance sampling formula

2 Improvements in the Accuracy of Computational Methods in RADIANCE

and the evaluation of both the weighting factors for the Monte Carlo integration and the proposed BRDF model are computationally cheap. In the rendered test scenes the computation times did not significantly change when using the new BRDF and weighting factors for the Monte Carlo integration.

The new model also improves the ability to approximate a measured BRDF. For the red linoleum floor the fitting residual decreased by a factor of 3 compared to the Ward-Dür BRDF. Additionally, the higher parameters that were obtained from the fitting yield more expanded specular highlights and thus up to five times brighter reflections in off-center regions.

3 Color Rendering Indices in Global Illumination Methods

Die Farbe ist der Ort, wo unser Gehirn und das Weltall sich begegnen.

(Paul Cézanne, 1839-1906)

Abstract. Human perception of material colors depends heavily on the nature of the light sources that are used for illumination. One and the same object can cause highly different color impressions when lit by a vapor lamp or by daylight, respectively. On the basis of state-of-the-art colorimetric methods, we present a modern approach for the calculation of color-rendering indices (CRI), which were defined by the International Commission on Illumination (CIE) to characterize color reproduction properties of illuminants. We update the standard CIE method in three main points: first, we use the CIELAB color space; second, we apply a linearized Bradford transformation for chromatic adaptation; and finally, we evaluate color differences using the CIEDE2000 total color difference formula. Moreover, within a real-world scene, light incident on a measurement surface is composed of a direct and an indirect part. Neumann and Schanda [Proc. CGIV'06 Conf., Leeds, UK, pp. 283–286 (2006)] have shown for the cube model that diffuse interreflections can influence the CRI of a light source. We analyze how colorrendering indices vary in a real-world scene with mixed direct and indirect illumination and recommend the usage of a spectral rendering engine instead of an RGB-based renderer for reasons of accuracy of CRI calculations.

3.1 Background

Industrial standards for illumination define the basic conditions for lighting design. E.g. at workplaces specified lighting conditions are required, where standards for characteristics such as illuminance, color temperature or color-rendering indices (CRI) have to be met. In this paper, we focus on the topic of color rendering indices in two respects. First, in a theoretical context regarding the calculation method, and second, in a practical context in terms of applicability of CRI calculations in scenes with global illumination.

The standard International Commission on Illumination (CIE) method for calculating the color-rendering index R_a , which was approved in 1974, is based on the CIEU*V*W* color space with the Euclidian distance as the corresponding color difference formula and the Von Kries transformation for chromatic adaptation. Since then, different approximately uniform color

spaces, better color difference formulas, and improved chromatic adaptation transformations have been developed. In Section 3.2, we cite several authors who point out various weaknesses of the CIE method (e.g., for white LED sources [BCSS04]) or propose different approaches for the characterization of light sources. Moreover, we overview various attempts toward spectral rendering from current literature, which range from spectral representations using linear combinations of orthonormal basis functions to N-step algorithms implementing several three-channel calculations in an RGB-based rendering engine.

In Section 3.3, we briefly describe the procedures of the standard CIE method and the CIE recommendation $R96_a$, which was published in 1999 [CIE99]. We present the color-rendering index CRI_{00} as a revised approach for the calculation of CRIs, where we use state-of-the-art colorimetric methods, but procedurewise still proceed in line with the CIE method. The three main improvements of our method affect the underlying color space, where we use CIELAB instead of $CIEU^*V^*W^*$, which is also recommended for $R96_a$, the chromatic adaptation transformation, where we apply a linearized Bradford transformation instead of the Von Kries adjustment, and the color difference formula, where we evaluate color differences using the CIEDE2000 color difference formula instead of the Euclidian norm. To enable comparisons to both the standard CIE method and the 1999 CIE proposal, we use both sets of color test samples – 14 Munsell colors as for R_a calculations and eight Macbeth ColorChecker samples plus two skin tones as recommended for $R96_a$. We present results of our improved calculation method for seven customary light sources (fluorescent, power ball, or mercury vapor lamps) and three LED light sources.

As shown by Neumann and Schanda [NS06], diffuse interreflections in a room can influence the perceived color-rendering properties. We analyze the variation of the CRI within real-world scenes with mixed direct and indirect illumination. To make CRI calculations possible within a lighting simulation program, we set up a spectral version of the physically based renderer RADIANCE [War94, WS98] which is presented in Section 3.4. Our approach is based on discrete spectra using 81 values between 380 and 780 nm equally spaced at every 5 nm. We compare our spectral results to naive RGB renderings and an improved RGB method, which uses spectral prefiltering [WEV02], and obtain differences in relative brightness of $\sim 10\%$, CIEDE2000 color differences of ~ 8 , and CRI differences of ~ 4 . As an example of use, we show both the distribution of the CRI and the correlated color temperature (CCT) in a real-world seminar room calculated from a rendered image.

A preliminary version of this paper was presented at the Human Vision and Electronic Imaging XIV Conference 2009 [GMD09a]. Because of a bug in the Little CMS Version 1.15 [Mar09], some numerical results in the proceedings are imprecise.

3.2 Related Work

Since CRIs have been introduced in 1974 by the CIE, many authors criticized this method in various points and presented different approaches for the development of a new method. In the sequel, we survey these proposals. The main interests for most investigations are the number and/or the characteristic of the test samples and the used color space with the related color difference formula. Guo and Houser [GH04] reevaluate the color rendering indices proposed

by Judd [Jud62], Thornton [Tho74, Tho72], Fotios [Fot97], Xu [Xu93], and Pointer [Poi86]. Seim [Sei85] proposes a method that uses the Seim-Valberg color space formula [SV86] together with 20 color samples of constant lightness and saturation, and with hues evenly distributed along the color circle. Pointer [Poi86] defines an alternative index based on separate hue, chroma, and lightness indices, and uses the 18 color samples from the Macbeth ColorChecker [MMD76] chart. Another color-rendering index, which is independent of test color samples, is proposed by Xu [Xu95]. In 1999, the CIE proposed the color-rendering index $R96_a$ in the closing remarks of the Technical Committee CIE TC 1-33 [CIE99]. The committee agreed to use eight colors from the Macbeth ColorChecker and two skin tones as test samples and to perform all calculations in the CIELAB color space. However, because of various disagreements, such as the choice of reference illuminants or the correlation between color differences and CRI, no final recommendation was given [Sch97]. Similar to our approach, Davis and Ohno [DO05] present an updated CRI based on the standard CIE method, where they replace the original samples by 15 highly saturated Munsell colors, use the CIELAB color space, introduce a CCT factor to account for changes in correlated color temperature, and calculate the CRI as root mean square. Schanda [Sch02], Bodrogi [Bod04], and Sándor and Schanda [SS06] propose to use color appearance models (CAMs) like CIECAM97s or CIECAM02 in the calculation of CRIs, because color difference formulas based on such CAMs were shown to be suitable for both small and large color differences by Li et al. [LLC03].

Recently, two approaches that are even further away from the classical CIE method were presented. Szabo et al. [SZBS07, SBS09] define a new color harmony formula together with an associated harmony-rendering index. On the basis of a survey with LED clusters, Vienot et al. [VEBM07] recommend the development of color quality grades or light quality indices. The failure of the CIE method for white LED light sources was also pointed out by Bodrogi et al. [BCSS04], Schanda [Sch07], and the CIE [CIE07]. Here, the main point of criticism is that the three peaks in the spectral power distribution of a white LED of the RGB cluster type combined with narrowband colorants can cause a wide range of perceived color differences, which are not predictable by a single average number, such as the CRI.

Not solely considering the light source, Neumann and Schanda [NS06] analyze the effect of diffuse interreflections on the CRI in a cube model. They show how the correlated color temperature and the CRI vary for different pairs of light sources and lambertian wall paint colors. On the basis of given examples for all three possible cases (i.e., that the CRI of a light source increases, decreases, or stays unchanged for different paint colors), they motivate to properly select both light sources and wall paint colors when a high CRI is desired.

Devlin et al. [DCWP02] describe that rendering techniques based on three-dimensional color spaces, such as RGB or XYZ, are not appropriate to be used for predictive purposes. Similarly, Ruppertsberg and Bloj [RB06] state that renderings in RGB space are not accurate enough for psychophysical experiments where real physical properties have to be simulated. In fact, color computations have to be performed in spectral space and – concerning color rendering – it is only possible to calculate CRIs from spectral power distributions (SPDs). During the past 20 years, various approaches for spectral rendering were published. For example, Meyer [Mey88] presents a method that uses Gaussian quadrature with the opponent representation of the fundamental spectral sensitivity functions for wavelength selection. Another approach is given by Peercy [Pee93], where SPDs are represented by vectors defining the coefficients for linear

combinations of orthonormal basis functions. Bergner et al. [BMD04] propose a method that also uses a principle component representation, but they derive the optimal basis functions from products of lights and reflectances. Our approach for a spectral rendering engine based on RADIANCE is similar to the setup by Johnson and Fairchild [JF99] with the difference that they use spectral rendering only in a local illumination context, where interreflections are not considered. Both Delahunt and Brainard [DB04] and Ruppertsberg and Bloj [RB08] perform spectral rendering with RADIANCE by combining multiple calls of the standard RGB version with pre- and postprocessing. They implement monochromatic renderings for each wavelength or process spectral information from three wavelengths using the three channels in one RGB rendering, respectively, resulting in an enormous computational overhead. Moreover, these approaches are problematic because several algorithms in RADIANCE are steered by its functions intensity and brightness. The intensity function is defined as the maximum of the three values R, G, and B, whereas the brightness is a weighted sum of the RGB values to approximate the CIE-Y tristimulus and thus not valid for arbitrary wavelengths. In scenes with many light sources, a list of illuminants is set up based on the brightness function using the “selective shadow testing” algorithm to approximate the direct illumination from all light sources by a rather small number of sources. This list can now contain different light sources for different wavelengths and thus result in spectrally varying illumination. RADIANCE also uses the intensity function to evaluate the weight of a ray and stops tracing the ray if its weight falls below a given threshold. Hence, rays generated by RADIANCE might be stopped earlier for some parts of the spectrum than for others resulting in truncated SPDs.

An improvement to RGB rendering by using spectral prefiltering is presented by Ward and Eydalberg-Vileshin [WEV02]. In their method, the RGB values for the surface reflectances are calculated from their spectral representations such that the direct-diffuse component is exact when illuminated by the light source. Compared to full-spectral rendering, the main drawback of this method is that scenes lit by different light sources or with specular and/or multiple reflections are not rendered accurately. However, because this improved RGB method is superior to naive RGB models, we will use it for additional comparisons to our full-spectral solutions.

3.3 CRI

In 1974, the CIE defined CRIs in order to categorize light sources. These indices describe the capability of an illuminant to reproduce colors of different objects compared to a reference illuminant and thus measure how humans perceive colors under a particular light source.

3.3.1 Standard CIE Method for Calculating CRIs

CRIs for a test light source are calculated using 14 Munsell colors as test samples. These test samples are illuminated with the test light and with a reference light, which has the same CCT, to obtain the CIEXYZ tristimulus values. The CCT is calculated as closest Planckian radiator in the CIE 1960 (u, v) diagram. Both test and reference XYZ values are mapped to the CIE 1960 (u, v) diagram, where a Von Kries type of adjustment for chromatic adaptation is performed. Finally, the (u, v) -coordinates are transformed into the CIEU*V*W* color space, where the CIE

1964 color differences ΔE_i are calculated. For each of the 14 test samples, the special color-rendering index is computed as $R_i = 100 - 4.6 \cdot \Delta E_i$. The General Color Rendering Index R_a is defined as arithmetic mean of the first 8 R_i 's, where the constant 4.6 was chosen such that the R_a for the CIE standard fluorescent lamp FL3.1 [CIE04] is 51 (see [SS03]). Detailed information and all formulas necessary for the calculation of the standard CIE CRI can be found, e.g., in [CIE95] and [Hun95]. In Tables 3.1 and 3.2, we oppose results for this standard CIE method to those from the recent CIE recommendation and our proposed method.

3.3.2 The Recent Proposal of the CIE – $R96_a$

In 1999, the CIE published the closing remarks of the Technical Committee CIE TC 1-33 on color rendering [CIE99], where proposals for updates of the CRI calculation method were given. Though the committee could not agree on a definite recommendation, a consensus was found in the following points.

First, the 14 Munsell color test samples are replaced by eight samples from the Macbeth ColorChecker [MMD76] and two skin tones – Caucasian and Oriental. Second, the chromatic adaptation transformation as introduced by the CIE [CIE94] in 1994 is used instead of the Von Kries type of adjustment, and finally, the color differences are evaluated in the CIELAB color space using the Euclidian distance (i.e., the ΔE_{ab}^* color difference). The special color rendering indices R_i are then calculated as in the standard CIE method as $R_i = 100 - c \cdot \Delta E_i$, and the general color rendering index $R96_a$ is given as an arithmetic mean of all ten special CRIs. The committee could not agree on whether to determine the constant c such that the warm white fluorescent lamp again has an $R96_a$ value of 51, or such that the average general CRI of 107 lamp spectra supplied by national committees or manufacturers remains constant. We decided to choose the latter case as only for this approach values for c are given in the closing remarks [CIE99].

Concerning the reference illuminant, no consensus for a new method could be obtained in the committee. There were two main suggestions: firstly, to use a list of six reference light sources (D65, D50, and four blackbody lamps P4200, P3450, P2950, and P2700) and to select the one closest to the test illuminant in the CIELAB space; secondly, to define the reference illuminant based on the CCT similar to the standard method, but to perform the calculations in the CIELAB color space. These two suggestions result in CRIs denoted as $R96_a(c)$ or $R96(TCC/LAB)_a$ with values for the constant c of $c[R96_a(c)] = 3.248$ or $c[R96(TCC/LAB)_a] = 3.032$, respectively. In Tables 3.1 and 3.3, we compare results for this approach to those from the standard CIE method and our proposed CRI_{00} .

3.3.3 Alternative Method for Calculating CRIs

A main drawback of the standard CIE method for CRI calculation is that it is based on colorimetric methods that were state of the art in the early 1970s, but are now inadequate. For instance, the $CIEU^*V^*W^*$ color space, which is based on the CIE 1960 uniform color space diagram, together with the Euclidian norm as the corresponding color difference formula was defined in 1964. The Von Kries type of adjustment, which is used in the CIE method for chromatic adaptation, goes back to the early 20th century [VK05]. Therefore, our approach is to update the CIE

3 Color Rendering Indices in Global Illumination Methods

standard method in three fundamental points: the color space, the chromatic adaptation, and the color difference formula.

First, we replace the CIEU*V*W* by the CIE 1976 (L*a*b*) or CIELAB color space, which was defined by the CIE in 1976 [CIE04]. Compared to the CIEU*V*W*, this space is more nearly uniform and therefore better qualified for the prediction of perceived color differences. We prefer the CIELAB over the CIELUV color space, which is the second, approximately uniform color space that was defined by the CIE in 1976, because the color difference formula we are going to use is defined for CIELAB color values.

Second, for chromatic adaptation we apply the Bradford transformation, which is used in the CIECAM97s color appearance model. This transformation is superior to the Von Kries type of adjustment or other transformations as *XYZ* scaling [Lin09]. As the nonlinear correction in the blue is considered negligible, we use the Bradford transformation in its linearized version [FS00].

Finally, for evaluating color differences we replace the Euclidian distance by the CIEDE2000 total color difference formula. This formula corrects the nonuniformity of the CIELAB color space for small color differences under reference conditions and is recommended by the CIE [CIE04]. Sharma et al. [SWD05] give implementation details for the CIEDE2000 and point out three independent sources of mathematical discontinuities for this function. Two of these discontinuities occur for color samples with hues that are 180 deg apart in the CIELAB space and hence do not occur within CRI calculations because the CIEDE2000 is only evaluated for small color differences. The third source of discontinuity could occur due to a hue rollover for a mean hue at 0/360 deg, but because this discontinuity is extremely small ($\leq 2.9 \times 10^{-4}$), it is negligible for practical purposes.

For the CRI $R96_a$, the CIE proposes to use eight test samples from the Macbeth ColorChecker chart plus two skin tones because physical samples of the original 14 Munsell colors are not available anymore [CIE99]. However, for our purpose of calculating CRIs, the spectral reflection data of the Munsell samples are sufficient and these are available in [CIE95]. Because we want to compare not only the averaged CRI_{00} but also the special rendering indices CRI_{00}^i to both the standard and the updated CIE method, we use both sets of test colors. The results in Table 3.1 show that the choice of test samples does not heavily influence the general CRI_{00} because of averaging.

Procedure

The procedure of our improved method is in line with both the standard CIE method and the CIE recommendation $R96_a(c)$. At this point, we refrain from reproducing standard colorimetric formulas, such as color space transformations, that can be found in most color science books. The MATLAB program “cri00,” which is available as supplementary material (see [GM]), contains all formulas that are used in the calculation of the CRI_{00} .

First, the CCT is calculated for the given test light source t by determining the closest Planckian radiator (blackbody) in the CIE 1960 (u, v) diagram (see Fig. 3.1).

Therefore, we compute the temperature T such that, in the uv diagram, the distance

$$\Delta C = \sqrt{[u_t - u_p(T)]^2 + [v_t - v_p(T)]^2}$$

color samples		Munsell (14)		Macbeth ColorChecker (10)		
Lamp	CCT [K]	R_a	CRI_{00}	$R96_a(c)$	$R96(\text{TCC/LAB})_a$	CRI_{00}
FL3.1	2932	51.14	51.00	54.82	58.14	51.00
FL2	4225	64.16	65.68	64.74	66.51	62.78
FL7	6497	90.19	90.14	90.41	89.73	88.99
FL11	3999	82.84	82.25	80.02	81.14	81.58
HCI-T	2960	86.95	85.82	84.94	87.64	85.23
HQL-R	3426	56.77	50.90	56.31	60.91	50.68
T5-H0	6499	93.82	94.46	93.87	92.79	93.23
WW LED	3270	70.49	69.97	71.69	73.44	71.07
CW LED	11171	82.75	82.03	34.61	67.03	80.91
LED mix	3112	94.17	96.30	80.46	84.26	95.78

Table 3.1: General CRIs calculated with the standard CIE method (R_a), the updated CIE proposals ($R96_a(c)$ and $R96(\text{TCC/LAB})_a$), and our method (CRI_{00}) for ten lamps. The first four lamps, FL3.1, FL2, FL7, and FL11, are typical fluorescent lamps defined by the CIE [CIE04]. The spectral power distributions for the next three, HCI-T (powerball lamp), HQL-R (mercury vapor lamp), and T5-H0 (fluorescent lamp), as well as for the LED sources, WW LED (warm white Luxeon LED), CW LED (cold white Luxeon LED), and LED mix (mixed spectral power distribution from different colored LEDs), were obtained from Bartenbach LichtLabor.

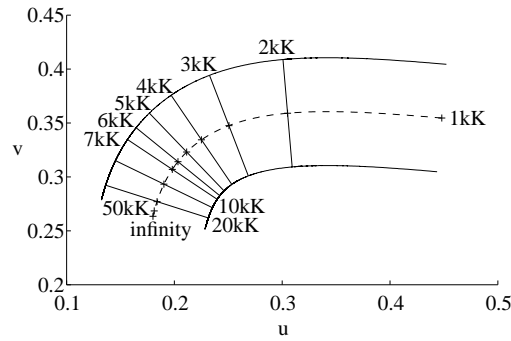


Figure 3.1: The Planckian locus (dashed line) with selected temperature isolines and the borders of the valid domain at a distance of 0.05 in the CIE 1960 UCS (u, v) diagram.

between the test light (u_t, v_t) and the Planckian locus at temperature T $[u_p(T), v_p(T)]$ is minimal. The coordinates u and v of the test light and the blackbody are computed from their chromaticity coordinates (x, y) by

$$u = \frac{4x}{-2x + 12y + 3} \quad \text{and} \quad v = \frac{6y}{-2x + 12y + 3}.$$

3 Color Rendering Indices in Global Illumination Methods

Depending on the CCT, the reference light is determined either as the closest Planckian radiator for temperatures of < 5000 K or as the closest CIE D illuminant (daylight) for temperatures of > 5000 K. The formulas for the SPDs of blackbodies and phases of daylight for given temperatures can be found in [CIE04].

The test samples – 14 Munsell colors as in the standard CIE method or eight Macbeth ColorChecker colors plus two skin tones as in $R96_a$ – are then illuminated with the test light t and the reference light source r . The CIEXYZ tristimulus values are calculated for the SPDs of the test light source Φ_t yielding $(X, Y, Z)_t$, the reference light source Φ_r yielding $(X, Y, Z)_r$, and for all test samples i illuminated by both light sources yielding $(X, Y, Z)_{t,i}$ or $(X, Y, Z)_{r,i}$, respectively.

To account for chromatic adaptation, we apply the linearized Bradford transformation to $(X, Y, Z)_{t,i}$, where we identify the white points with the current illuminant. The tristimulus value $(X, Y, Z)_{t,i}$ of the test sample i illuminated by the test light source t is thus mapped to $(X, Y, Z)'_{t,i}$ to account for the chromatic adaptation from white point $(X, Y, Z)_t$, i.e., the test light source, to white point $(X, Y, Z)_r$, i.e., the reference illuminant. This linearized Bradford chromatic adaptation transformation is defined as

$$(X, Y, Z)'_{t,i} := (X, Y, Z)_{t,i} \cdot \mathbf{M} \cdot \begin{pmatrix} \rho_r/\rho_t & 0 & 0 \\ 0 & \gamma_r/\gamma_t & 0 \\ 0 & 0 & \beta_r/\beta_t \end{pmatrix} \cdot \mathbf{M}^{-1},$$

with

$$\mathbf{M} = \begin{pmatrix} 0.8951 & -0.7502 & 0.0389 \\ 0.2664 & 1.7135 & -0.0685 \\ -0.1614 & 0.0367 & 1.0296 \end{pmatrix}$$

and

$$\begin{aligned} (\rho_t, \gamma_t, \beta_t) &= (X, Y, Z)_t \cdot \mathbf{M} \\ (\rho_r, \gamma_r, \beta_r) &= (X, Y, Z)_r \cdot \mathbf{M}, \end{aligned}$$

where (ρ, γ, β) are the values in the cone response domain that describe the corresponding (X, Y, Z) tristimuli.

Both the reference values $(X, Y, Z)_{r,i}$ and the adapted test values $(X, Y, Z)'_{t,i}$ are then transformed to the CIELAB space using the reference light source $(X, Y, Z)_r$ as reference white point. For these values $(L^*, a^*, b^*)_{r,i}$ and $(L^*, a^*, b^*)'_{t,i}$ the CIEDE2000 color differences

$$\begin{aligned} \Delta E_{00}^i &= \Delta E_{00}^i [(L^*, a^*, b^*)_{r,i}; (L^*, a^*, b^*)'_{t,i}] = \\ &= \sqrt{\left(\frac{\Delta L'}{k_L S_L}\right)^2 + \left(\frac{\Delta C'}{k_C S_C}\right)^2 + \left(\frac{\Delta H'}{k_H S_H}\right)^2 + R_T \left(\frac{\Delta C'}{k_C S_C}\right) \left(\frac{\Delta H'}{k_H S_H}\right)} \end{aligned}$$

are calculated.

The lightness difference $\Delta L'$, the chroma difference $\Delta C'$, the hue difference $\Delta H'$, and the corresponding weighting functions S_L , S_C , and S_H as well as the rotation function R_T are computed from the CIELAB values as given by the CIE [CIE04], or more detailed, by

Sharma et al. [SWD05]. The parametric factors k_L , k_C , and k_H , which are used to account for variations in experimental conditions, are all set to 1.

We calculate our new special CRIs CRI_{00}^i and the general color-rendering index CRI_{00} , such as in the CIE methods as

$$\text{CRI}_{00}^i = 100 - c \cdot \Delta E_{00}^i \quad \text{and} \quad \text{CRI}_{00} = \frac{1}{n} \sum_{i=1}^n \text{CRI}_{00}^i,$$

where $n = 8$ if the 14 Munsell color samples from the standard CIE method are used, or $n = 10$ if the ten Macbeth ColorChecker samples as recommended for $R96$ are used. Thus, the general CRI_{00} is the arithmetic mean of the first eight special rendering indices if the original set of test samples is used, or the arithmetic mean of all ten special CRI_{00}^i values if the new test samples are used. The constant c is set to 9.097 if $n = 8$, or to 6.927 if $n = 10$, respectively, to obtain a CRI_{00} of 51 for the CIE standard fluorescent lamp FL3.1 in both cases.

Numerical results for our new method are presented in Tables 3.1 to 3.3. In Table 3.1, general CRIs computed with our method are opposed to results from the standard CIE method and the updated CIE proposal for seven customary light sources and three types of LED illuminants. The CCT values given were calculated in MATLAB using a minimum search algorithm (see [GM]) to find the closest Planckian radiator and thus vary slightly from the values published in [CIE04]. The CRI_{00} results in Table 3.1 show that the choice of the set of test samples does not significantly change the general CRIs. The results for our proposed CRI_{00} are very similar to the values of the standard CIE method R_a , which seems to be desirable as for the updated CIE methods $R96_a(c)$ and $R96(TCC/LAB)_a$ the CIE ‘‘calculated the c value that would keep the average of the R_a values of these (107 from national committees and lamp manufacturers obtained) lamps constant.’’ [CIE99] The low $R96_a(c)$ value of the cold white LED is caused by using the reference light source D65 with a CCT of ~ 6500 K for a lamp with a CCT of $> 11,000$ K. The distance ΔE_{ab} in the CIELAB color space between these two lamps is > 30 compared to a maximum value of 15 for all other test light sources and their associated reference illuminants. Thus, the use of $R96_a(c)$ seems to be problematic for test light sources far away from all six reference sources in the CIELAB space, such as lamps with a high CCT.

i	R_i	CRI_{00}^i									
1	67.76	72.86	5	64.25	66.04	9	-8.30	63.71	12	35.54	4.75
2	80.02	72.40	6	66.31	62.30	10	48.20	56.15	13	69.54	66.92
3	85.15	79.43	7	81.74	75.25	11	49.73	59.50	14	90.75	85.03
4	63.26	64.32	8	55.40	67.13						

Table 3.2: Special CRIs calculated using the 14 Munsell color samples with the standard CIE method (R_i) and our method (CRI_{00}^i) for the WW LED (warm white Luxeon LED).

In Tables 3.2 and 3.3, the special CRIs for the warm white Luxeon LED are presented. Table 3.2 contains results for the standard CIE method and our proposed CRI_{00} both using the standard test sample set of 14 Munsell colors. Table 3.3 shows the values obtained from the

3 Color Rendering Indices in Global Illumination Methods

i	$R96_i(c)$	$R96(TCC/LAB)_i$	CRI_{00}^i	i	$R96_i(c)$	$R96(TCC/LAB)_i$	CRI_{00}^i
1	71.77	73.39	74.13	6	32.26	36.64	48.32
2	72.04	73.81	57.08	7	45.88	49.14	70.10
3	69.65	71.75	65.46	8	78.89	79.90	68.54
4	79.50	81.11	84.64	9	95.05	95.10	82.53
5	75.70	77.52	79.06	10	96.12	96.05	80.89

Table 3.3: Special CRIs calculated using the eight Macbeth ColorChecker samples plus two skin tones with the methods $R96_i(c)$ and $R96(TCC/LAB)_i$ as proposed by the CIE in [CIE99], and our method (CRI_{00}^i) for the WW LED (warm white Luxeon LED).

updated CIE methods $R96_a(c)$ and $R96(TCC/LAB)_a$, and our proposed CRI_{00} now using the test sample set of eight plus two Macbeth ColorChecker samples. Problems with the application of the standard CIE method to LED light sources have been observed by Bodrogi et al. [BCSS04], Schanda [Sch07], and the CIE [CIE07]. In Table 3.2, the difference between R_i and CRI_{00}^i for test sample 9 illuminated by the warm white LED is remarkable and complies with the maximum color difference for test sample 9 in [BCSS04]. Moreover, discrepancies regarding the CIE special color-rendering index R_9 for LED sources emerged in perceptual tests at Bartenbach LichtLabor [Kno06]. In these informal tests, probands stated that the red test sample looked similar under the reference and the LED test light source, but the calculated special color-rendering index R_9 was low.

The supplementary material (see [GM]) contains a MATLAB program “cri00” for calculating the proposed color-rendering index CRI_{00} and a demonstration program “cri00_demo” that computes all special indices CRI_{00}^i and the general index CRI_{00} for the CIE standard fluorescent lamps FL3.1, FL2, FL7, and FL11.

3.4 Global Illumination Methods

For different purposes (such as psychophysical tests, lighting technology, or architectural lighting), it is crucial to model real-world scenes as accurately as possible. Predictive renderings in architectural design should be both photorealistic and physically correct. When setting up lighting concepts, interior designers and lighting engineers must take care of standards concerning luminance, illuminance, reflection coefficients, or CRIs. Therefore, it is important to be able to refer to a lighting computer program that provides photometrically correct values within renderings. As described in Section 3.3, it is only possible to compute CRIs from spectral data for reflectances and SPDs, and for this reason a spectral renderer is needed when CRI calculations shall be implemented.

Because the physically based rendering package RADIANCE [War94, WS98] is known to be an accurate rendering engine [UWP05, GMD08], we decided to set up a spectral renderer based on this open-source lighting simulation tool. Instead of RGB, we use a discrete spectrum with

81 values between 380 and 780 nm, equally spaced at every 5 nm, which is widely used in the industry. Although the number of values increases by a factor of 27, due to pipelining the computational overhead is only $\sim 40\%$. In line with the method used in RADIANCE to process brightness distribution data, input data for surface reflectances and spectral power distributions are read from files. Solely for the image output, pixel values are converted from spectrum to RGB.

For an RGB triple, the RADIANCE functions intensity and brightness are given as

$$i(R, G, B) = \max(R, G, B) \quad (3.1)$$

$$\text{and } b(R, G, B) = 0.2651 \cdot R + 0.6701 \cdot G + 0.0648 \cdot B, \quad (3.2)$$

where the coefficients in the brightness formula sum up to 1 and are correct for the nominal CRT primaries $R = (0.640, 0.330)$, $G = (0.290, 0.600)$, $B = (0.150, 0.060)$, and the true white point $W = (0.3333, 0.3333)$, given in CIE (x, y) chromaticity coordinates.

In our spectral setup, we define intensity and brightness for a spectral distribution σ as

$$i(\sigma) = \max_{380nm \leq \lambda \leq 780nm} \sigma(\lambda) \quad (3.3)$$

$$\text{and } b(\sigma) = \int_{380nm}^{780nm} \bar{y}(\lambda) \sigma(\lambda) d\lambda, \quad (3.4)$$

where \bar{y} is the color matching function for the CIE 1931 standard colorimetric observer (see [CIE04]). Therefore, the brightness $b(\sigma)$ equals the definition of the CIEXYZ tristimulus value of Y .

In the spectral version of RADIANCE, we use the brightness function for all SPDs and, hence, also to set up the list of potential light-source contributions in the “selective shadow testing” algorithm. For multiple reflected light Φ , the brightness $b(\Phi)$ can be bounded by the brightness of the light source times the intensities of the single reflection functions,

$$\begin{aligned} b(\Phi) &= \int_{380nm}^{780nm} \bar{y}(\lambda) \Phi_S(\lambda) r_0(\lambda) r_1(\lambda) \dots r_{n-1}(\lambda) d\lambda \\ &\leq \int_{380nm}^{780nm} \bar{y}(\lambda) \Phi_S(\lambda) i(r_0) i(r_1) \dots i(r_{n-1}) d\lambda \\ &= i(r_0) i(r_1) \dots i(r_{n-1}) b(\Phi_S), \end{aligned} \quad (3.5)$$

where Φ_S is the SPD of the light source, n is the number of reflections, and r_j are the reflection functions. In RADIANCE, the weight of a ray is defined as the product of the intensities of all materials hit by the ray. Thus, the inequality in Eq. 3.5 justifies that, in the spectral renderer, we use the intensity function for material spectra such as extinction, albedo or surface reflectances, and ensures that even narrowband material spectra do not force a ray to stop just because most of its spectral reflectance values are close to zero.

Finally, we compare intensity and brightness for the RGB and the spectral model. From

3 Color Rendering Indices in Global Illumination Methods

Eqs. 3.1 and 3.2 for the RGB version of intensity and brightness, we derive the inequalities

$$\begin{aligned} 0.0648 \cdot i(R, G, B) &\leq 0.0648 \cdot (R + G + B) \leq b(R, G, B), \\ b(R, G, B) &\leq b[\max(R, G, B), \max(R, G, B), \max(R, G, B)] = i(R, G, B), \\ \text{and } i(R, G, B) &\leq \frac{1}{0.0648} \cdot b(R, G, B) = 15.4321 \cdot b(R, G, B). \end{aligned}$$

Summarized,

$$0.0648 \cdot i(R, G, B) \leq b(R, G, B) \leq i(R, G, B) \leq 15.4321 \cdot b(R, G, B)$$

implies that the RGB functions intensity and brightness are in the same order of magnitude, especially in case of not purely blue colors. By contrast, for the spectral versions we only have the one-sided bound

$$b(\sigma) \leq \int_{380nm}^{780nm} \bar{y}(\lambda) i(\sigma) d\lambda = 106.855 \cdot i(\sigma)$$

by Eqs. 3.3 and 3.4, and $\int_{380nm}^{780nm} \bar{y}(\lambda) d\lambda = 106.855$.

3.4.1 Cornell Box

With our first test scene – the Cornell Box – we compare the images obtained by our spectral and naive RGB renderings and analyze the image differences with respect to brightness and color. For this standard test scene in computer graphics, the scene setup, the reflectances of the lambertian surfaces, and the SPD of the light source can be downloaded from [Cor09]. Using inter- and extrapolation, all spectra are adapted to our representation from 380 to 780 nm, all 5 nm (see Fig. 3.2(a)). For the RADIANCE simulations, the lambertian surfaces are modeled as plastic material with both specularity and roughness equal to zero. The light source is a tungsten flood light with UV filter and diffusing glass plate and is modeled in RADIANCE as totally diffuse light with the given emission spectrum. Figure 3.2(b) shows a spectral rendering of the scene.

To allow a pixel-by-pixel image comparison, we take care to trace exactly the same ray paths. For this purpose, we turn off all jitterings either by parameter settings or by removing random number generation from the code. The initialization of the hemisphere sampling in *inithemi()* in *ambcomp.c* is made independent of the current ray's weight by replacing the weight *wt* by 1.0. Also the random numbers that define the direction of a single ambient sample ray are set to 0.5 in *divsample()* in the same file. Additionally, the shadow threshold check that is based on brightness values in the *direct()* routine in *source.c* is removed, i.e., the threshold is set to 0 (compare RADIANCE source code on [Rad10]). To avoid subdivision, the light source is modeled as a point light source having the same cosine brightness distribution as a flat source. By using *-dj = 0* all rays that account for the light source are sent to the center of the sphere. Moreover, we switch off irradiance caching (*-aa = 0*), set the number of ambient bounces to *-ab = 2*, the number of ambient divisions to *-ad = 400*, the number of ambient supersamples to *-as = 0*, and remove the lower limit for the weight of rays

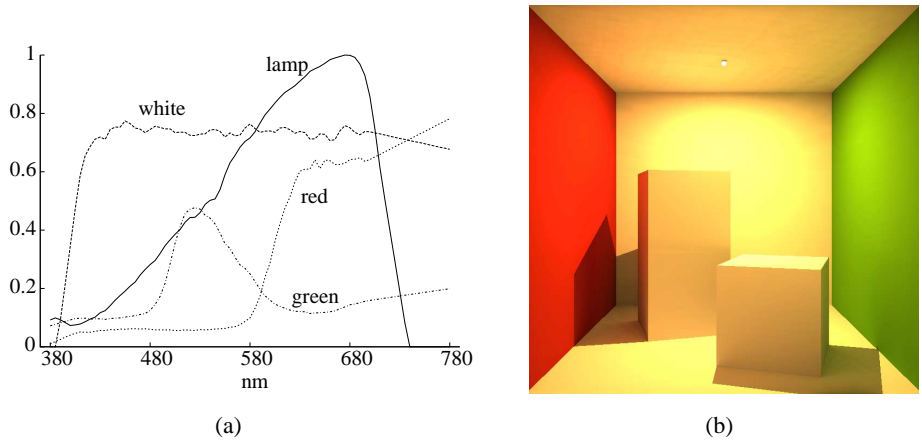


Figure 3.2: Cornell Box: (a) reflection spectra of the lambertian materials “white”, “green”, and “red”, and the SPD of the light source (scaled to a maximum of 1) and (b) spectral rendering.

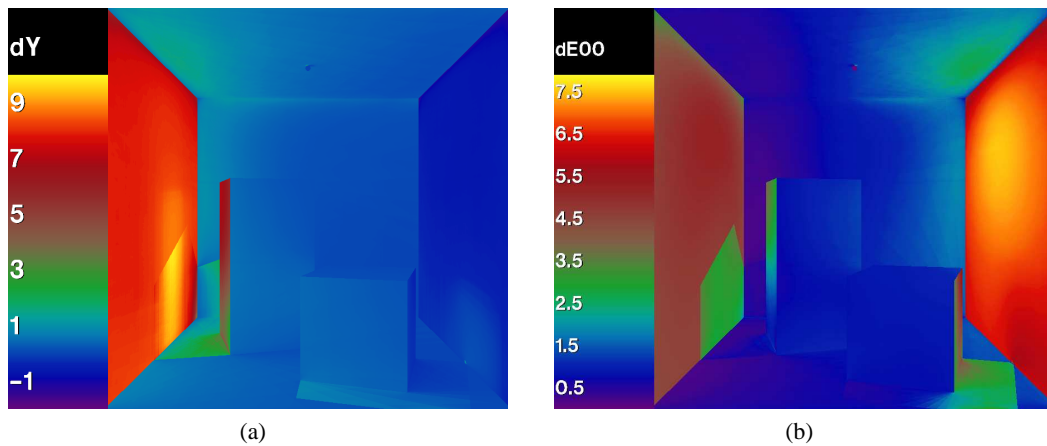


Figure 3.3: The Cornell Box: (a) relative brightness differences in percent between the naive RGB and the spectral solution (maximum: 9.85%, minimum: -1.59%) and (b) CIEDE2000 total color differences (maximum: 7.64, minimum: 0.00).

$-lw = 0$. We render the images using one sample ray per pixel ($-ps = 1$) and send each eye ray through the center of its pixel ($-pj = 0$).

Figure 3.3 shows false-color images for brightness differences (left) and color differences (right) between the naive RGB and the spectrally rendered pictures. Large differences can be seen both in brightness (especially at the red wall) and color (mainly at the green, but also at the red wall). The brightness differences are shown relatively, in percent with the RGB solution defining the reference. In the right image, significant color differences do not only occur at the

colored walls themselves, but also in regions where reflected light from these walls dominates (e.g., at the sidewalls of the white boxes and on the ceiling near the colored walls).

The significant differences shown in Fig. 3.3 demonstrate inaccuracies caused by RGB rendering. The RGB approximation of spectral reflectance functions and SPDs result in errors of multiplied RGB values compared to the correct RGB values derived from the multiplied spectra.

3.4.2 Ward – Eydelberg-Vileshin Test Scene

The objective of the second test scene is the comparison of our spectral rendering engine to the RGB version using the spectral prefiltering approach as proposed by Ward and Eydelberg-Vileshin [WEV02]. Therefore, we use their fluorescent-lamp test scene together with the spectral data (see [War09]). The left sphere is modeled in RADIANCE as plastic with a specularity of 0.05, a roughness of 0, and the diffuse color Macbeth Green. The right golden sphere is

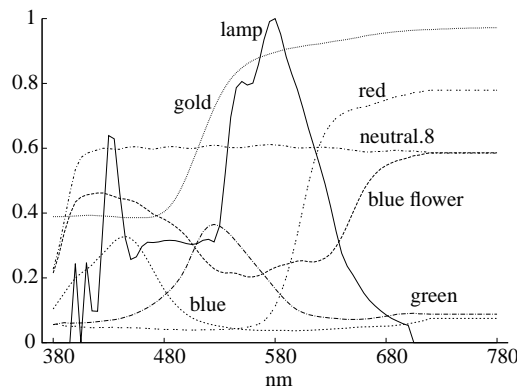


Figure 3.4: The Ward – Eydelberg-Vileshin test scene: reflection spectra of the materials and the SPD of the cool white fluorescent light source (scaled to a maximum of 1).

simulated as 100% specular metal with zero roughness, and its color is computed from the wavelength-dependent index of refraction for pure gold. All other materials are assumed to be lambertian and modeled as plastic with both specularity and roughness equal to zero. The color of the walls are Macbeth Red for the left wall, Macbeth Blue for the right wall, Macbeth Blueflower for the wall at the front, and Macbeth Neutral.8 for all other walls. The light source is a cool white fluorescent lamp modeled as totally diffuse light in RADIANCE. Figure 3.4 shows the reflection spectra of the materials and the SPD of the light source. We do not apply white balancing as it is done in their work, because we want to get real photometric values as needed for CRI calculations. The procedure for spectrally prefiltering RGB values is described in detail in their paper.

Similar to the Cornell Box test scene, we allow a pixel-by-pixel image comparison by tracing exactly the same ray paths within the prefiltered RGB and the spectral renderings. The left image in Fig. 3.5 shows our spectral solution for the Ward – Eydelberg-Vileshin test scene. On the right side, the CIEDE2000 color differences between the prefiltered RGB and our spectral solution are presented in a false-color image. As mentioned in Section 3.2, the approach of spectral

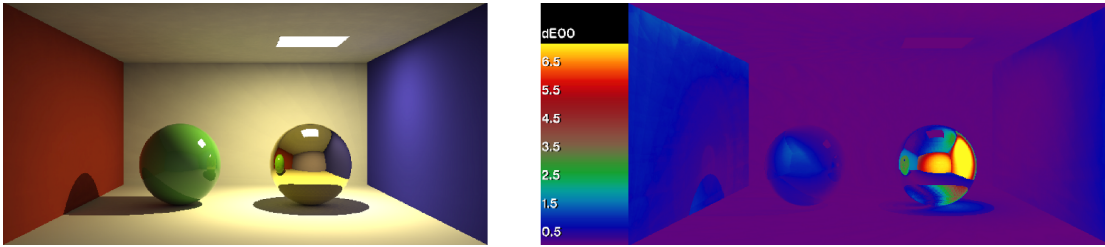


Figure 3.5: The Ward – Eydelberg-Vileshin test scene: spectral rendering (left) and CIEDE2000 color differences between the spectrally prefiltered RGB and the spectral solution (maximum: 8.06, minimum: 0.00; right).

prefiltering for RGB rendering is suitable for the direct-diffuse component but lacks accuracy for multiple reflected light, which can be seen at the golden sphere in the reflection of the blue sidewall and the “blue flower” front wall.

3.4.3 CRI Test Scene

The CRI is defined for SPDs of light sources. However, within a real-world scene, light incident on a measurement surface is composed of a direct and an indirect part. The aim of our third test scene is to show how the CRI changes with mixed direct and multiple reflected light.

Our test room is modeled by a square base area with a red linoleum floor and white plaster on the ceiling and the walls. The four lighting fixtures, which represent specular louver units made of aluminum, are equally arranged and contain fluorescent lamps. These lamps are of type T5-H0, having a CCT of 6499 K and a CRI_{00} of 94.46. The specular louver units mainly light the floor, which results in mixed direct and indirect (reflected from the floor) lighting at the walls. All reflection spectra, the SPDs, and the brightness distribution functions of the illuminants describe real-world materials and were measured at Bartenbach LichtLabor, Austria [Bar]. In RADIANCE, we model the light source using the *brightdata* modifier for lights and assign the measured luminous intensity distribution. The walls and ceiling consist of white plaster with fully lambertian reflection. The red linoleum floor is modeled by the Ward BRDF [War92], with specularity 0.0821 and roughness 0.0372 estimated from measured reflection data. For all materials, the diffuse color is given by the measured reflection spectra. Figure 3.6(a) shows the T5-H0 lamp spectrum scaled to a maximum value of 1 together with the reflection spectra of the red linoleum floor and the white plaster walls next to a spectral rendering of the scene [Fig. 3.6(b)].

For calculating the CRI within the image, we render the image with the “-i” option in RADIANCE to obtain irradiance instead of radiance values. For each pixel, we get an SPD that represents the light incident on the current surface, from which we calculate the CRI. Because this is done in a postprocessing step, any color rendering index or other photometric measure that can be derived from spectral data could be computed (e.g., the standard CIE CRI R_a or one of the R_{96_a} CRIs). Because we intend to show the applicability of CRI calculations within a global illumination method, we implement only one CRI calculation and compute our proposed CRI_{00} based on the 14 Munsell test samples to ease comparisons to the standard CIE method.

3 Color Rendering Indices in Global Illumination Methods

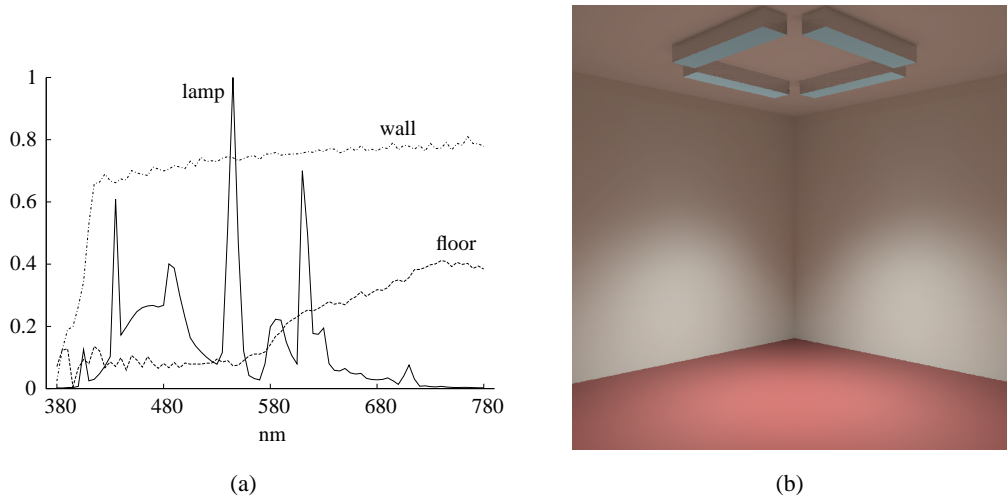


Figure 3.6: CRI test scene: (a) reflection spectra of the red linoleum floor, the white plaster walls, and the SPD of the T5-H0 light source (scaled to a maximum of 1) and (b) spectral rendering.

Except for the light source, we obtain the highest CRI_{00} values at the floor (mainly direct illumination), followed by the lower regions in the middle of the walls (direct and indirect illumination), and the upper regions of the walls as well as the ceiling (mainly indirect illumination), where the CRI is attenuated by the reflection on the red linoleum floor. Moreover, the maximum CRI_{00} (94.46) within the scene complies with the CRI_{00} of the source. The CRI_{00} distribution throughout the scene is presented as a false-color image in Fig. 3.7(a).

To make a comparison to RGB rendering possible, we use Smits' RGB-to-spectrum conversion for reflectances [Smi99], which creates physically plausible spectra from RGB values. Because we are working with SPDs instead of reflectances, we slightly change Smits' algorithm and do not set an upper limit for the spectral values. With this modified procedure, we first compute the seven spectra for white, red, green, blue, cyan, magenta, and yellow, and then perform the RGB to spectrum transformations, where we use spectrally prefiltered RGB as proposed in [WEV02].

The false-color image in Fig. 3.7(b) shows the CRI_{00} distribution resulting from the spectrally prefiltered RGB rendering followed by Smits' conversion. Throughout the scene, all CRI_{00} values are higher than the correct values obtained from spectral rendering [e.g., the maximum of 98.21, which appears for the illuminants, is significantly higher than the true CRI_{00} of the light sources (94.46)]. The problem with applying Smits' method for reflectances to SPDs is that, for a given RGB triple, the smoothest of all metamer spectra is calculated. Therefore, two metamer spectra with CRIs far apart will result in the same spectrum similar to a Planckian radiator having a very high CRI. The large differences between the CRI distributions in Fig. 3.7 underline the importance of photometric correctness in global illumination systems as provided by spectral rendering.

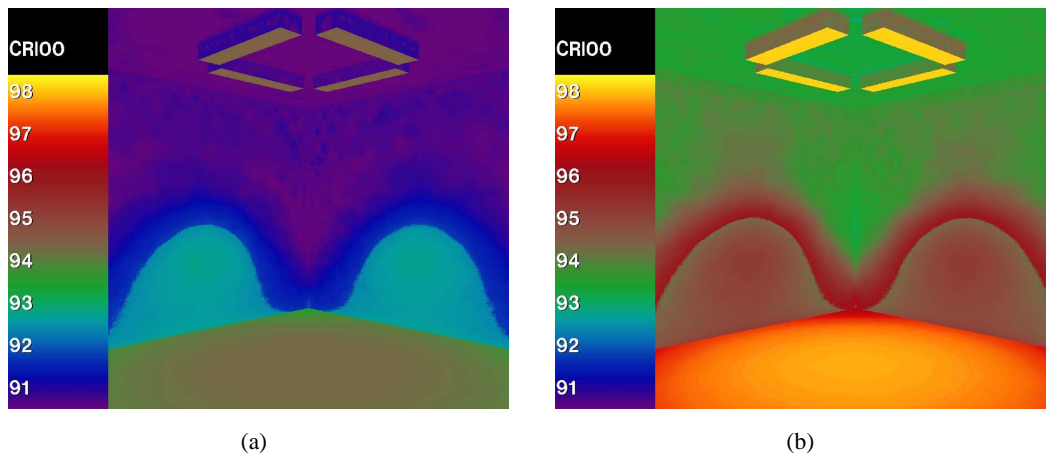


Figure 3.7: CRI test scene: (a) CRI_{00} distribution obtained by spectral rendering (maximum CRI_{00} : 94.46, minimum CRI_{00} : 90.24) and (b) CRI_{00} distribution obtained by spectrally pre-filtered RGB rendering and Smits' algorithm (maximum CRI_{00} : 98.21, minimum CRI_{00} : 92.87).

3.4.4 Real-World Seminar Room

Our fourth test scene is a not fully completed, real-world seminar room from the Lichtakademie Bartenbach. All measurements of reflection spectra and brightness distribution functions were done by our cooperation partner Bartenbach LichtLabor. The room is illuminated by four light tubes with scattering inserts, which redirect daylight from outside into the room and have different depreciation factors. The scattering inserts are made of a mirrorlike material with the purpose of distributing light almost uniformly into the room and avoiding glare from direct sunlight. The room is composed of a red linoleum floor, three fair-faced concrete walls and one plastered wall, and a plastered ceiling. The enclosures of the light tubes and additional specular louver units, which are switched off, are made of aluminum. Moreover, the room contains four white/light-gray boxes under a white table and a flat screen at the wall. In RADIANCE, the light sources are modeled as circular disks, which are placed at the bottom edge of the light tubes and have the measured brightness distribution assigned. In addition to the *illum* material for the disks, we use a *glow* material inside the light pipes to illuminate the local structure without affecting the illumination in the room. For the SPD of the light sources, we use the standard phase of daylight D65, which has a CCT of 6503.6 K and a CRI_{00} of 100, and neglect possible spectral changes due to reflections inside the light pipes. The fair-faced concrete walls are modeled as fully lambertian surfaces. The enclosures are modeled by Ward's lightly brushed aluminum [War92] with specularity 0.56 and roughness 0.11. The spectral reflectances of the materials, which were not already shown in Fig. 3.6(a), and the D65 spectrum are presented in Fig. 3.8.

Figure 3.9 shows a photo of the real room (left) together with an image of the simulated scene obtained by our spectral version of RADIANCE (right). In Fig. 3.10 the false-color image

3 Color Rendering Indices in Global Illumination Methods

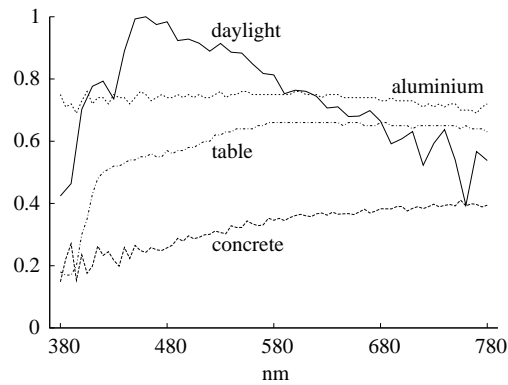


Figure 3.8: Real-world seminar room: reflection spectra of the concrete wall, the table, and the aluminium enclosures, and the SPD of the D65 daylight (scaled to a maximum of 1).



Figure 3.9: Real-world seminar room: photo taken at the Bartenbach Lichtakademie (left), and spectral rendering (right).

indicates the CRI_{00} distribution within the scene. Expectedly, the highest CRI can be found on the table and on the floor, where the main part of the illumination comes directly from the light sources. With mixed direct and indirect illumination, the CRI gets lower, which can be seen for example near the walls. Regions that are illuminated solely by indirect illumination show how much of the CRI can be lost by interreflections. For example, in the shady regions under the table or below the screen, a difference in CRI_{00} of ~ 8.5 from the CRI of the light source (100) occurs. Within the calculation of the CRI for each pixel, the CCT is computed to define a reference light source. This information can be displayed similar to the CRI using a false-color scale. Fig. 3.11 shows that the CCT of incident light can significantly change by interreflections inside the room.

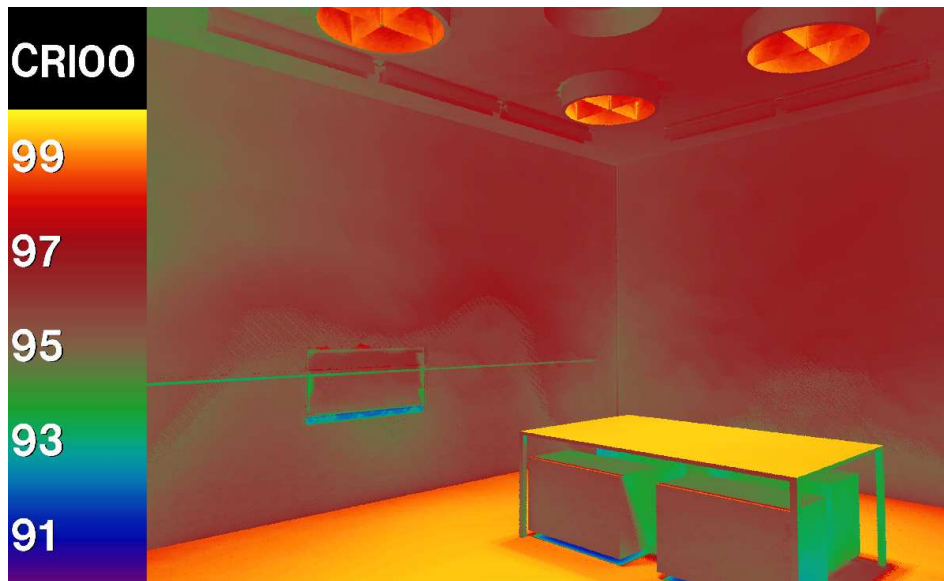


Figure 3.10: Real-world seminar room: CRI_{00} distribution (maximum CRI_{00} : 99.67, minimum CRI_{00} : 91.49).

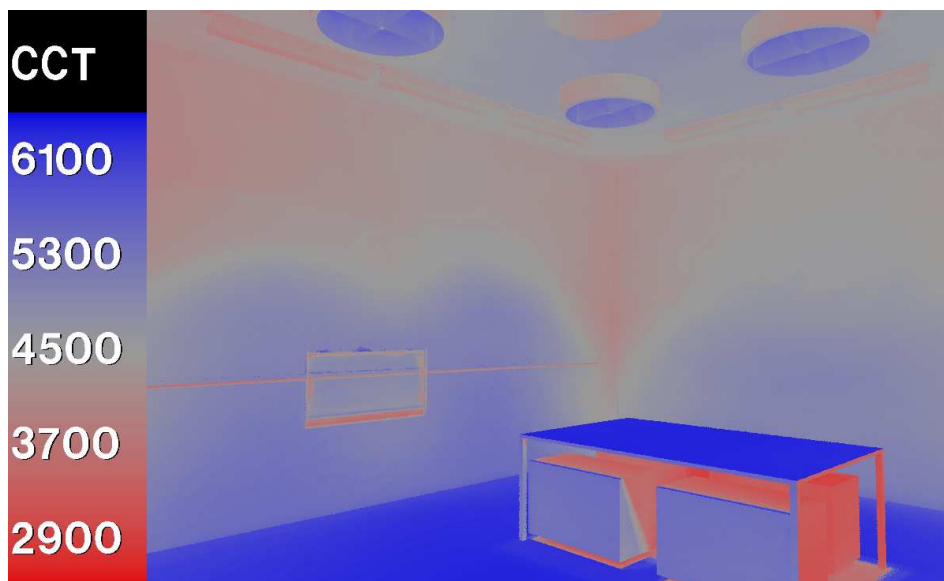


Figure 3.11: Real-world seminar room: CCT distribution (maximum CCT: 6376.67 Kelvin, minimum CCT: 2897.21 Kelvin).

3.5 Discussions and Future Work

The present work was motivated by the problem of displaying relevant measures for lighting design within a computer-generated preview of a scene. For our cooperation partner Bartenbach

3 Color Rendering Indices in Global Illumination Methods

LichtLabor, the prediction of illuminance, color-rendering index, or CCT is important whenever an architectural lighting concept is to be set up.

The update of the standard CIE method for the CRI in the form of our proposed CRI_{00} yields a measure for the color-rendering properties of light sources that describes human perception more closely. Contrary to other approaches mentioned in Section 3.2, the procedure for calculating the CRI_{00} is still in line with the standard CIE method and can therefore be easily adopted by industry. However, by following the CIE procedure, we also inherit the issue of a discontinuity for light sources with a CCT of 5000 K. This problem could not be solved thus far, but should be a main interest in future investigations.

To calculate lighting design characteristics from renderings, highly accurate data in the obtained images are required. Moreover, some characteristics such as the CRI, can only be calculated if spectral data are available. Thus, spectral rendering is necessary for reasons of both accuracy and feasibility. Our spectral version of RADIANCE allows interior or lighting designers to predict and change important measures, such as CCT or CRI, in computational simulations by using various wall paints or specifically placing colored items. Computer-generated images for psychophysical tests are another application for spectral rendering because there the pictures require physically correct data as well. In consideration of the obtained accuracy, the drawback of spectral rendering in terms of 40% computational overhead seems to be subordinate. As shown in Section 3.4, interreflections can alter the CRI or CCT significantly. In follow-up work, we want to analyze these effects for mirrorlike reflections that happen in daylight redirection systems, such as horizontal mirror ducts or vertical light pipes.

3.6 Conclusion

We presented a modernized method for the calculation of CRIs based on state-of-the-art colorimetric methods. Our update affected the standard CIE algorithm from 1974 in three main points, but did not change the basic setup of the procedure. We replaced the $CIEU^*V^*W^*$ by the CIELAB color space, the Von Kries transformation by the linearized Bradford transformation for chromatic adaptation, and the Euclidian distance by the CIEDE2000 color difference formula. This approach has been evaluated for customary light sources and LED illuminants, and is promising to be better qualified for the prediction of color-rendering perceptions.

Furthermore, we evaluated CRIs in scenes with global, mixed direct and indirect illumination. Therefore, we presented an approach to set up a spectral rendering engine based on the open-source software RADIANCE and showed the advantages of spectral rendering over RGB-based methods. Finally, we exemplified the application of CRI and CCT calculations in global illumination methods by means of a real-world test scene.

Acknowledgments

The authors thank Christian Knoflach and Rico Thetmeyer from our cooperation partner Bartenbach LichtLabor in Aldrans, Austria, for the seminar-room test scene and the associated photometric data. Parts of this research were supported by the FIT-IT Program of the BMVIT (Bundesministerium für Verkehr, Innovation und Technologie) and the FFG with Grant No. 816009.

4 Estimating Melatonin Suppression and Photosynthesis Activity in Real-World Scenes from Computer Generated Images

Sleep, those little slices of death; Oh how I loathe them.

(Edgar Allan Poe, 1809-1849)

In lighting design and architectural illumination planning simulations of luminance and illuminance distributions within scenes are performed using rendering tools such as RADIANCE. In this paper we focus on the evaluation by two action spectra other than the luminous efficiency function – the circadian action function describing the melatonin suppression and the photosynthesis action function. We show how indices that are derived from these action spectra can be calculated from spectrally rendered images of a real-world scene. For both action spectra we derive approximations based on the CIE color matching functions that allow estimations of the corresponding index from RGB rendered images. We evaluate the differences between the spectral results and the RGB approximations for an office room with three different types of illumination.

4.1 Background

Physically based rendering packages such as RADIANCE are used in lighting design and architectural illumination planning for simulations of luminance and illuminance distributions. Especially for daylight simulations and daylight factor calculations this rendering tool is widely used and was shown to be accurate in [Mar99, UWP05, GMD08]. However, spectral rendering is necessary if highly accurate results are desired as for example color shifts may occur when calculations are performed in the RGB color space [RB06, GMD09b].

In the present study not only the CIE photopic luminous efficiency function $V(\lambda)$ that is used to calculate (il)luminances from (ir)radiances and which equals the CIE color-matching function \bar{y} [CIE04], but also other weighting functions are considered. In detail, two action spectra are used for evaluations in a real-world test scene: the circadian action function describing the melatonin suppression and the photosynthesis action spectrum representing a plant's photosynthesis activity.

Circadian action function

The hormone melatonin, which is mainly secreted during the night, is primarily responsible for the regulation of the circadian rhythm. Light in general and radiation in the blue part of the visible spectrum in particular suppresses the secretion of this hormone. Gall [Gal09] defines a circadian action function $c(\lambda)$ that is based on experimental data from Brainard [BHG*01] and Thapan [TAS01] for light-induced melatonin suppression. The spectral distribution of $c(\lambda)$ is shown in Figure 4.1.

Using this circadian action function, Gall calculates the circadian radiation quantity X_{ec} , which we refer to as C , by

$$C = \int \sigma(\lambda)c(\lambda)d\lambda \quad (4.1)$$

and defines the circadian action factor a_{cv} in relation to the CIE luminance Y as

$$a_{cv} = \frac{C}{Y} = \frac{\int \sigma(\lambda)c(\lambda)d\lambda}{\int \sigma(\lambda)\bar{y}(\lambda)d\lambda} \quad (4.2)$$

for a given spectral power distribution (SPD) σ . In the current study we use the values for Gall's circadian action function $c(\lambda)$ that are given in [Gal09] and simulate the distribution of the circadian action factor a_{cv} within a real-world scene.

Photosynthesis action spectrum

Plants as well as some algae and bacteria are able to generate carbohydrates and oxygen from carbon dioxide, water, and light energy. The action spectrum for this photosynthesis process differs for various plants and is subject of scientific research [Taz99a, Taz99b].

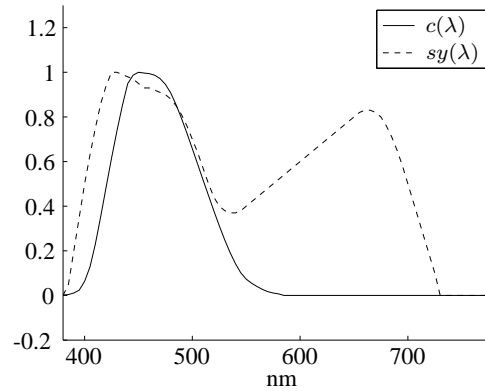


Figure 4.1: Spectral distributions of the circadian action function $c(\lambda)$ as defined by Gall and the photosynthesis action spectrum $sy(\lambda)$ as given in DIN 5031-10.

In the current study we use the photosynthesis action spectrum $sy(\lambda)$ that is defined by the German Institute for Standardization (DIN) in the document DIN 5031-10 [DIN00] and calculate

the photosynthesis activity SY from

$$SY = \int \sigma(\lambda) sy(\lambda) d\lambda \quad (4.3)$$

for a SPD σ . The spectral distribution of $sy(\lambda)$ is shown in Figure 4.1.

4.2 Spectral Rendering

For spectral rendering with RADIANCE [War94, WS98] various proposals were presented in the literature. Both Delahunt and Brainard [DB04] and Ruppertsberg and Bloj [RB06, RB08] use N-step algorithms with multiple calls to the RGB renderer together with a post-processing step to gather the images. Delahunt and Brainard render a single monochromatic image for each wavelength, whereas Ruppertsberg and Bloj put independent wavelengths in each of the three channels. In the latter case wavelengths from the red, green, and blue part of the spectrum should be combined because otherwise the calculation of brightnesses in RADIANCE given by

$$b(R, G, B) = 0.265 \cdot R + 0.670 \cdot G + 0.0648 \cdot B \quad (4.4)$$

might lead to inaccuracies in algorithms that are steered by this function. Geisler-Moroder and Dür [GMD09b] present an approach for spectral rendering with RADIANCE using a discrete representation of the spectrum with 81 values equally spaced between 380nm and 780nm. They expand the brightness function from the RGB approximation to the CIE tristimulus value Y , i.e.

$$b(\sigma) = Y(\sigma) = \int_{380}^{780} \sigma(\lambda) \bar{y}(\lambda) d\lambda \quad (4.5)$$

for a SPD σ and the CIE color-matching function \bar{y} .

For the current study we adopt and slightly modify this approach. Because RADIANCE is intended to be used for simulations of real-world scenes as observed by humans, the brightness function that approximates the CIE Y tristimulus and thus the human brightness perception is used for steering algorithms in the ray tracing process. However, since we use different weighting functions for brightness ($\bar{y}(\lambda)$), melatonin suppression ($c(\lambda)$), and photosynthesis activity ($sy(\lambda)$), we re-define the brightness function in RADIANCE via the constant 1-function as

$$b(\sigma) = \int_{380}^{780} 1 \cdot \sigma(\lambda) d\lambda. \quad (4.6)$$

In this way all parts of the spectrum are treated equally and inaccuracies in brightness-steered algorithms of RADIANCE are avoided in exchange for a slight computational overhead. In a post-processing step we are then able to apply the sensitivity functions $\bar{y}(\lambda)$, $c(\lambda)$, and $sy(\lambda)$, and compute the indices C , Y , and SY from a single spectral image.

4.2.1 Test scene

Our test scene shows an office room that contains three different sources of illumination – windows, ceiling lamps, and computer monitors. Figure 4.2(a) shows an overview of the scene

4 Estimating Melatonin Suppression and Photosynthesis Activity

and Figure 4.2(b) the view from the the front workplace. The windows are simulated as light sources using the spectrum of the CIE standard illuminant D65 [CIE04] with a luminance of 1000cd/m^2 . The spectra of both the TFT display, that emits white light only, and the LED ceiling lamps (Luxeon Rebel cold white) were measured by our cooperation partner Bartenbach LichtLabor. The luminance of the monitors are set to 250cd/m^2 and the ceiling lights are modeled to have a luminous flux of 1500lm each. As for this study primarily the spectrum and not the angular distribution of the light is important, all sources are modeled as totally diffuse emitters. Figure 4.3 shows the spectra of the three light sources together with the main reflectance spectra of the scene, i.e. the floor, the walls (including the ceiling), and the wooden desks. The reflectance spectra of white plaster (walls, ceiling), cherry wood, and aluminium (e.g. for the ceiling light fixtures) were measured by our cooperation partner Bartenbach LichtLabor. For the other objects we use reflectance spectra from the Macbeth ColorChecker chart [MMD76] that are available on [Bab09], e.g. Macbeth Neutral 6.5 for the floor, Macbeth Foliage for the chairs, and Macbeth Orange and Macbeth Orange Yellow for the containers and their fronts.



Figure 4.2: Office test scene: (a) overview of the test scene containing three different sources of illumination: four light sources that simulate the windows, two LED ceiling lamps, and two computer monitors and (b) view from the front workplace that is important for the evaluation of the circadian action factor a_{cv} as it simulates the field of view of a person working at the desk.

4.2.2 Weighting functions

Given a weighting function $\omega(\lambda)$ such as $c(\lambda)$ or $sy(\lambda)$, the associated index $\Omega(\sigma)$ for a spectral power distribution σ is defined by

$$\Omega(\sigma) = \int_{380}^{780} \sigma(\lambda)\omega(\lambda)d\lambda. \quad (4.7)$$

Thus, Ω becomes a functional on the Hilbert space $L^2([380\text{nm}, 780\text{nm}])$ that contains all spectra $\sigma(\lambda)$ that satisfy

$$\int_{380}^{780} \sigma(\lambda)^2 d\lambda < \infty. \quad (4.8)$$

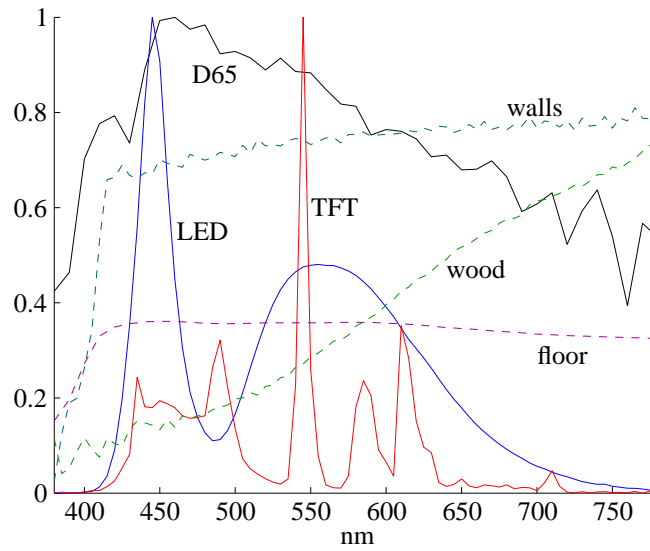


Figure 4.3: Light source spectra (each scaled to a maximum of 1) and main reflectance spectra used in the test scene: the windows are modeled with the CIE standard phase of daylight D65, the spectra for the LED lamps and the monitors as well as the reflectances of cherry wood and white plaster were measured by our cooperation partner Bartenbach LichtLabor, and the floor is modeled with the dark gray color Macbeth Neutral 6.5 from the Macbeth ColorChecker chart.

For example the CIE XYZ tristimulus values can be written as functionals

$$X(\sigma) = \int_{380}^{780} \sigma(\lambda) \bar{x}(\lambda) d\lambda, \quad (4.9)$$

$$Y(\sigma) = \int_{380}^{780} \sigma(\lambda) \bar{y}(\lambda) d\lambda, \quad (4.10)$$

$$\text{and } Z(\sigma) = \int_{380}^{780} \sigma(\lambda) \bar{z}(\lambda) d\lambda, \quad (4.11)$$

where \bar{x} , \bar{y} , and \bar{z} are the color-matching functions for the CIE 1931 standard colorimetric observer [CIE04] (see Figure 4.7(a)). Evaluating the functional $Y(\sigma)$ for each pixel's SPD σ in a spectrally rendered image yields the luminance distribution if the image contains radiances, and the illuminance distribution if the image contains irradiances, respectively.

4.2.3 Circadian action function

From the radiances within a spectrally rendered image the circadian action factor a_{cv} can be computed in a post-processing step. For the SPD σ of each pixel the functionals C and Y are

4 Estimating Melatonin Suppression and Photosynthesis Activity

evaluated and the circadian action factor

$$a_{cv}(\sigma) = \frac{C(\sigma)}{Y(\sigma)} = \frac{\int_{380}^{780} \sigma(\lambda)c(\lambda)d\lambda}{\int_{380}^{780} \sigma(\lambda)\bar{y}(\lambda)d\lambda} \quad (4.12)$$

can be displayed in a falsecolor image. Figure 4.4 shows the distribution of a_{cv} as perceived when working at the front desk. In Figure 4.5 the a_{cv} values of the scene when seen from outside are presented. In the falsecolor images the a_{cv} values of all three light sources exactly correspond to the analytical results of $a_{cv}(\lambda)$ given in Table 4.1. Comparing the results for the three light sources shows that the light-induced melatonin suppression is strongest for D65 followed by the TFT monitor light and lastly the LED lamp.

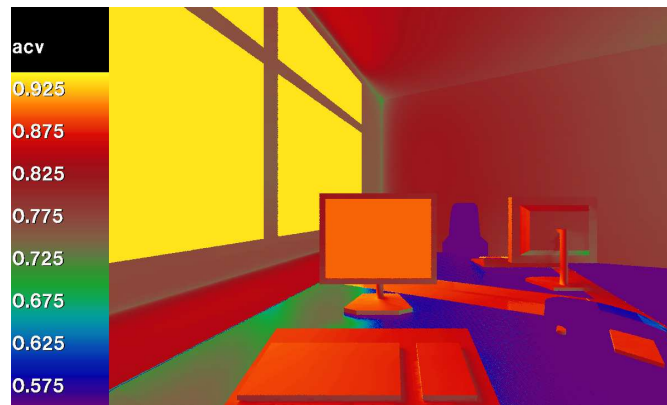


Figure 4.4: Distribution of the circadian action factor $a_{cv}(\sigma)$ calculated from the spectral rendering in the field of view of a person working at the front desk.

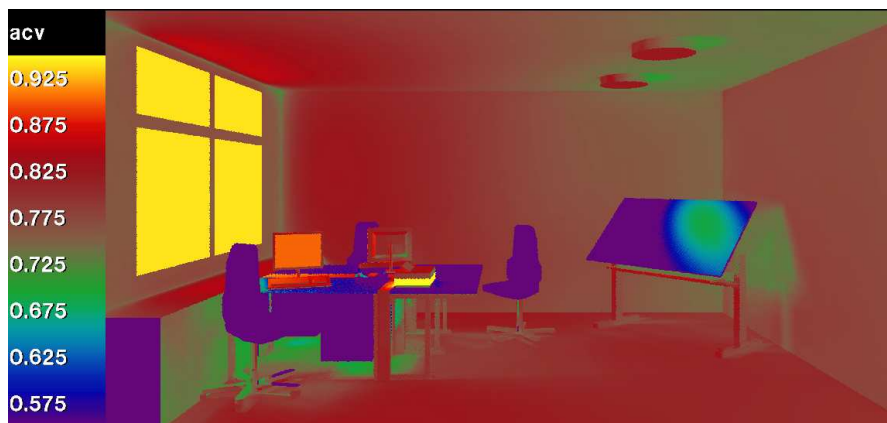


Figure 4.5: Distribution of the circadian action factor $a_{cv}(\sigma)$ inside the scene calculated from the spectral rendering. The analytical results for the three light sources given in Table 4.1 exactly correspond to the image.

4.2.4 Photosynthesis activity

For the photosynthesis activity the incident light is decisive. We thus render the images of our test scene again using the RADIANCE option “-i” to obtain irradiances instead of radiance values. To calculate the photosynthesis index SY from the irradiance spectrum σ at each pixel within the rendered images the functional $SY(\sigma)$ is evaluated:

$$SY(\sigma) = \int_{380}^{780} \sigma(\lambda) sy(\lambda) d\lambda. \quad (4.13)$$

Figure 4.6 shows the SY distribution within the scene and thus proposes the “ideal place” to put plants in the office – on the windowsill or on the desk close to the window. As the index SY is not divided by the brightness of the corresponding SPD it is an absolute measure and depends on both the quality and the quantity of incident light. Thus, the “ideal place” for a plant could for example be changed by increasing the LED’s emittance what in turn would lead to uncomfortably high illuminances and glare for the people working in the office.

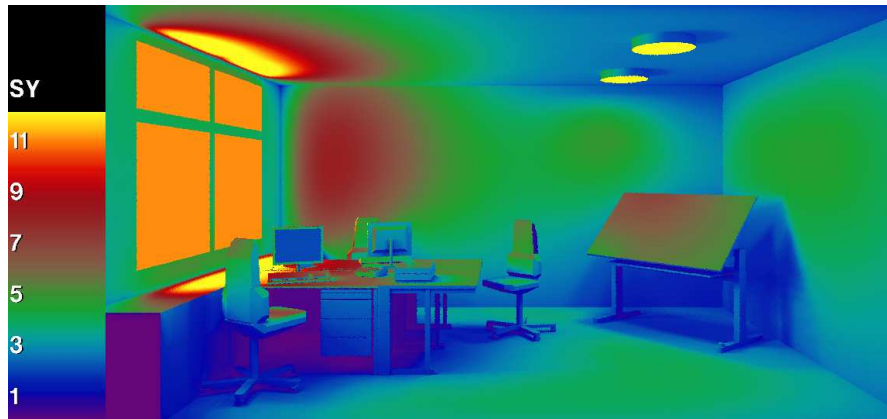


Figure 4.6: Distribution of the photosynthesis activity $SY(\sigma)$ inside the scene calculated from the spectral rendering. The windowsill or the parts of the desk close to the window are “ideal places” to position a plant.

4.3 RGB Approximation

In RADIANCE the RGB approximation of luminances and illuminances by Equation 4.4 usually works well, what is desirable and necessary as these are the main indices needed in lighting design and other applications of this physically based renderer. Similar to the approximation of the CIE tristimulus value Y we try to find an approximation to the indices a_{cv} and SY based on the three color-matching functions \bar{x} , \bar{y} , and \bar{z} .

To calculate the indices C and SY from the values in an RGB rendered image as a weighted sum, we need to derive coefficients (r_C, g_C, b_C) and (r_{SY}, g_{SY}, b_{SY}) for the three channels R, G, and B similar to Equation 4.4.

4 Estimating Melatonin Suppression and Photosynthesis Activity

Gall and Bieske [GB04] propose to approximate the circadian action factor a_{cv} via the CIE chromaticity coordinates (x, y) as

$$a_{cv} \approx \frac{\int \bar{z}(\lambda)\sigma(\lambda)d\lambda}{\int \bar{y}(\lambda)\sigma(\lambda)d\lambda} = \frac{Z}{Y} = \frac{1-x-y}{y}. \quad (4.14)$$

For the light sources in our test scene Equation 4.14 yields results with relative errors of +15.7% for D65, +42.2% for the LED lamp, and +20.4% for the monitor light. Gall's approximation of the circadian radiation quantity C is only based on the CIE color-matching function \bar{z} and thus leaves room for improvement by calculating an approximation based on all three color-matching functions.

Generally, we look for an approximation of the functional $\Omega(\sigma)$ from Equation 4.7 by a linear combination

$$\Omega(\sigma) \approx k_x X(\sigma) + k_y Y(\sigma) + k_z Z(\sigma) \quad (4.15)$$

where $X(\sigma)$, $Y(\sigma)$, and $Z(\sigma)$ are the functionals describing the CIE XYZ tristimuli as given in Equations 4.9 to 4.11.

According to the Riesz representation theorem the Hilbert space $L^2([a, b])$ of functions is isomorphic to its dual space of functionals. Thus we can represent each functional Ω by its corresponding density ω and search for an approximation of ω by a linear combination of the color-matching functions \bar{x} , \bar{y} , and \bar{z} , which are the corresponding densities of the functionals X , Y , and Z :

$$\omega(\lambda) \approx k_x \bar{x}(\lambda) + k_y \bar{y}(\lambda) + k_z \bar{z}(\lambda). \quad (4.16)$$

We find this approximation ψ by an orthogonal projection of ω onto the subspace spanned by \bar{x} , \bar{y} , and \bar{z} , i.e.,

$$\psi = k_x \bar{x} + k_y \bar{y} + k_z \bar{z} \quad \text{such that} \quad (4.17)$$

$$\langle \omega - \psi, \bar{x} \rangle = \langle \omega - \psi, \bar{y} \rangle = \langle \omega - \psi, \bar{z} \rangle = 0. \quad (4.18)$$

Equation 4.18 leads to the system of linear equations

$$\begin{pmatrix} \langle \omega, \bar{x} \rangle \\ \langle \omega, \bar{y} \rangle \\ \langle \omega, \bar{z} \rangle \end{pmatrix} = G(\bar{x}, \bar{y}, \bar{z}) \cdot \begin{pmatrix} k_x \\ k_y \\ k_z \end{pmatrix} \quad (4.19)$$

where

$$G(\bar{x}, \bar{y}, \bar{z}) = \begin{pmatrix} \langle \bar{x}, \bar{x} \rangle & \langle \bar{y}, \bar{x} \rangle & \langle \bar{z}, \bar{x} \rangle \\ \langle \bar{x}, \bar{y} \rangle & \langle \bar{y}, \bar{y} \rangle & \langle \bar{z}, \bar{y} \rangle \\ \langle \bar{x}, \bar{z} \rangle & \langle \bar{y}, \bar{z} \rangle & \langle \bar{z}, \bar{z} \rangle \end{pmatrix} \quad (4.20)$$

is the Gramian matrix for the three color-matching functions \bar{x} , \bar{y} , and \bar{z} . Solving the system (4.19) for the weighting functions $\omega = c(\lambda)$ and $\omega = sy(\lambda)$ yields the approximations

$$\psi_{c(\lambda)} = -0.284\bar{x} + 0.358\bar{y} + 0.681\bar{z} \quad \text{and} \quad (4.21)$$

$$\psi_{sy(\lambda)} = 0.533\bar{x} + 0.276\bar{y} + 0.581\bar{z} \quad (4.22)$$

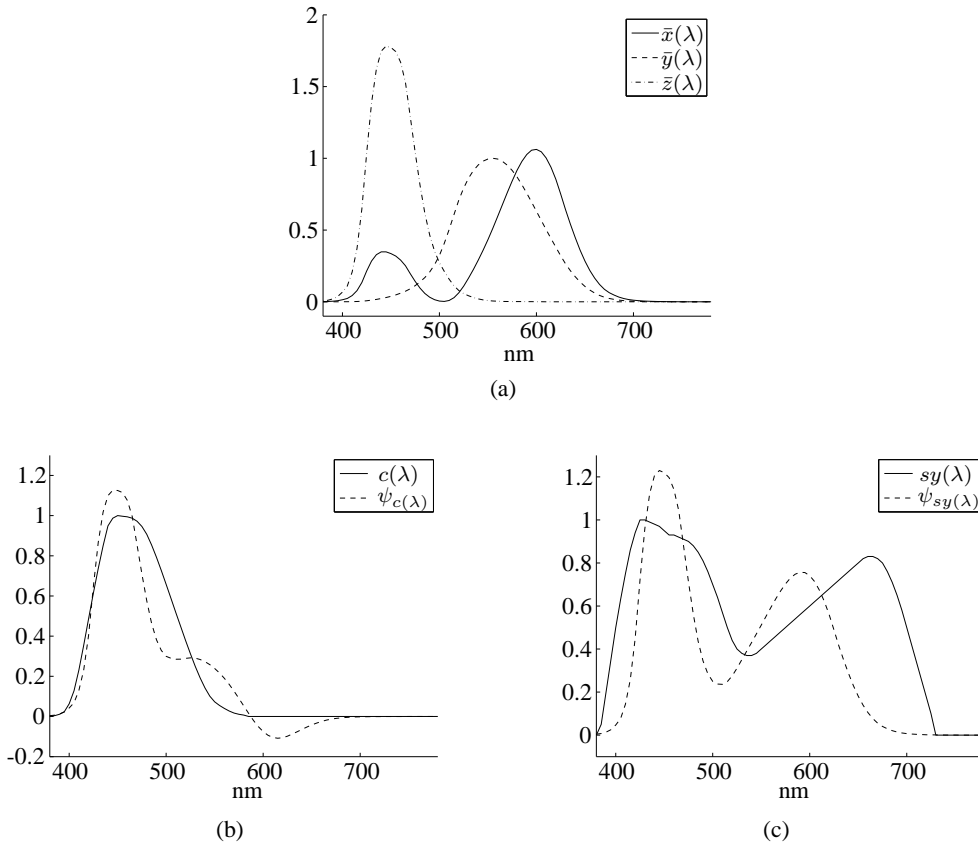


Figure 4.7: (a) The CIE color-matching functions \bar{x} , \bar{y} , and \bar{z} , (b) the circadian action function $c(\lambda)$ as defined by Gall, and the approximation function $\psi_{c(\lambda)}$ that is a linear combination of \bar{x} , \bar{y} , and \bar{z} and (c) the photosynthesis action spectrum $sy(\lambda)$ as defined in DIN 5031-10, and the approximation function $\psi_{sy(\lambda)}$ as a linear combination of \bar{x} , \bar{y} , and \bar{z} .

for the circadian and photosynthesis action spectra, respectively. In Figures 4.7(b) and 4.7(c) these approximations based on the three CIE color-matching functions (Figure 4.7(a)) are compared to the real action functions.

Multiplying by the transformation matrix of RADIANCE from RGB to XYZ gives the coefficients (r, g, b) for the approximation of the index Ω from the RGB values in the rendered image:

$$(r, g, b) = (k_x, k_y, k_z) \cdot \begin{pmatrix} 0.514 & 0.324 & 0.162 \\ 0.265 & 0.670 & 0.0648 \\ 0.0241 & 0.123 & 0.853 \end{pmatrix}. \quad (4.23)$$

Evaluating Equation 4.23 for the coefficients of the circadian action spectrum approximation $\psi_{c(\lambda)}$ (Equation 4.21) and the photosynthesis action spectrum approximation $\psi_{sy(\lambda)}$ (Equation

4 Estimating Melatonin Suppression and Photosynthesis Activity

4.22) yields the RGB coefficients

$$(r_C, g_C, b_C) = (-0.0346, 0.232, 0.558) \quad \text{and} \quad (4.24)$$

$$(r_{SY}, g_{SY}, b_{SY}) = (0.361, 0.429, 0.600), \quad (4.25)$$

respectively. Finally, the approximations for the circadian action factor a_{cv} and the photosynthesis activity SY are given by

$$a_{cv}(R, G, B) = \frac{C(R, G, B)}{b(R, G, B)} = \frac{-0.0346 \cdot R + 0.232 \cdot G + 0.558 \cdot B}{0.265 \cdot R + 0.670 \cdot G + 0.0648 \cdot B} \quad (4.26)$$

and

$$SY(R, G, B) = 0.361 \cdot R + 0.429 \cdot G + 0.600 \cdot B. \quad (4.27)$$

In Table 4.1 the analytical results for the three light sources in the test scene (D65, LED, monitor light) are presented. The correct values for the circadian action factor a_{cv} and the photosynthesis activity SY are opposed to their RGB approximations. Additionally, the relative errors of the RGB approximations are given. For both indices a_{cv} and SY the RGB approximation performs best for the LED illuminant, followed by the monitor light and lastly the CIE phase of daylight D65. However, even for the LED lamp the relative error for the circadian action index is already greater than 5%.

	D65	LED	TFT
$a_{cv}(\sigma)$	0.941	0.824	0.903
$a_{cv}(R, G, B)$	0.830	0.871	0.834
Δa_{cv}	-11.82%	+5.72%	-7.69%
$SY(\sigma)$	2.198	6.400	0.415
$SY(R, G, B)$	1.581	6.333	0.393
ΔSY	-28.05%	-1.04%	-5.40%

Table 4.1: Analytical results for the three light sources used in the test scene. The correct values of the circadian action factor $a_{cv}(\sigma)$ and the photosynthesis activity $SY(\sigma)$ are opposed to the RGB approximations $a_{cv}(R, G, B)$ and $SY(R, G, B)$, respectively. Additionally, the particular relative error Δ is depicted.

Re-rendering the scene with the standard RGB version of RADIANCE yields an RGB color value for each pixel describing the radiance or irradiance distribution within the test scene. To calculate the approximation for the circadian action factor a_{cv} Equation 4.26 is evaluated for the RGB radiance values of each pixel. The results are presented as falsecolor images in Figure 4.8 for the computer workplace view and in Figure 4.9 for the scene overview as seen from outside, each on the left side. The images on the right side in Figures 4.8 and 4.9 show the relative differences in percent between the correct results for a_{cv} calculated from the spectral renderings (Figures 4.4 and 4.5) and the RGB approximations, i.e.

$$\Delta a_{cv} = 100 \cdot \frac{a_{cv}(R, G, B) - a_{cv}(\sigma)}{a_{cv}(\sigma)}. \quad (4.28)$$

4.3 RGB Approximation

The values for both $a_{cv}(R, G, B)$ and Δa_{cv} for the three light sources D65, LED, and the monitor light comply with the analytical values in Table 4.1.

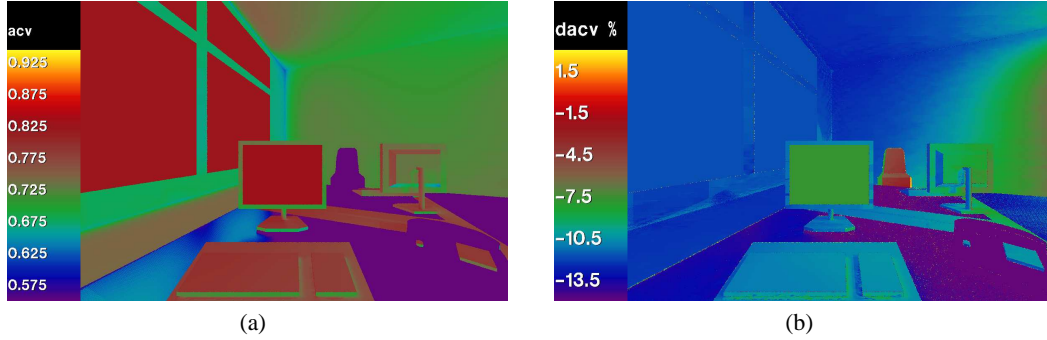


Figure 4.8: (a) Distribution of the approximated circadian action factor $a_{cv}(R, G, B)$ calculated from the RGB rendering using Equation 4.26 in the field of view as perceived by a person working at the front desk and (b) resulting relative differences Δa_{cv} from the values obtained from the spectral rendering.

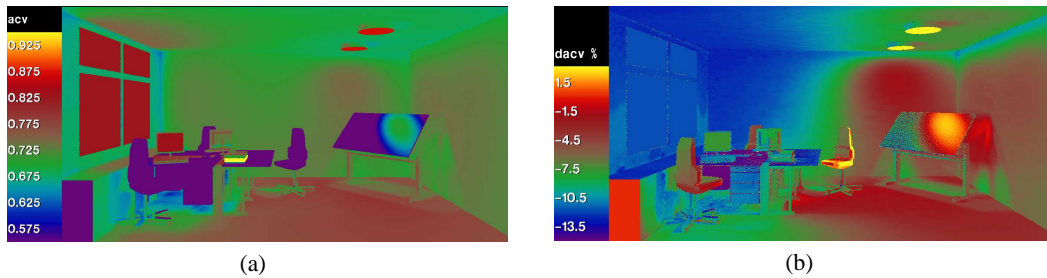


Figure 4.9: (a) Distribution of the approximated circadian action factor $a_{cv}(R, G, B)$ inside the scene calculated from the RGB rendering using Equation 4.26 and (b) resulting relative differences Δa_{cv} from the values obtained from the spectral rendering.

Evaluating Equation 4.27 for the irradiance color values of each pixel obtained from the RGB rendering with the option “-i” yields an approximation for the photosynthesis activity SY at the particular pixel, i.e., the position in the scene. Figure 4.10 shows the RGB approximation for SY (left) opposed to the relative differences in percent between the correct results from the spectral rendering (Figure 4.6) and the RGB approximation, calculated as

$$\Delta SY = 100 \cdot \frac{SY(R, G, B) - SY(\sigma)}{SY(\sigma)}. \quad (4.29)$$

Again, the analytical results for $SY(R, G, B)$ and ΔSY for the three light sources exactly correspond to the values in Table 4.1.

One idea to improve the performance of the approximations is to consider all spectra only on the constrained domain where the action spectra are non-zero. For example the values of the

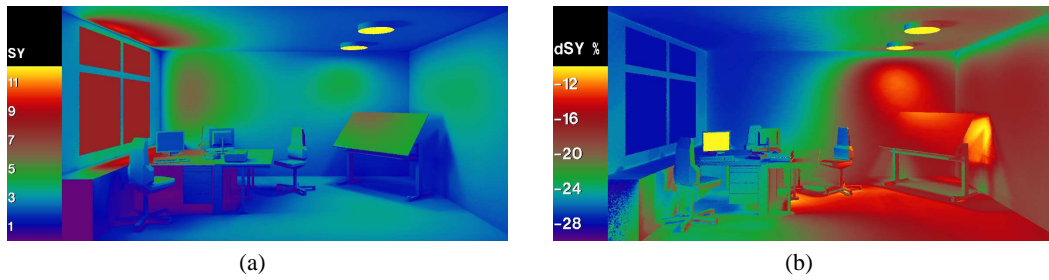


Figure 4.10: (a) Distribution of the approximated photosynthesis activity $SY(R, G, B)$ inside the scene calculated from the RGB rendering using Equation 4.27 and (b) resulting relative differences ΔSY from the values obtained from the spectral rendering.

melatonin suppression function are non-zero in the interval from 380nm to 580nm. From Equations 4.16 to 4.20 an approximation formula for $a_{cv}(\sigma)$ similar to Equations 4.21 and 4.26 can be derived that shows smaller relative errors when compared to the values given in Table 4.1. However, we could not use this approach directly within our RGB renderings as some of the truncated spectra lead to negative RGB input values and the gamut clipping of these RGB triples yields approximations that are worse than those presented in Figures 4.8 and 4.9. For the photosynthesis action spectrum the approach based on the constrained interval from 385nm to 725nm does not improve the approximation because all three color-matching functions \bar{x} , \bar{y} , and \bar{z} are close to zero outside of this domain.

4.4 Conclusion

We have shown how indices derived from various weighting functions such as the circadian action factor or the photosynthesis activity can be calculated within spectrally rendered images. Based on the CIE color-matching functions we presented approximations to calculate the measures a_{cv} and SY from RGB rendered images. However, as these RGB approximations turned out to be rough estimations, we propose to use spectral rendering whenever accurate results are desired. If no spectral rendering engine is available, the methods proposed by Delahunt and Brainard [DB04] and Ruppertsberg and Bloj [RB08] could be used to perform spectral rendering using the standard RGB version of the RADIANCE rendering engine.

Acknowledgments

The authors thank Christian Knoflach and Rico Thetmeyer from our cooperation partner Bartenbach LichtLabor in Aldrans, Austria [Bar], for the office test scene and the associated photometric data. The reviewers' comments that helped to improve this paper are gratefully acknowledged. Parts of this research were supported by the FIT-IT Program of the BMVIT (Bundesministerium für Verkehr, Innovation und Technologie) and the FFG with Grant No. 816009.

A CIE 171:2006 Test Cases 4.1 - 4.6: Results

In the following Tables A.1 to A.6 the results of the point illuminance calculations for the six CIE experimental test cases that were presented in Section 1.1 are opposed to the CIE reference values (Tables A.1 to A.6 in [CIE06]). All given illuminance values were calculated with *rtrace* from version 3.8 of RADIANCE. For the test cases 4.2 and 4.5 (Sections 1.1.2 and 1.1.5), which contain disk luminaires, additional computations were performed using our proposed improved subdivision algorithm for circular light sources (see Section 2.1). These results are listed in the lines entitled “disk sampling”.

The abbreviations for the CIE reference values are as follows:

TE UL is the total error band upper limit,

TE LL is the total error band lower limit,

MB UL is the measurement band upper limit, and

MB LL is the measurement band lower limit.

In the tables, computed values outside the CIE measurement band limits are printed in bold face.

A CIE 171:2006 Test Cases 4.1 - 4.6: Results

Position		Sensor						
		1	2	3	4	5	6	7
	TE UL	91	107	115	118	116	107	93
	MB UL	85	100	108	110	108	100	87
1	RADIANCE	66	77	84	85	83	78	66
	MB LL	65	77	83	85	83	77	67
	TE LL	59	70	75	77	76	70	61
	TE UL	103	124	130	129	129	124	105
	MB UL	96	116	122	120	121	116	98
2	RADIANCE	76	89	95	94	95	88	76
	MB LL	74	89	94	93	93	89	75
	TE LL	67	81	85	84	84	81	68
	TE UL	112	132	141	141	141	131	113
	MB UL	105	123	132	132	132	122	106
3	RADIANCE	83	96	103	105	102	96	84
	MB LL	81	95	101	102	101	94	81
	TE LL	73	86	92	92	92	86	74
	TE UL	115	133	143	146	143	133	116
	MB UL	108	124	133	137	133	124	108
4	RADIANCE	84	97	105	106	104	97	85
	MB LL	83	96	103	105	103	96	83
	TE LL	75	87	93	96	93	87	76
	TE UL	113	132	141	140	141	132	112
	MB UL	105	124	131	131	131	123	105
5	RADIANCE	83	96	102	104	102	95	83
	MB LL	81	95	101	101	101	95	81
	TE LL	74	86	92	92	92	86	73
	TE UL	103	124	130	127	130	123	104
	MB UL	97	116	121	119	121	115	97
6	RADIANCE	77	89	95	95	97	91	76
	MB LL	74	89	93	92	93	89	75
	TE LL	68	81	85	83	85	81	68
	TE UL	92	108	116	117	115	108	92
	MB UL	86	100	108	109	107	100	86
7	RADIANCE	68	78	85	85	84	76	66
	MB LL	66	77	83	84	83	77	66
	TE LL	60	70	76	76	75	70	60

Table A.1: RADIANCE results for the measurement point illuminances of CIE test case 4.1, gray wall - CFL lamp, with upper and lower limits as given by the CIE.

Position	Sensor						
	1	2	3	4	5	6	7
TE UL	50	68	66	60	66	68	51
MB UL	47	63	62	56	61	63	48
1 RADIANCE	35	45	45	42	46	46	35
	disk sampling	36	47	47	44	48	48
MB LL	36	49	48	43	47	49	37
TE LL	33	44	43	39	43	44	33
TE UL	65	93	88	77	87	93	67
MB UL	61	87	83	72	81	87	62
2 RADIANCE	45	61	59	53	60	61	46
	disk sampling	47	64	62	56	63	65
MB LL	47	67	64	55	63	67	48
TE LL	43	61	58	50	57	61	44
TE UL	65	90	87	77	85	90	66
MB UL	61	84	81	72	80	84	62
3 RADIANCE	45	59	59	54	60	61	46
	disk sampling	47	62	62	57	63	64
MB LL	47	65	62	56	61	65	48
TE LL	42	59	57	50	56	59	43
TE UL	61	79	77	72	77	79	61
MB UL	57	74	72	67	72	73	51
4 RADIANCE	42	53	54	53	56	56	44
	disk sampling	44	56	57	56	59	59
MB LL	44	57	55	52	55	56	44
TE LL	40	52	50	47	50	51	40
TE UL	66	89	85	75	83	87	64
MB UL	61	83	79	70	78	82	60
5 RADIANCE	45	59	59	56	63	64	49
	disk sampling	47	62	63	59	66	68
MB LL	47	64	61	54	60	63	46
TE LL	43	58	55	49	54	57	42
TE UL	65	92	85	74	83	89	63
MB UL	61	86	80	69	78	83	59
6 RADIANCE	45	60	60	55	64	67	49
	disk sampling	47	64	63	58	68	70
MB LL	47	66	61	53	60	64	46
TE LL	43	60	56	48	54	58	41
TE UL	50	66	64	57	62	64	48
MB UL	47	62	60	54	58	60	45
7 RADIANCE	35	45	46	44	49	49	38
	disk sampling	36	47	48	46	51	52
MB LL	36	48	46	41	45	46	35
TE LL	33	43	42	38	41	42	31

Table A.2: RADIANCE results for the measurement point illuminances of CIE test case 4.2, gray wall - opal lamp, with upper and lower limits as given by the CIE.

A CIE 171:2006 Test Cases 4.1 - 4.6: Results

Position		Sensor						
		1	2	3	4	5	6	7
	TE UL	178	279	265	222	265	279	180
	MB UL	166	261	248	207	248	261	168
1	RADIANCE	161	241	228	197	233	240	158
	MB LL	128	201	191	159	191	201	130
	TE LL	116	182	173	145	173	182	118
	TE UL	206	312	305	258	308	317	214
	MB UL	192	291	285	241	288	296	200
2	RADIANCE	178	252	245	220	254	255	178
	MB LL	148	224	219	186	222	228	154
	TE LL	135	203	199	169	201	207	140
	TE UL	229	353	337	281	342	358	232
	MB UL	214	330	315	262	319	334	217
3	RADIANCE	196	287	279	245	287	291	198
	MB LL	165	254	242	202	246	257	167
	TE LL	149	230	220	183	223	234	152
	TE UL	209	310	303	265	311	315	207
	MB UL	195	290	283	247	290	294	193
4	RADIANCE	194	282	273	244	282	285	192
	MB LL	150	223	218	191	224	227	149
	TE LL	136	203	198	173	203	206	135
	TE UL	230	358	345	286	344	356	229
	MB UL	215	334	322	267	321	332	214
5	RADIANCE	203	296	285	248	289	289	196
	MB LL	165	257	248	206	247	256	165
	TE LL	150	234	225	187	225	232	150
	TE UL	221	329	317	264	312	317	209
	MB UL	206	308	296	247	291	296	196
6	RADIANCE	184	264	256	225	253	254	178
	MB LL	159	237	228	190	224	228	151
	TE LL	144	215	207	173	204	207	137
	TE UL	188	289	273	229	274	283	180
	MB UL	176	270	255	214	255	264	168
7	RADIANCE	167	249	237	205	240	245	163
	MB LL	135	208	196	165	157	204	129
	TE LL	123	189	178	150	179	185	117

Table A.3: RADIANCE results for the measurement point illuminances of CIE test case 4.3, gray wall - SSR luminaire, with upper and lower limits as given by the CIE.

Position		Sensor						
		1	2	3	4	5	6	7
	TE UL	30	32	39	43	40	33	31
	MB UL	28	29	37	40	38	30	29
1	RADIANCE	26	29	35	37	34	29	26
	MB LL	22	23	28	31	29	23	22
	TE LL	20	21	26	28	26	21	20
	TE UL	31	32	39	42	41	33	31
	MB UL	28	30	37	39	38	31	29
2	RADIANCE	28	29	36	39	36	30	28
	MB LL	22	23	28	30	29	24	23
	TE LL	20	21	26	28	27	21	21
	TE UL	39	41	51	54	51	40	38
	MB UL	36	38	48	51	47	38	35
3	RADIANCE	34	37	45	49	44	37	35
	MB LL	28	29	37	39	37	29	27
	TE LL	25	27	33	36	33	26	25
	TE UL	43	46	57	62	57	46	43
	MB UL	40	43	53	57	53	43	40
4	RADIANCE	37	41	50	52	49	41	37
	MB LL	31	33	41	44	41	33	31
	TE LL	28	30	37	40	37	30	28
	TE UL	38	40	51	54	51	41	38
	MB UL	35	38	48	51	48	38	36
5	RADIANCE	35	37	44	49	44	37	34
	MB LL	27	29	37	39	37	29	28
	TE LL	25	26	33	35	34	27	25
	TE UL	31	33	41	43	40	33	31
	MB UL	29	30	39	40	38	31	29
6	RADIANCE	28	30	37	40	36	30	28
	MB LL	23	23	30	31	29	23	23
	TE LL	20	21	27	28	26	21	20
	TE UL	31	33	42	44	41	33	32
	MB UL	29	31	39	41	38	31	30
7	RADIANCE	27	29	35	38	35	29	27
	MB LL	22	24	30	32	29	24	23
	TE LL	20	21	27	29	26	22	21

Table A.4: RADIANCE results for the measurement point illuminances of CIE test case 4.4, black wall - CFL lamp, with upper and lower limits as given by the CIE.

A CIE 171:2006 Test Cases 4.1 - 4.6: Results

Position	Sensor						
	1	2	3	4	5	6	7
TE UL	32	48	47	42	47	48	33
MB UL	30	44	44	40	44	45	31
1 RADIANCE	23	33	34	31	34	33	24
	disk sampling	24	35	36	33	36	25
MB LL	23	34	34	31	34	35	24
TE LL	21	31	31	28	31	31	22
TE UL	46	73	70	60	69	74	48
MB UL	43	68	66	56	64	69	44
2 RADIANCE	33	50	49	43	50	51	33
	disk sampling	35	53	52	46	53	35
MB LL	33	53	51	43	49	53	34
TE LL	30	48	46	39	45	48	31
TE UL	47	71	70	61	69	72	48
MB UL	44	66	65	57	65	67	45
3 RADIANCE	34	49	49	45	50	50	35
	disk sampling	35	52	53	48	54	37
MB LL	34	51	50	44	50	52	34
TE LL	30	46	45	40	45	47	31
TE UL	43	61	62	56	61	61	43
MB UL	40	57	57	53	57	57	40
4 RADIANCE	31	43	45	44	47	46	33
	disk sampling	33	46	48	46	50	35
MB LL	31	44	44	40	44	44	31
TE LL	28	40	40	37	40	40	28
TE UL	47	71	68	60	68	70	47
MB UL	44	66	64	56	63	65	43
5 RADIANCE	33	49	50	46	53	54	37
	disk sampling	35	52	53	49	57	39
MB LL	34	51	49	43	49	50	33
TE LL	31	46	44	39	44	46	30
TE UL	46	72	68	57	66	71	45
MB UL	43	67	63	54	62	66	42
6 RADIANCE	33	50	49	45	53	55	36
	disk sampling	35	53	53	48	57	39
MB LL	33	52	49	41	47	51	33
TE LL	30	47	44	37	43	46	30
TE UL	32	47	46	40	45	45	31
MB UL	30	44	43	38	42	42	29
7 RADIANCE	23	33	34	33	37	37	26
	disk sampling	24	35	36	35	39	27
MB LL	23	34	33	29	32	33	23
TE LL	21	30	30	26	29	30	20

Table A.5: RADIANCE results for the measurement point illuminances of CIE test case 4.5, black wall - opal lamp, with upper and lower limits as given by the CIE.

Position		Sensor						
		1	2	3	4	5	6	7
	TE UL	146	249	237	197	237	252	149
	MB UL	136	232	221	184	221	235	139
1	RADIANCE	135	216	204	175	210	215	132
	MB LL	105	179	170	142	170	181	107
	TE LL	95	162	155	129	155	164	97
	TE UL	172	288	282	236	284	294	179
	MB UL	161	269	263	221	265	275	168
2	RADIANCE	151	233	227	202	236	235	151
	MB LL	124	207	202	170	204	211	129
	TE LL	113	188	184	154	185	192	117
	TE UL	195	329	313	258	317	335	196
	MB UL	182	307	292	241	296	312	183
3	RADIANCE	170	268	261	228	270	272	172
	MB LL	140	237	225	185	228	241	141
	TE LL	127	215	204	168	207	218	128
	TE UL	178	287	278	242	285	290	176
	MB UL	166	268	259	226	266	271	164
4	RADIANCE	171	264	255	227	265	266	169
	MB LL	128	206	200	174	205	209	126
	TE LL	116	187	181	158	186	190	115
	TE UL	196	334	320	262	319	333	196
	MB UL	183	312	299	244	298	311	183
5	RADIANCE	178	277	267	231	272	271	170
	MB LL	141	240	230	188	230	239	141
	TE LL	128	218	209	171	208	217	128
	TE UL	186	306	292	242	287	292	175
	MB UL	174	286	273	226	268	273	163
6	RADIANCE	157	243	237	207	235	233	151
	MB LL	134	220	210	174	206	210	126
	TE LL	122	200	191	158	187	191	114
	TE UL	155	258	241	202	242	251	146
	MB UL	145	241	225	189	226	234	136
7	RADIANCE	139	222	212	182	215	218	135
	MB LL	111	186	173	145	174	180	105
	TE LL	101	169	157	132	158	164	95

Table A.6: RADIANCE results for the measurement point illuminances of CIE test case 4.6, black wall - SSR luminaire, with upper and lower limits as given by the CIE.

A CIE 171:2006 Test Cases 4.1 - 4.6: Results

B Supplementary Material for the New BRDF Model

In Section 2.2.2 on page 35 we state that, in the plane of incidence, the maximum of our new BRDF $f_{new}(\theta_l, \phi_l; \theta_v, \phi_v)$ occurs below the mirror direction, whereas the peak of the new BRDF times the cosine of the polar angle of the reflected direction $f_{new}(\theta_l, \phi_l; \theta_v, \phi_v) \cdot \cos \theta_v$ is found in the mirror direction.

Let $\rho_s = 1$ and $\theta_l > 0$. In the plane of incidence $\phi_v = \phi_l + \pi$ and hence

$$f_{new}(\theta_l, \phi_l; \theta_v, \phi_l + \pi) = \frac{1}{\pi\alpha\beta} \cdot \exp\left(-\left(\frac{\cos^2 \phi_l}{\alpha^2} + \frac{\sin^2 \phi_l}{\beta^2}\right) \left(\frac{\sin \theta_v - \sin \theta_l}{\cos \theta_l + \cos \theta_v}\right)^2\right) \cdot \frac{2(1 + \cos(\theta_l + \theta_v))}{(\cos \theta_l + \cos \theta_v)^4}. \quad (\text{B.1})$$

Partial differentiation with respect to θ_v yields

$$\left. \frac{\partial f_{new}(\theta_l, \phi_l; \theta_v, \phi_l + \pi)}{\partial \theta_v} \right|_{\theta_v = \theta_l} = \frac{1}{4\pi\alpha\beta} \cdot \frac{\sin \theta_l}{\cos^3 \theta_l} > 0. \quad (\text{B.2})$$

Thus $f_{new}(\theta_l, \phi_l; \theta_v, \phi_l + \pi)$ is still increasing in the mirror direction $\theta_v = \theta_l$ and must have its maximum below. Using the product rule and applying Equation (2.27) we find that

$$\left. \frac{\partial (f_{new}(\theta_l, \phi_l; \theta_v, \phi_l + \pi) \cdot \cos \theta_v)}{\partial \theta_v} \right|_{\theta_v = \theta_l} = \frac{1}{4\pi\alpha\beta} \cdot \frac{\sin \theta_l}{\cos^2 \theta_l} - f_{new}(\theta_l, \phi_l; \theta_l, \phi_l + \pi) \cdot \sin \theta_l = 0. \quad (\text{B.3})$$

Thus $f_{new}(\theta_l, \phi_l; \theta_v, \phi_v + \pi) \cdot \cos \theta_v$ has its maximum in the mirror direction $\theta_v = \theta_l$. □

In Equation 2.30 we state that the albedo of our new BRDF meets energy balance, i.e. its albedo is bounded by 1. Rewriting Equation (2.30) with respect to the sampling PDF $d_{\alpha,\beta}$ (see Equations (2.31) and (2.32)) yields

$$a(\vec{v}) = \int_0^{2\pi} \int_0^{\pi/2} \frac{2}{1 + \cos \theta_v / \cos \theta_l} \cdot d_{\alpha,\beta}(\theta_l, \phi_l; \theta_v, \phi_v) \cos \theta_l \sin \theta_l d\theta_l d\phi_l. \quad (\text{B.4})$$

Let $\epsilon = \tan \delta$ and ϕ, δ as given by Ward's sampling method (see Equation (2.21)). From the

B Supplementary Material for the New BRDF Model

spherical coordinates

$$\vec{v} = (\sin \theta_v \cos \phi_v, \sin \theta_v \sin \phi_v, \cos \theta_v), \quad (\text{B.5})$$

$$\vec{h} = (\epsilon \cos \phi, \epsilon \sin \phi, 1)/\sqrt{1 + \epsilon^2}, \quad (\text{B.6})$$

$$\text{and } \vec{l} = (\sin \theta_l \cos \phi_l, \sin \theta_l \sin \phi_l, \cos \theta_l) = -\vec{v} + 2\langle \vec{h}, \vec{v} \rangle \vec{h} \quad (\text{B.7})$$

we compute

$$\cos \theta_l = -\cos \theta_v + 2\frac{\epsilon \sin \theta_v \cos(\phi - \phi_v) + \cos \theta_v}{1 + \epsilon^2} \quad (\text{B.8})$$

and thus

$$\frac{\cos \theta_l}{\cos \theta_v} = \frac{1 - \epsilon^2 + 2\epsilon \tan \theta_v \cos(\phi - \phi_v)}{1 + \epsilon^2}. \quad (\text{B.9})$$

By the transformation law for densities and by substituting Equation (B.9) into Equation (B.4) we obtain

$$a(\vec{v}) = \iint_D \frac{2}{1 + (1 + \epsilon^2)/(1 - \epsilon^2 + 2\epsilon \tan \theta_v \cos(\phi - \phi_v))} dsdt, \quad (\text{B.10})$$

where D denotes the valid domain where $\theta_l < \pi/2$ and thus a sample ray is not rejected:

$$D = \{(s, t) \in [0, 1]^2 | 1 - \epsilon^2 + 2\epsilon \tan \theta_v \cos(\phi - \phi_v) > 0\}. \quad (\text{B.11})$$

In the general case, i.e. where ϵ is small and at non-grazing angles where $\tan \theta_v$ is not too large, the albedo approximates 1:

$$a(\vec{v}) \approx \iint_{[0,1]^2} \frac{2}{1 + 1} dsdt = 1. \quad (\text{B.12})$$

For grazing angles, let $\epsilon \neq 0$ and $\theta_v \rightarrow \pi/2$. Then

$$\frac{2}{1 + (1 + \epsilon^2)/(1 - \epsilon^2 + 2\epsilon \tan \theta_v \cos(\phi - \phi_v))} \rightarrow 2 \quad (\text{B.13})$$

and

$$D \rightarrow \{(s, t) \in [0, 1]^2 | \cos(\phi - \phi_v) > 0\}. \quad (\text{B.14})$$

Although in general ϕ is not uniformly distributed in $(-\pi, \pi]$, the probability that a sample ray is not rejected

$$\text{P}\{\cos(\phi - \phi_v) > 0\} = 1/2 \quad (\text{B.15})$$

because the distribution of ϕ is point symmetric about the origin. Combining Equation (B.10) with Equations (B.13) to (B.15) yields that $a(\vec{v}) \rightarrow 1$ if $\theta_v \rightarrow \pi/2$.

□

$\theta_v \backslash \theta_l$	25°	35°	45°	55°	65°	75°
0.0°	0.001348	0.001348	0.001348	0.001348	0.001348	0.001348
2.5°	0.001348	0.001348	0.001348	0.001348	0.001348	0.001348
5.0°	0.001348	0.001348	0.001348	0.001348	0.001348	0.001348
7.5°	0.001348	0.001348	0.001348	0.001348	0.001348	0.001348
10.0°	0.001348	0.001348	0.001348	0.001348	0.001348	0.001348
12.5°	0.001348	0.001348	0.001348	0.001348	0.001348	0.001348
15.0°	0.013480	0.001348	0.001348	0.001348	0.001348	0.001348
17.5°	0.107840	0.001348	0.001348	0.001348	0.001348	0.001348
20.0°	0.202200	0.001348	0.001348	0.001348	0.001348	0.001348
22.5°	0.505500	0.014154	0.001348	0.001348	0.001348	0.001348
25.0°	0.808800	0.026960	0.001348	0.001348	0.001348	0.001348
27.5°	0.505500	0.114580	0.007414	0.001348	0.001348	0.001348
30.0°	0.202200	0.202200	0.013480	0.001348	0.001348	0.001348
32.5°	0.134800	0.572900	0.040440	0.001348	0.001348	0.001348
35.0°	0.067400	0.943600	0.067400	0.001348	0.001348	0.001348
37.5°	0.040440	0.606600	0.148280	0.007414	0.001348	0.001348
40.0°	0.013480	0.269600	0.229160	0.013480	0.001348	0.001348
42.5°	0.007414	0.148280	0.721180	0.040440	0.001348	0.001348
45.0°	0.001348	0.026960	1.213200	0.067400	0.001348	0.001348
47.5°	0.001348	0.014154	0.808800	0.202200	0.007414	0.001348
50.0°	0.001348	0.001348	0.404400	0.337000	0.013480	0.001348
52.5°	0.001348	0.001348	0.235900	1.179500	0.040440	0.001348
55.0°	0.001348	0.001348	0.067400	2.022000	0.067400	0.001348
57.5°	0.001348	0.001348	0.040440	1.348000	0.370700	0.007414
60.0°	0.001348	0.001348	0.013480	0.674000	0.674000	0.013480
62.5°	0.001348	0.001348	0.007414	0.370700	2.493800	0.074140
65.0°	0.001348	0.001348	0.001348	0.067400	4.313600	0.134800
67.5°	0.001348	0.001348	0.001348	0.040440	2.898200	0.808800
70.0°	0.001348	0.001348	0.001348	0.013480	1.482800	1.482800
72.5°	0.001348	0.001348	0.001348	0.007414	0.842500	6.335600
75.0°	0.001348	0.001348	0.001348	0.001348	0.202200	11.18840
77.5°	0.001348	0.001348	0.001348	0.001348	0.134800	6.335600
80.0°	0.001348	0.001348	0.001348	0.001348	0.067400	1.482800
82.5°	0.001348	0.001348	0.001348	0.001348	0.001348	0.808800
85.0°	0.001348	0.001348	0.001348	0.001348	0.001348	0.134800
87.5°	0.001348	0.001348	0.001348	0.001348	0.001348	0.074140
90.0°	0.001348	0.001348	0.001348	0.001348	0.001348	0.013480

Table B.1: Reflection data for an isotropic red linoleum floor measured by Bartenbach LichtLabor; total reflection ρ under CIE standard illuminant A: 17.5%.

B Supplementary Material for the New BRDF Model

Bibliography

- [AS00] ASHIKHMIN M., SHIRLEY P.: An anisotropic phong brdf model. *Journal of Graphics Tools* 5 (2000), 25–32.
- [Bab09] BABELCOLOR: ColorChecker data.
www.babelcolor.com/download/ColorChecker_RGB_and_spectra.xls, Nov. 7, 2009.
- [Bar] BARTENBACH LICHTLABOR: Homepage. www.bartenbach.com.
- [BCSS04] BODROGI P., CSUTI P., SZABO F., SCHANDA J.: Why Does the CIE Colour Rendering Index Fail for White RGB LED Light Sources? In *Proc. of CIE Expert Symposium on LED Light Sources* (Tokyo, 2004), Vienna, CIE.
- [BHG*01] BRAINARD G. C., HANIFIN J. P., GREESON J. M., BYRNE B., GLICKMAN G., GERNER E., ROLLAG M. D.: Action spectrum for melatonin regulation in humans: Evidence for a novel circadian photoreceptor. *The Journal of Neuroscience* 21, 16 (2001), 6405–6412.
- [Bli77] BLINN J. F.: Models of light reflection for computer synthesized pictures. *SIG-GRAPH Comput. Graph.* 11, 2 (1977), 192–198.
- [BMD04] BERGNER S., MÖLLER T., DREW M. S.: A Spectral Engine for Visualization. Technical Report SFU-CMPT-TR2004-06, 2004.
- [Bod04] BODROGI P.: Colour rendering: past, present (2004), and future. In *Proc. of CIE Expert Symposium on LED Light Sources* (Tokyo, 2004), Vienna, CIE, pp. 10–12.
- [BS63] BECKMANN P., SPIZZICHINO A. (Eds.): *The Scattering of Electromagnetic Waves from Rough Surfaces*. Pergamon Press, NY, 1963.
- [BS06] BAEHR H. D., STEPHAN K.: *Wärme- und Stoffübertragung*. Springer-Verlag Berlin Heidelberg, 2006.
- [CIE94] CIE: *A Method of Predicting Corresponding Colours under Different Chromatic and Illuminance Adaptations*. CIE Publication 109-1994, 1994.
- [CIE95] CIE: *Method of Measuring and Specifying Colour Rendering Properties of Light Sources*. CIE Publication CIE 13.3-1995, 1995.
- [CIE99] CIE: *Colour rendering*. TC 1-33 closing remarks, CIE Publication 135/2, 1999.
- [CIE04] CIE: *Colorimetry*. 3rd ed., CIE Publication 15:2004, 2004.

Bibliography

- [CIE06] CIE: *Test Cases to Assess the Accuracy of Lighting Computer Programs*. CIE Publication 171:2006, 2006.
- [CIE07] CIE: *Colour Rendering of White LED Light Sources*. CIE Publication 177:2007, 2007.
- [Cor09] CORNELL UNIVERSITY PROGRAM OF COMPUTER GRAPHICS: The Cornell Box. Project web page, www.graphics.cornell.edu/online/box, Sept. 3, 2009.
- [CT81] COOK R. L., TORRANCE K. E.: A reflectance model for computer graphics. In *SIGGRAPH '81: Proceedings of the 8th annual conference on Computer graphics and interactive techniques* (New York, NY, USA, 1981), ACM, pp. 307–316.
- [Dau07] DAU DESIGN AND CONSULTING INC.: Validation of AGi32 against CIE 171:2006. available online: www.agi32.com (April 2, 2008), June 2007.
- [DB04] DELAHUNT P. B., BRAINARD D. H.: Does human color constancy incorporate the statistical regularity of natural daylight? *J. Vision* 4, 2 (2004), 57–81.
- [DBB03] DUTRÉ P., BALA K., BEKAERT P.: *Advanced Global Illumination*. A. K. Peters, Ltd., Natick, MA, USA, 2003.
- [DCWP02] DEVLIN K., CHALMERS A., WILKIE A., PURGATHOFER W.: Star report on tone reproduction and physically based spectral rendering. In *Eurographics 2002* (2002), Eurographics Association.
- [DIN00] DIN: *Optical radiation physics and illuminating engineering - Part 10: Photobiologically effective radiation, quantities, symbols and actions*. DIN 5031-10, 2000.
- [DO05] DAVIS W., OHNO Y.: Toward an improved color rendering metric. In *Fifth International Conference on Solid State Lighting* (2005), vol. 5941, SPIE, pp. 59411G–1 – 59411G–8.
- [Dür06] DÜR A.: An Improved Normalization for the Ward Reflectance Model. *Journal of Graphics Tools* 11, 1 (2006), 51–59.
- [Fot97] FOTIOS S. A.: *The perception of light sources of different colour properties*. PhD thesis, UMIST, Manchester, 1997.
- [FS00] FINLAYSON G., SÜSSTRUNK S.: Spectral Sharpening and the Bradford Transform. In *Proc. CIS2000* (Derby, UK, 2000).
- [Gal09] GALL D.: Die Messung circadianer Strahlungsgrößen. available online: www.tu-ilmenau.de/fakmb/fileadmin/template/fglt/publikationen/2004/Vortrag_Gall2004.pdf, Nov. 7, 2009.
- [GB04] GALL D., BIESKE K.: Definition and Measurement of Circadian Radiometric Quantities. In *Proc. of CIE Symposium '04* (2004).

- [GH04] GUO X., HOUSER K. W.: A review of colour rendering indices and their application to commercial light sources. *Lighting Res. and Technol.* 36, 3 (2004), 183–199.
- [Gla89] GLASSNER A. S. (Ed.): *An introduction to ray tracing*. Academic Press Ltd., London, UK, 1989.
- [GM] GEISLER-MORODER D.: Personal Homepage.
www.uibk.ac.at/mathematik/personal/geisler-moroder.
- [GM06] GEISLER-MORODER D.: *Farbwiedergabe und Farbdifferenzen*. Master's thesis, University of Innsbruck in collaboration with Bartenbach LichtLabor, 2006.
- [GMD08] GEISLER-MORODER D., DÜR A.: Validation of Radiance against CIE171:2006 and Improved Adaptive Subdivision of Circular Light Sources. In *7th International RADIANCE Workshop* (Fribourg, Switzerland, 2008).
- [GMD09a] GEISLER-MORODER D., DÜR A.: Color Rendering Indices in Global Illumination Methods. In *Human Vision and Electronic Imaging XIV* (San Jose, CA, 2009), vol. 7240, SPIE, pp. 72401F–1 – 72401F–9.
- [GMD09b] GEISLER-MORODER D., DÜR A.: Color-rendering indices in global illumination methods. *Journal of Electronic Imaging* 18, 4 (2009), 043015–1–043015–12.
- [GMD10] GEISLER-MORODER D., DÜR A.: Estimating Melatonin Suppression and Photosynthesis Activity in Real-World Scenes from Computer Generated Images. In *Proc. 5th European Conference on Colour in Graphics, Imaging, and Vision (CGIV 2010)* (Joensuu, Finland, 2010), IS&T. (To appear).
- [Gry89] GRYNBERG A.: Validation of Radiance. Technical Report LBID 1575, Lawrence Berkely Laboratory, 1989.
- [Heu92] HEUSER H.: *Funktionalanalysis*. B. G. Teubner Stuttgart, 1992.
- [HTSG91] HE X. D., TORRANCE K. E., SILLION F. X., GREENBERG D. P.: A comprehensive physical model for light reflection. *SIGGRAPH Comput. Graph.* 25, 4 (1991), 175–186.
- [Hun95] HUNT R. W. G.: *Measuring Colour, 2nd. Ed.* Ellis Horwood, Hertfordshire, UK, 1995.
- [JF99] JOHNSON G. M., FAIRCHILD M. D.: Full-Spectral Color Calculations in Realistic Image Synthesis. *IEEE Comput. Graph. Appl.* 19, 4 (1999), 47–53.
- [Jud62] JUDD D. B.: A flattery index for artificial illuminants. *Illum. Eng. (N.Y.)* 62 (1962), 593–598.
- [Kaj86] KAJIYA J. T.: The rendering equation. *SIGGRAPH Comput. Graph.* 20, 4 (1986), 143–150.

Bibliography

- [Kno06] KNOFLACH C.: Private Communication. Bartenbach LichtLabor, Aldrans, Austria, 2006.
- [KSKK10] KURT M., SZIRMAY-KALOS L., KŘIVÁNEK J.: An anisotropic brdf model for fitting and monte carlo rendering. *SIGGRAPH Comput. Graph.* 44, 1 (2010), 1–15.
- [Lew94] LEWIS R. R.: Making shaders more physically plausible. *Computer Graphics Forum (Eurographics '94 Conference Issue)* 13, 3 (1994), 1–13.
- [LFTG97] LAFORTUNE E. P. F., FOO S.-C., TORRANCE K. E., GREENBERG D. P.: Non-linear approximation of reflectance functions. In *SIGGRAPH '97: Proceedings of the 24th annual conference on Computer graphics and interactive techniques* (1997), pp. 117–126.
- [LH54] LAWSON D. I., HIRD D.: A photometric method of determining configuration factors. *British Journal of Applied Physics* 5, 2 (1954), 72–74.
- [Lin09] LINDBLOOM B. J.: Personal homepage. <http://brucelindbloom.com>, Sept. 3, 2009.
- [LJJ09] LABAYRADE R., JENSEN H. W., JENSEN C.: Validation of Velux Daylight Visualizer 2 Against CIE 171:2006 Test Cases. In *Eleventh International IBPSA Conference* (Glasgow, Scotland, 2009), pp. 1506–1513.
- [LLC03] LI C., LUO M. R., CUI G.: Colour-Difference Evaluation Using Colour Appearance Models. In *Eleventh Color Imaging Conference* (2003), pp. 127–131.
- [LS98] LEE M., SAMET H.: Traversing the Triangle Elements of an Icosahedral Spherical Representation in Constant-Time. In *Proc. 8th Intl. Symp. on Spatial Data Handling* (Vancouver, Canada, 1998), pp. 22–33.
- [Mar99] MARDALJEVIC J.: *Daylight Simulation: Validation, Sky Models and Daylight Coefficients*. PhD thesis, De Montfort University, Institute of Energy and Sustainable Development, Leicester, 1999.
- [Mar09] MARIA M.: Little cms. Project web page, www.littlecms.com, Sept. 3, 2009.
- [Mey88] MEYER G.: Wavelength Selection for Synthetic Image Generation. *Computer Vision, Graphics, and Image Processing* 41, 1 (1988), 57–79.
- [MMD76] MCCAMY C. S., MARCUS H., DAVIDSON J. G.: A Color-Rendition Chart. *Journal of Applied Photographic Engineering* 20, 3 (1976), 95–99.
- [NDM05] NGAN A., DURAND F., MATUSIK W.: Experimental Analysis of BRDF Models. In *Proc. of Eurographics Symposium on Rendering EGSR'05* (2005), pp. 117–126.
- [NNSK99] NEUMANN L., NEUMANN A., SZIRMAY-KALOS L.: Compact metallic reflectance models. *Computer Graphics Forum* 18 (1999), 161–172.

- [NRH*77] NICODEMUS F. E., RICHMOND J. C., HSIA J. J., GINSBER I. W., LIMPERIS T.: *Geometrical Considerations and Nomenclature for Reflectance*. NBS Monograph 160, U. S. Dept. of Commerce, 1977.
- [NS06] NEUMANN L., SCHANDA J.: Effect of Interreflections in a Room on the Colour Rendering of Light Source. In *Proc. 3rd European Conf. on Color in Graphics, Imaging, and Vision (CGIV06)*, Leeds, UK (2006), IS&T, pp. 283–286.
- [Pee93] PEERCY M. S.: Linear Color Representations for Full Spectral Rendering. In *SIGGRAPH '93 Proceedings* (1993), pp. 191–198.
- [Pho75] PHONG B. T.: Illumination for computer generated pictures. *Commun. ACM* 18, 6 (1975), 311–317.
- [Poi86] POINTER M. R.: Measuring colour rendering – a new approach. *Lighting Res. and Technol.* 18, 4 (1986), 175–184.
- [Rad10] RADIANCE KNOWLEDGE DATABASE: Project web page. www.radiance-online.org, Jan. 22, 2010.
- [RB06] RUPPERTSBERG A. I., BLOJ M.: Rendering complex scenes for psychophysics using radiance: How accurate can you get? *J. Opt. Soc. Am. A* 23, 4 (2006), 759–768.
- [RB08] RUPPERTSBERG A. I., BLOJ M.: Creating physically accurate visual stimuli for free: Spectral rendering with RADIANCE. *Behavior Research Methods* 40, 1 (2008), 304–308.
- [SBS09] SZABO F., BODROGI P., SCHANDA J.: A colour harmony rendering index based on predictions of colour harmony impression. *Lighting Res. and Technol.* 41, 2 (2009), 165–182.
- [Sch94] SCHLICK C.: An Inexpensive BRDF Model for Physically-Based Rendering. *Computer Graphics Forum* 13, 3 (1994), 233–246.
- [Sch97] SCHANDA J.: Colour rendering in the light of the new CIE recommendation. In *ELIS'97 Symp.* (Bucuresti, 1997), available online: www.knt.vein.hu/staff/schandaj/SJCV-Publ-2005/381.doc, (Dec. 9, 2009).
- [Sch02] SCHANDA J.: The concept of colour rendering revisited. In *First European Conference on Color in Graphics, Imaging, and Vision (CGIV '2002)* (Poitiers, France, 2002), IS&T.
- [Sch07] SCHANDA J. (Ed.): *Colorimetry: Understanding the CIE System*. John Wiley & Sons, Inc., Hoboken, NJ, 2007.
- [Sei85] SEIM T.: In search of an improved method for assessing the colour rendering properties of light sources. *Lighting Res. and Technol.* 17, 1 (1985), 12–22.

Bibliography

- [SG02] SLATER A., GRAVES H.: *Benchmarking Lighting Design Software*. TM 28/00, 33. CIBSE, London, 2002.
- [Smi99] SMITS B.: An RGB-to-Spectrum Conversion for Reflectances. *Journal of Graphics Tools* 4, 4 (1999), 11–22.
- [SP94] SILLION F. X., PUECH C.: *Radiosity and Global Illumination*. Morgan Kaufmann Publishers Inc., San Francisco, CA, USA, 1994.
- [SS03] SCHANDA J., SÁNDOR N.: Colour Rendering, Past – Present – Future. In *International Lighting and Colour Conf., Cape Town* (Nov. 2003).
- [SS06] SÁNDOR N., SCHANDA J.: Visual colour rendering based on colour difference evaluations. *Lighting Res. and Technol.* 38, 3 (2006), 225–239.
- [SV86] SEIM T., VALBERG A.: Towards a uniform color space: A better formula to describe the munsell and OSA color scales. *Color Res. & Appl.* 11, 1 (1986), 11–24.
- [SWD05] SHARMA G., WU W., DALAL E. N.: The CIEDE2000 Color-Difference Formula: Implementation Notes, Supplementary Test Data, and Mathematical Observations. *Color Res. & Appl.* 30, 1 (2005), 21–30.
- [SWZ96] SHIRLEY P., WANG C., ZIMMERMAN K.: Monte carlo techniques for direct lighting calculations. *ACM Trans. Graph.* 15, 1 (1996), 1–36.
- [SZBS07] SZABO F., ZILIZI I., BODROGI P., SCHANDA J.: Visual experiments on colour harmony: a formula and a rendering index. CIE 26th Session, CIE 178:2007 D1-2 – D1-5, 2007.
- [TAS01] THAPAN K., ARENDT J., SKENE D. J.: An action spectrum for melatonin suppression: evidence for a novel non-rod, non-cone photoreceptor system in humans. *Journal of Physiology* 535, 1 (2001), 261–267.
- [Taz99a] TAZAWA S.: Effects of Various Radiant Sources on Plant Growth (Part 1). *Japan Agricultural Research Quarterly* 33, 3 (1999), 163–176.
- [Taz99b] TAZAWA S.: Effects of Various Radiant Sources on Plant Growth (Part 2). *Japan Agricultural Research Quarterly* 33, 3 (1999), 177–183.
- [Tho72] THORNTON W. A.: Color-discrimination index. *J. Opt. Soc. Am.* 62 (1972), 191–194.
- [Tho74] THORNTON W. A.: A validation of the color-preference index. *J. Illum. Eng. Soc.* 4 (1974), 48–52.
- [TS67] TORRANCE K. E., SPARROW E. M.: Theory for off-specular reflection from roughened surfaces. *J. Opt. Soc. Am.* 57, 9 (1967), 1105–1112.

- [UWP05] ULBRICHT C., WILKIE A., PURGATHOFER W.: Verification of Physically Based Rendering Algorithms. In *State of the Art Reports, Eurographics 05* (Dublin, Ireland, 2005), Eurographics Association, pp. 95–112.
- [VEBM07] VIENOT F., EZRATI J. J., BOUST C., MAHLER E.: Grading LED illumination: from colour rendering indices to specific light quality indices. CIE 26th Session, CIE 178:2007 D1-22 – D1-25, 2007.
- [VK05] VON KRIES J.: Positive und negative Nachbilder. Lokale und Farbenumstimmungen des Sehorgans. In *Handbuch der Physiologie des Menschen, 3. Band*, Nagel W., (Ed.). F. Vieweg u. Sohn, Braunschweig, Germany, 1905, pp. 205–220.
- [Wal05] WALTER B.: Notes on the Ward BRDF. Technical Report PCG-05-06, Cornell Program of Computer Graphics, available on: www.graphics.cornell.edu/~bjw/wardnotes.pdf, 2005.
- [War92] WARD G. J.: Measuring and Modeling Anisotropic Reflection. *Computer Graphics* 26, 2 (1992), 265–272.
- [War94] WARD G. J.: The RADIANCE lighting simulation and rendering system. In *SIGGRAPH '94 Proceedings* (New York, NY, USA, 1994), ACM, pp. 459–472.
- [War08] WARD G.: Private Communication, December, 2008.
- [War09] WARD G.: Personal Homepage. www.anywhere.com/gward/papers/egwr02, Sept. 3, 2009.
- [Wer95] WERNER D.: *Funktionalanalysis*. Springer-Verlag Berlin Heidelberg, 1995.
- [Wes00] WESTLUND H. B.: *Appearance Based Rendering*. Master's thesis, Graduate School of the University of Oregon, 2000.
- [WEV02] WARD G., EYDELBERG-VILESHIN E.: Picture Perfect RGB Rendering Using Spectral Prefiltering and Sharp Color Primaries. In *13th Eurographics Workshop on Rendering (EGWR02)* (Pisa, Italy, 2002), Eurographics Association, pp. 117–124.
- [WGGM*] WITTKOPF S., GROBE L. O., GEISLER-MORODER D., COMPAGNON R., KÄMPF J., LINHART F., SCARTEZZINI J.-L.: Photometric quantities of anidolic daylight collectors. Submitted to *Solar Energy*.
- [Whi80] WHITTED T.: An improved illumination model for shaded display. *Commun. ACM* 23, 6 (1980), 343–349.
- [WMW99] WESTLUND H. B., MEYER G. W., WALKER P. A.: iBRDF - Version 1.0 documentation. Department of Computer & Information Science, University of Oregon, Eugene, Oregon 97403, 1999.

Bibliography

- [WS98] WARD G., SHAKESPEARE R.: *Rendering with Radiance*. Morgan Kaufmann Publishers, 1998.
- [Xu93] XU H.: Colour rendering capacity and luminous efficiency of a spectrum. *Lighting Res. and Technol.* 25, 3 (1993), 131–132.
- [Xu95] XU H.: Sample-independent color rendering index. *Color Res. & Appl.* 20, 4 (1995), 251–254.

Curriculum Vitae

Personal Data

Name: David Geisler-Moroder
Date of Birth: September 3, 1983
Place of Birth: Rum in Tirol, Austria
Nationality: Austria

Education

Since 10/2006 Doctoral programme in Engineering Sciences, University of Innsbruck
Area of dissertation: Technical Mathematics
Ph.D. Thesis: *Accuracy Improvements for Computational Methods and Color Rendering Index Calculations in Global Illumination Models*

06/2006 Diploma exam with honours (Dipl.-Ing.)

2001 – 2006 Diploma programme in Technical Mathematics, University of Innsbruck
Diploma thesis: *Farbwiedergabe und Farbdifferenzen*

06/2001 School leaving exam with honours

1993 – 2001 Bundesrealgymnasium Adolf-Pichler-Platz, Innsbruck

1989 – 1993 Elementary school Allerheiligen, Innsbruck

Career History

Since 07/2009 Project collaborator in the FFG dissertation fellowship project *CRIGIM* at the Department of Mathematics, University of Innsbruck

03/2009 – 06/2009 Visiting Scholar at SERIS – Solar Energy Research Institute of Singapore under Prof. Stephen Wittkopf

03/2008 – 02/2009 Project collaborator in the FFG dissertation fellowship project *CRIGIM* at the Department of Mathematics, University of Innsbruck

02/2007 – 03/2007 Scientific assistant of Prof. Arne Dür at the Department of Mathematics, University of Innsbruck

Curriculum Vitae

Awards

- 03/2008 – 06/2010 FFG dissertation fellowship, program line FIT-IT, Visual Computing
- 06/2008 “Förderungsstipendium”, University of Innsbruck
- 05/2007 – 04/2008 “Doktoratsstipendium”, University of Innsbruck
- 11/2006 Scientific prize of The Austrian Federal Economic Chamber for the Diploma thesis *Farbwiedergabe und Farbdifferenzen*

Publications

[GM06], [GMD08], [GMD09b], [GMD09a], [GMD10], [WGGM*].